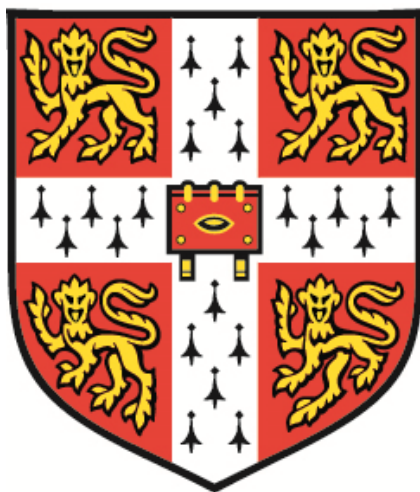


The Study of Organic Crystals by Atomic Force Microscopy



University of Cambridge
Wolfson College

A thesis submitted for the degree of

Doctor of Philosophy

June 2014

Author:

Ernest Ho Hin Chow

Supervisor:

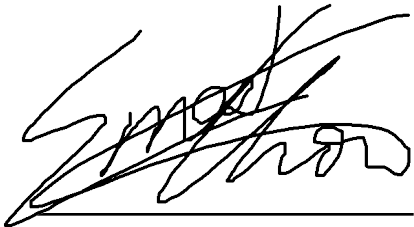
Prof. William Jones

Declaration

The work described in this report was carried out at the Department of Chemistry, University of Cambridge, under the supervision of Prof. W. Jones. The report is the result of my own work except where specific reference is made.

This report is not the same as any that I have submitted for a degree, diploma, or other qualifications at any other university. No part of this thesis has been, or is concurrently being submitted for any such degree, diploma, or other qualification.

As specified by the Degree Committee of Physics and Chemistry, this thesis lies within the 60,000 word limit.

A handwritten signature in black ink, appearing to read 'Ernest Chow', written over a horizontal line.

Ernest Chow

June 2014

Acknowledgements

I would like to thank my academic supervisor, Prof. William Jones, and my industrial supervisor, Dr. John Murphy. I truly appreciate their guidance and training, and also their friendly support throughout my PhD, allowing these few years of research experience to be a fruitful and enjoyable one.

I am grateful to all the members of the Materials Chemistry Group. It has been a pleasure working with the group, and group meetings as well as lunchtime discussions have often been insightful and entertaining. I'd like to thank Mark in particular, who first trained me to use the atomic force microscope, and Dinesh, whom we have frequently worked together and has assisted me in performing some calculations for part of a chapter in this report. I would also like to thank Hugh for proofreading this thesis. Kreso, Bhavnita, Hugh, Mihails, Sam and all other members have also been really helpful in many ways. Ex-members Catherine and Andrew are acknowledged for useful email discussions.

Sven Schroeder and Lauren Newton from University of Manchester are acknowledged for conducting the XPS experiments for the studies on aspirin surfaces.

I also need to thank my parents, my brother, and Wilma. They have always been supportive to me in every way, and I would not have gotten this far if it weren't for their endless encouragement and love towards me.

Last but not least, I would like to thank the Pfizer Institute of Pharmaceutical Materials Science for providing the funding for this PhD.

Abstract

Organic crystals are found in everyday goods such as foods, drugs, dyes, and agricultural products. To better understand the solid-state behaviour of organic crystals, the study of their surfaces is crucial, as several reactions occur at the interface between the crystal surface and its immediate environment. While atomic force microscopy (AFM) is a useful tool for studying surfaces, it is not a common technique for studying organic crystals. The first part of this report aims to address problems of imaging organic crystals by AFM which arise from the nature of the imaging technique and the material property of organic crystals. Methods of detecting and predicting the likelihood of the problems encountered in imaging organic crystals are suggested in order for a more accurate interpretation of the information obtained by this technique.

The effect of humidity on aspirin crystal surfaces is then investigated by AFM. The growth of new features on the surface is believed to be a result of the hydrolysis of aspirin molecules. Mechanisms are suggested based on the observed surface response of aspirin, where surface defects and the mobility of surface molecules are believed to be important factors affecting reactivity.

The last section investigates the solid-state photochemical reaction of anthracene, which is a reaction that should not occur according to the topochemical postulate. The surface response of anthracene crystals to UV light was studied, and the results indicate strong reactivity at sites of surface defects, which is likely due to photodimerisation. A similar mechanism that described the behaviour of aspirin surfaces was suggested for this reaction.

In summary, both reactions that were studied provided a better insight towards understanding the solid-state reactivity of organic crystals. The proposed surface mechanisms imply that surface defects and the presence of humidity or solvent vapour are very likely to play a role in determining reactivity. Further studies on the origin of defects are suggested in order to better control the behaviour of organic crystals in the solid-state.

Contents

List of Figures	iv
List of Tables	x
1 Introduction to organic solids	1
1.1 Organic crystals and crystal engineering	1
1.2 Application of crystal engineering in pharmaceutical materials sciences	2
1.2.1 Studying drug components	2
1.2.2 Manufacturing solid-state dosage forms	3
1.3 The surface of organic crystals	5
1.3.1 Solid-solid interface	5
1.3.2 Solid-liquid interface	5
1.3.3 Solid-gas interface	6
1.3.4 Comparison of surface techniques	7
1.4 Thesis outline	8
2 Introduction to Atomic Force Microscopy	9
2.1 AFM: the fundamentals	9
2.1.1 Force-distance mode	10
2.1.2 Imaging mode	12
2.2 Literature review on studying organic crystals by AFM	16
2.2.1 AFM as an imaging method	16
2.2.2 Force-distance measurements: adhesion forces and sur- face energies	30
2.2.3 Nanoindentation techniques and mechanical properties of molecular crystals	31
2.2.4 Concluding remarks	37
3 A literature review on the hydrolysis of aspirin (ASA)	38
3.1 Bulk studies on the hydrolysis of ASA	39

3.2	Limitations of bulk studies	40
3.3	The anisotropy of crystal faces	41
3.4	Importance of surface studies on the solid-state hydrolysis of ASA	45
4	Experimental Methods	48
4.1	Optical microscopy	48
4.2	Attenuated total reflection – Fourier transform infrared spectroscopy	48
4.3	Powder X-ray diffraction	48
4.4	The Cambridge Structural Database and BFDH morphology prediction	49
4.5	Atomic Force Microscopy	49
4.5.1	Instrumental details	49
4.5.2	Cantilever selection and tip-to-sample force	50
4.5.3	Sample preparation and area of selection	51
4.5.4	Recording and processing AFM images	51
4.5.5	Surface roughness	53
4.5.6	Cross sectional analysis	53
4.6	Relating surface orientation to crystal structure	53
4.7	Controlled humidity environment	55
4.8	X-ray photoelectron spectroscopy	56
5	Organic surfaces imaged by AFM	58
5.1	Introduction	58
5.1.1	The nature of AFM imaging technique and organic crystals	58
5.2	Natural sublimation of organic crystals and the influence of the AFM tip	59
5.2.1	Preventing and determining the influence of the tip on areas imaged by AFM	66
5.3	Predicting surface sublimation	67
5.4	Chapter conclusion	70
6	Surface study of the solid-state hydrolysis of aspirin (ASA)	71
6.1	Introduction	71
6.2	Selecting a suitable ASA crystal surface	71
6.2.1	Sublimation growth	73
6.2.2	Fast evaporation of a saturated solvent	75
6.2.3	Slow solution growth	77

6.3	Following surfaces of ageing ASA crystal {001} face in different moisture levels	80
6.3.1	0% RH	82
6.3.2	Room humidity (<i>ca.</i> 40% RH)	82
6.3.3	50% RH	83
6.3.4	98% RH	84
6.3.5	Toluene atmosphere	85
6.4	Surface characterisation and bulk studies	86
6.5	Discussion	90
6.5.1	Proposed mechanism of surface product formation	93
6.5.2	Physical or chemical interaction?	93
6.6	Chapter conclusion	95
7	Following changes on crystal surfaces during photochemical reactions: A case study on anthracene	97
7.1	Introduction to solid-state photochemical reactions and the topochemical postulate	97
7.1.1	Anomalies of the topochemical postulate, <i>e.g.</i> AN	98
7.2	Experimental setup	100
7.2.1	Preparing AN crystals	100
7.2.2	Studying the photoreaction of AN surfaces	100
7.3	Experiments and results	101
7.3.1	Bulk photoreactivity of AN crystals	102
7.3.2	Surface photoreactivity of AN crystals	103
7.4	Dianthracene or anthraquinone?	113
7.5	Inconsistent rate of reaction at sites of defects	118
7.6	Chapter Conclusion	119
8	Conclusions	121
9	Bibliography	124

List of Figures

1.1	Schematic representation of two different packing structures based on the same molecule.	3
1.2	AFM image of aspirin (100) face	6
1.3	3-D height AFM images of ASA crystal surfaces prepared by different methods	7
2.1	Illustration of how the cantilever deflection is detected by a photodetector and laser beam.	10
2.2	A typical force distance plot with illustrations showing each stage of the ramping cycle.	11
2.3	Illustration of how AFM images are generated.	13
2.4	Schematic illustration of AFM contact imaging with a constant cantilever deflection	13
2.5	Schematic illustration of how frictional forces are detected by the cantilever lateral twisting motion in contact mode imaging. .	14
2.6	Illustration of phase signals in the AFM tapping mode arising from the phase difference between the driving vibration and the free end vibration.	15
2.7	AFM images of (melamine)·(cyanuric acid) crystal recorded in an aqueous solution saturated with melamine and cyanuric acid. .	18
2.8	AFM images of tetracene crystals with thicknesses of approximately 10 to 15 unit cell lengths.	18
2.9	Intermittent contact mode amplitude images showing the surface reconstruction of a spray-dried lactose particle after exposure to 58% RH.	19
2.10	Intermittent contact mode amplitude images of an anhydrous theophylline crystal after exposure to 65% RH.	20
2.11	Images of different polymorphs of ROY.	21
2.12	Determination of orientations of C ₃₂ H ₆₆ crystals on substrate surfaces via AFM.	21

2.13	Real-time <i>in situ</i> AFM height images of a L-cystine crystal surface.	23
2.14	AFM images of a (caffeine)·(oxalic acid) cocrystal stored at 75% RH.	24
2.15	AFM height images of the (001) plane of an ingestional drug molecule.	24
2.16	2-D and 3-D height images of a chocolate sample obtained at various storage times.	25
2.17	AFM images of the {110} face of paracetamol crystals.	26
2.18	AFM images of glycine crystals grown on a patterned self-assembled monolayer substrate.	27
2.19	AFM height and phase images of cimetidine polymorph A and B.	28
2.20	AFM images of (010) face of α -glycine etched by water and acetone.	29
2.21	Representative force distance plot for a budesonide particle on an AFM probe ramped onto a model mica surface.	30
2.22	Force distance measurement plots recorded between iron-coated tip and different profens.	31
2.23	Selected force distance plots for the three forms of carbamazepine, together with respective AFM height images of these forms.	32
2.24	Plot of hardness vs. maximum peak load on the cantilever for ascorbic acid, sucrose, lactose, and ibuprofen.	33
2.25	A correlation plot between particle hardness and powder compaction performance.	34
2.26	A hexachlorobenzene crystal bent along the (001) face, and the crystal packing of hexachlorobenzene.	34
2.27	Representative load versus depth-of-penetration curves of saccharin obtained with indentation normal to the (100) and (011) planes.	34
2.28	AFM height images of saccharin	35
2.29	AFM height images and Yong's moduli values of a photoactive cocrystal before and after photoreaction	36
3.1	ASA tablets aged in 80% RH and 50°C for 98 days, containing needle-shaped crystals of SA on the surface.	38
3.2	Typical ASA decomposition curve in the presence of humidity at 60°.	39
3.3	Crystal structure and predicted BFDH growth morphology of ASA.	42
3.4	AFM 3-D images of ASA (001) surface under dissolution.	42
3.5	AFM Deflection images of ASA (100) face etched by water, acetone, and ethyl acetate.	44

3.6	Carbon and oxygen 1s XPS of ASA crystal faces, showing the deconvoluted C and O environments.	44
3.7	AFM image of (001) and (100) after nanoindentation.	45
3.8	The measured force of adhesion values at different RH levels between dicalcium phosphate probes and ASA.	46
3.9	AFM height profile of ASA before and after dicalcium phosphate contact.	46
3.10	AFM amplitude profile of ASA (001) under ambient conditions before and after contact with dicalcium phosphate.	47
4.1	Picture of the Multimode AFM instrument with labelled parts. .	49
4.2	3-D height profile of a standard calibration grid ($50 \times 50 \mu\text{m}^2$). .	50
4.3	Optical microscope and AFM images of two aspirin crystal surfaces treated under different conditions	52
4.4	Illustration of how the height of features can be analysed by cross sectional plots.	54
4.5	1-D XRD spectra of experimental ASA crystals compared to simulated PXRD pattern of ASA form I	55
4.6	Picture of two sections of a large single crystal prepared by cleaving along the length of the crystals. The crystals were glued onto coverslips that were attached to stainless steel discs.	55
4.7	Schematic illustration of a 1-D X-ray diffraction on coverslip containing crystals to be studied by AFM, with most crystals having the dominant face on top.	56
4.8	Crystal structure of ASA viewed onto $\{100\}$ compared to the optical microscope image of the crystal surface prepared by quick evaporation.	56
5.1	Four consecutive AFM height images of a benzamide crystal surface.	59
5.2	Optical microscope images of organic crystals formed on coverslips.	60
5.3	1-D XRD pattern of organic crystals grown on coverslips and the corresponding simulated powder pattern.	60
5.4	AFM height images of AN (001) surface before and after continuous imaging.	62
5.5	AFM height images of SA (011) surface before and after continuous imaging.	63
5.6	AFM height images of ASA (100) surface before and after continuous imaging.	64

5.7	AFM height images of TP (200) surface before and after continuous imaging.	65
5.8	Representative AFM amplitude image of SA (011) and AN (001).	66
5.9	Schematic illustration of the 2-D nucleation energy model and the sublimation of molecules at step edges and kinks.	67
5.10	Histograms of the binding energy calculations for selected organic crystals based on the 2-D nucleation morphology prediction model.	69
6.1	Crystal structure of ASA form I viewed along the [010] direction.	71
6.2	The BFDH morphology prediction of ASA form I crystals	72
6.3	1-D XRD scans of ASA crystals grown by different methods.	73
6.4	Schematic illustration of ASA crystal growth by sublimation, and photos and optical microscope images of crystals obtained by this method.	74
6.5	Representative AFM height profile of an ASA {100} crystal surface grown by sublimation.	75
6.6	Optical microscope and AFM images of ASA crystals prepared by rapid evaporation, together with ASA crystal structure viewed along the [100] direction.	76
6.7	ASA Crystals of mixed morphologies grown from solution.	78
6.8	A representative AFM height image of the ASA (100) surface and a cross sectional height analysis.	78
6.9	ASA {001} face prepared by cleaving long crystals along the cross sectional area, together with a schematic illustration of the morphologies of ASA crystals.	79
6.10	A representative AFM height image of a cleaved {001} surface and a cross sectional analysis on the surface.	79
6.11	A representative AFM height image of a freshly cleaved {001} surface , together with a cross section analysis at the surface.	82
6.12	A representative AFM image of an ASA surface aged in 0% RH for two months.	83
6.13	A representative AFM image of an ASA surface aged at room humidity for two months.	84
6.14	A representative AFM image of an ASA surface aged at 50% RH for two months.	85
6.15	Representative AFM images of an ASA surface aged at 98% RH for two months.	86

6.16	Two representative AFM images of an ASA surface aged in toluene atmosphere for two months.	87
6.17	A representative AFM image of an ASA surface aged in 98% RH and 40°C for one week in preparation for XPS studies.	88
6.18	Theoretical and experimental carbon 1s XPS spectrum of ASA and SA.	89
6.19	PXRD patterns of ground ASA samples compared to simulated patterns.	91
6.20	ATR-FTIR spectra of ground ASA samples compared to SA (as purchased).	91
6.21	Representative 3-D height profiles of ASA {001} surface stored under different conditions for two months.	92
6.22	(a) 3-D illustration of the mechanism of surface product formation; (b) Amplitude image of a sample {001} surface aged in room RH with labelled crystal orientation ($5 \times 5 \mu\text{m}^2$).	94
7.1	Three types of crystal structure classification based on the geometric relationship between neighbouring molecules.	97
7.2	Photodimerisation scheme of AN.	98
7.3	A unit cell in the crystal structure of AN.	99
7.4	Polarised optical microscopy images of AN crystals obtained by recrystallisation from ethyl acetate.	100
7.5	Set up of AFM imaging next to a UV-A light source.	101
7.6	Set up for AFM study under controlled humidity level.	101
7.7	Picture of AN crystals before (left) and after (right) exposure to UV light for 1 week.	102
7.8	PXRD patterns of experimental AN crystals compared to simulated patterns.	102
7.9	ATR-FTIR patterns of AN before and after exposure to UV, and ANQ (as purchased).	103
7.10	Amplitude AFM images of an AN surface before and after storage in the dark.	104
7.11	Amplitude images of AN crystal surface before and after exposure to UV light.	105
7.12	3-D Height profile of continuous AFM imaging on AN (001) surface exposed to UV.	107
7.13	Height profile of continuous AFM imaging on AN (001) surface exposed to continuous UV.	108

7.14	Amplitude and 3-D height profile of a larger area at the same position that was repeatedly imaged previously in Figure 7.12 and 7.13.	110
7.15	Amplitude profile of an AN (001) surface exposed to UV under dry conditions before and after 24 hours.	112
7.16	Amplitude profile of an AN (001) surface exposed to UV under ambient humidity before and after 24 hours.	114
7.17	Schematic 2-D illustration of the surface relaxation on a flat crystal surface and at step or pit features.	115
7.18	Amplitude profiles and 3-D height profiles of an AN (001) surface exposed to UV at different time intervals.	116
7.19	Amplitude profile of a larger area after the continuous imaging period.	118

List of Tables

2.1	Mechanical properties of particles of pharmaceutical materials determined by AFM nanoindentation	33
5.1	Sublimation enthalpy of selected organic crystals.	67
6.1	Solubility of ASA and SA in water and toluene at room temperature.	95

List of Abbreviations

AN	Anthracene
ANQ	Anthraquinone
API	Active pharmaceutical ingredient
ASA	Aspirin
ATR	Attenuated total reflection
BFDH	Bravais-Friedel-Donnay-Harker model
CSD	Cambridge Structural Database
DSC	Differential scanning calorimetry
DPI	Dry powder inhaler
F_{adh}	Force of adhesion
F_{load}	Loading force
F_{res}	Restoring force
FTIR	Fourier transform infrared spectroscopy
IGC	Inverse gas chromatography
k_{cant}	Spring constant of an AFM cantilever
NC-AFM	Non-contact AFM
PXRD	Powder X-ray diffraction
RH	Relative humidity
Rq	root mean square surface roughness
SA	Salicylic acid
TGA	Thermogravimetric analysis
TP	Theophylline
UHV	Ultra high vacuum
W_{adh}	Work of adhesion
XPS	X-ray photoelectron spectroscopy
γ	Surface energy

Chapter 1

Introduction to organic solids

1.1 Organic crystals and crystal engineering

Organic crystals play a crucial part in numerous industries. Commodity goods that are used in our everyday lives, including dyes, food, pharmaceuticals, agricultural agents often contain organic crystals. In order to improve the use of organic crystals, it is important to understand their solid-state properties, whether if it is to synthesize novel materials, develop more cost-effective manufacturing procedures, achieve better quality control, or boost the stability and performance of end-product. The solid-state properties of organic crystals are influenced by their supramolecular structure, which is studied by crystal engineering.

The concept of crystal engineering was introduced in 1971 [1], which subsequently was defined as “*the understanding of intermolecular interactions in the context of crystal packing and in the utilization of such understanding in the design of new solids with desired physical and chemical properties*” [2, 3]. Among others, such interactions include hydrogen bonding, halogen bonding, as well as π - π interactions [4]. By understanding the behaviour of these interactions, crystal engineering was developed not only for the study of crystal structures, but also for the rational design of crystalline materials using concepts like supramolecular synthons and molecular self-assembly [5]. This approach has been broadly employed in chemistry and materials science, drug industry, and nanotechnology [6, 7].

Crystal engineering has advanced rapidly over the last few decades, where several new robust supramolecular synthons have been identified, leading to a better understanding of how molecules assemble in the solid-state. This has enabled new crystalline architectures to be synthesized more by rational design than by trial-and-error. In particular, one of the most active developments

in crystal engineering is the pursuit of pharmaceutical cocrystals [2, 5] with improved properties such as solubility [8, 9], stability [10], dissolution rate [11], and bioavailability [12–15].

1.2 Application of crystal engineering in pharmaceutical materials sciences

As the pharmaceutical industry has benefited from the advances in crystal engineering, an introduction should be given to pharmaceutical materials sciences, which is a field of research that studies the structure, manufacture and performance of drugs. As solid dosage forms are the major method of drug delivery on the market, it is important that when developing a pharmaceutical product, not only must the drug be targeted to the correct site in a human cell or organ, it is also important to learn about the physical and material property of the dosage form. For example, a tablet would not be a desirable form of drug delivery if it disintegrated before consumption, and any commercial drug containing unstable ingredients which are easily converted to undesirable or unknown forms is unacceptable.

1.2.1 Studying drug components

Molecules form crystals, which form particles, and eventually dosage forms. By learning about the fundamental behaviour of molecules of each drug component, a strategy can be developed to relate molecular properties to the crystal structure, and eventually dosage performance. A drug is usually made up of two or more components, namely an active pharmaceutical ingredient (API), and one or more excipients. While API molecules have the chemical functionality that provides the desired pharmaceutical effect to the body, excipients are other components that are pharmaceutically inactive, which are often employed for a variety of functions, such as diluents, tablet coating, flavouring and colouring [16].

Regardless of whether the drug components are crystalline or amorphous materials, their stability is one of the most important properties to be considered, as it is crucial for each component to perform specific functions without undergoing unwanted side reactions that affect drug performance. Amorphous materials often have an advantage of greater solubility and bioavailability due to their high-energy state compared to crystalline materials [17], however this high-energy state can be unstable and convert to crystalline form. Although

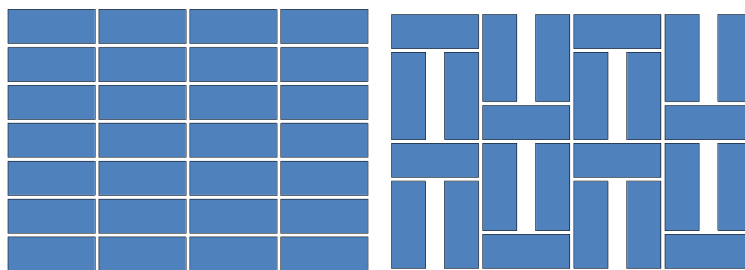


Figure 1.1: Schematic representation of two different packing structures based on the same molecule (represented by the block).

crystalline materials are more stable due to a structured arrangement of atoms or molecules with long range order, very often a chemical entity can exist in more than one crystalline form, in which each form is different from one another in the packing pattern. This phenomenon is known as polymorphism (Figure 1.1), which is often known to exist for APIs and excipients. Different polymorphs of the same API molecule can have different physicochemical properties, and will most certainly affect drug performance if the polymorph used in formulation changes. Therefore, a considerable amount of research effort has been made to screen for polymorphs to ensure that the selected form is stable and will not convert to another polymorph during manufacturing and distribution.

1.2.2 Manufacturing solid-state dosage forms

The most common type of solid-state dosage form is tablets, which are often composed of a certain amount of API dosage mixed and compressed with some filler excipient. The main advantages are their good chemical stability, cost-effective manufacturing, simple packaging and administration. Another type of solid-state dosage is dry powder inhalers (DPIs), which are administered via a respiratory route, and uses the inhalation force of patients to deliver the drug particles to the lungs [18, 19]. The advantage of this route over the oral route is that the high contact area to volume ratio between blood vessels and the airstream in the lungs allows fast absorption of the drug into the blood stream, and does not require passing through the digestive system. For orally administered drugs the drug may be converted metabolically even before entering the blood stream.

A few common manufacturing processes are outlined below. Extensive research is carried out to ensure that the drug ingredients do not undergo any undesirable reactions during each step, as a change of form in any ingredient of a commercial drug puts the drug at risk of withdrawal from the market, with

subsequent loss to the company and patient. Ritonavir, marketed by Abbott Laboratories with the trade name Norvir is an example of polymorphism hindering the sales of a drug. In this case a new polymorph was discovered after the drug was marketed, leading to a halt in production and loss of revenue [20].

Crystallisation

Crystallisation is usually the first solid-state process to purify the required molecule formed from previous chemical reactions. During crystallisation, solvent and other impurities are removed. Under different conditions, such as different temperature or pressure, the molecule can crystallise in different polymorphs, or as an amorphous form.

Particle size reduction

Besides polymorphism, different crystallisation conditions also affect the particle size of the crystals. The distribution of particle size needs to be made more uniform to yield better compression and flow properties for tableting. This is also particularly important for manufacturing DPIs, as a particle size of less than 5 μm is normally required in order to allow API particles to be deposited at the tracheobronchial and pulmonary regions of the lung [18, 19]. Excipients, for example, lactose monohydrate, with a typical particle size of 30 - 90 μm [21], are usually added to act as inert carriers of the small API particles, which improve the flow characteristics of the drug, and prevents aggregation of particles to allow easier handling of the drug [8].

While micronisation is a possible way to achieve this by breaking down large particles with high energy impact, there is also an accompanying risk of change in polymorph or the creation of amorphous material [22, 23].

Wet or dry granulation

Excipient molecules are mixed with API molecules by wet or dry granulation, depending on whether a liquid is added or not. This aims to produce a homogeneous mixture of materials before further processing. As the API and excipient are brought into direct contact, it is important to address the compatibility between the drug components.

Compression

The compression of the homogeneous drug component mixture is usually carried out with a tablet press. A large pressure is exerted to press the mixture

into tablet shape. This impact force is high in energy, and may induce changes to the API or the excipient [24]. Drug components with good flow and compression properties sometimes do not have to go through all of the above processes, and can be mixed together and directly compressed to form tablets. Therefore, it is desirable to develop API and excipients with better physicochemical properties, which can in turn reduce manufacturing time and costs.

1.3 The surface of organic crystals

Crystal engineering has not only played a significant role in the development of pharmaceutical material sciences, as demonstrated in the previous section, but it has also provided significant impact to several other industries. While the majority of studies in this field has focused on designing crystalline materials with improved bulk properties, significantly less studies have been devoted to studying the surface of crystals. As most organic solids are manufactured in the form of powders, especially in the pharmaceutical industry, given a high surface area to volume ratio, the surface must play an important role in governing the behaviour of these materials. Moreover, several reactions occur at interfacial contacts:

1.3.1 Solid-solid interface

During manufacturing procedures such as micronisation or granulation, particles are broken and new surfaces are exposed. Different drug components are mixed together and brought into close contact. The balance between the adhesion and cohesion forces of different particle surfaces must be optimised in order to prevent bad flow properties of the materials, as well as problems such as particle agglomeration. Moreover, any incompatibility between drug components must be identified. This is particularly important during tablet compression, as surfaces are being compressed onto one another with high impact energy, which may induce reaction between particle surfaces.

1.3.2 Solid-liquid interface

Although solution crystallisation is a simple procedure, there is a lack of fundamental understanding of how dissolved molecules in the solvent are deposited onto the growing crystal interface. Crystal growth is not only affected by the growth conditions (*e.g.* temperature, pressure, and supersaturation), but is also further complicated by factors such as the interactions between molecules

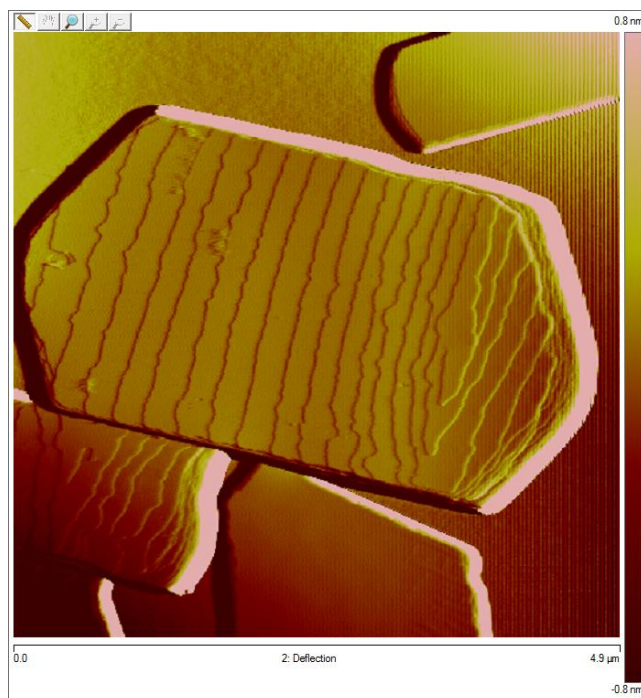


Figure 1.2: An AFM deflection image of an aspirin (ASA) (100) crystal surface, showing a screw dislocation, together with step features of approximately 1 nm in height. The imaged area is $4.9 \times 4.9 \mu\text{m}^2$

and different solvents used for crystallisation, and the presence of defects at the interface. Studying the surface of organic crystals can provide insight towards understanding crystal growth, in particular, what determines the growth rate of different crystal faces, and how defects affect crystallisation (Figure 1.2).

On the other hand, the dissolution of a crystal also occurs at the solid-liquid interface, which is strongly related to the bioavailability of drugs in the human body.

1.3.3 Solid-gas interface

Many drugs are susceptible to degradation in the presence of oxygen or humidity. As only molecules at the surface level of crystals or particles are exposed to air, the degradation is expected to occur at this solid-gas interface. Factors that could affect this reaction might include the number of defects the surface contains, and the topography and roughness of the particle surface.

In the past, most studies regarding solid-state reactions have often employed bulk techniques such as powder X-ray diffraction (PXRD), differential scanning calorimetry, thermogravimetric analysis, as well as several spectroscopy techniques. However, these bulk techniques cannot detect the surface response of solids. As shown in Figure 1.3, atomic force microscopy (AFM) images of aspirin (ASA) surfaces prepared by different methods can show very differ-

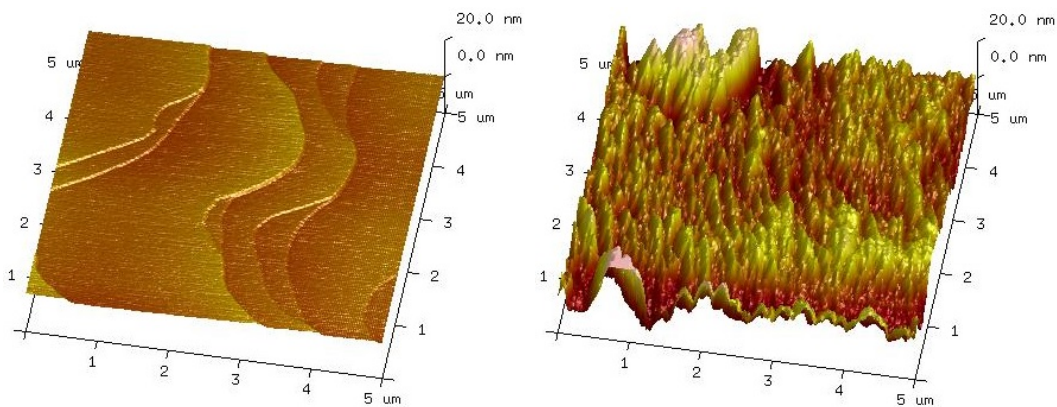


Figure 1.3: 3-D height AFM images of two ASA crystal surfaces, grown by (a) sublimation (b) solution crystallisation. The displayed images have the same height range of 40 nm. A significant difference in roughness was observed between the two surfaces, possibly influencing the reactivity of each sample. The imaging area is $5 \times 5 \mu\text{m}^2$.

ent surface topography and roughness, which cannot be detected by any bulk characterisation techniques. In order to fully understand solid-states reactions, alternative techniques are required to study the behaviour of solid surfaces.

1.3.4 Comparison of surface techniques

The currently available techniques for surface characterisation of materials include contact angle measurements and inverse gas chromatography (IGC). While contact angle measurements are limited in detecting heterogeneity and require a flat surface for accurate measurements, IGC is not surface-specific and gives only average information of the overall surface. Optical microscopy is useful in visualising surfaces, but its resolution is limited by the wavelength of visible light. Electron microscopes provide higher resolution due to the smaller wavelength of the electron beam, but often the high beam flux causes organic samples to decompose quickly during data acquisition. With the introduction of AFM, which was first reported in 1986 [25], non-destructive, high resolution surface studies were made possible, allowing the direct visualisation and analysis of solid surfaces.

As the use of AFM in studying organic crystals is a relatively new technique that has emerged in the past two decades, there are many areas where progress is yet to be made. This thesis aims to address some of these areas, and demonstrate the invaluable insight that AFM can provide to our understanding of crystal engineering and organic crystals.

1.4 Thesis outline

In Chapter 2, an introduction to AFM is given, followed by a literature review of the use of AFM in studying organic crystals.

Chapter 3 is a literature review on ASA and its solid-state hydrolysis to form salicylic acid (SA). Past studies involving the hydrolysis of ASA is presented, followed by a discussion involving the anisotropy of different ASA crystal faces, which highlights the importance of studying the solid-state hydrolysis on crystal surfaces.

Chapter 4 is a description of all the experimental methods used to obtain the results for this thesis. This is followed by Chapter 5, which presents a study that explores the limitations of the AFM in studying organic crystals. Due to the nature the technique and organic crystals, surface changes observed by AFM may be influenced by the tip as well as the natural sublimation of organic crystals. Precautions need to be taken to determine the extent of these effects, in order to identify the surface response that corresponds to changes to the experimental conditions.

Based on the literature review in Chapter 3, Chapter 6 presents a detailed investigation on the reactivity of ASA crystal surfaces. Studies involving the storage of (001) surface under different humidity conditions are discussed, and a suggested mechanism that describes the observed surface reactivity of ASA is given.

The photochemical reaction of anthracene (AN) crystals is explored in Chapter 7. This reaction is forbidden by the well known topochemical postulate, and therefore challenges the fundamental concepts in crystal engineering. With the use of continuous AFM imaging to study AN surfaces, this will give a better insight towards understanding the reason of this unexpected photoreactivity. A surface mechanism similar to the previous chapter is proposed to explain the photoreactivity of AN, which does not necessarily contradict with the topochemical postulate.

This thesis ends with a conclusion chapter, where all the ideas and progress presented throughout the thesis are tied together, and future work in the study of organic crystals is suggested.

Chapter 2

Introduction to Atomic Force Microscopy

This chapter aims to provide a thorough background on atomic force microscopy (AFM) and the use of this technique in studying organic crystals, which will put the research material in later chapters into context. An overview of how the AFM operates will be first presented, followed by a literature overview on the use of AFM in studying organic solids, which has proved to be an invaluable tool for understanding the fundamentals of how organic solids behave.

It is noted that most of the material in this chapter is taken from the following review article recently published by our group (Reference [26]):

E. H. H. Chow, D.-K. Bucar, and W. Jones. New opportunities in crystal engineering - the role of atomic force microscopy in studies of molecular crystals. *Chem. Commun.*, 48(74):9210-26, September 2012

2.1 AFM: the fundamentals

AFM belongs to the family of scanning tunnelling microscopy, which relies on a physical probe to explore the surface of interest. The AFM “feels” atomic forces, such as electrostatic or van der Waals forces between the tip and the sample, by the deflection of the cantilever on an AFM probe. A restoring force (F_{res}) (*i.e.* the force required to restore the cantilever to its equilibrium position) balances these forces. Given the spring constant of the cantilever (k_{cant}), and using Hooke’s Law, F_{res} can be determined from the corresponding cantilever deflection (dz), where the z-axis is defined to be the direction along the interactive force between the sample and the tip:

$$F_{res} = -k_{cant}dz \quad (2.1)$$

Measuring dz can therefore allow F_{res} and the corresponding tip-to sample interaction to be determined.

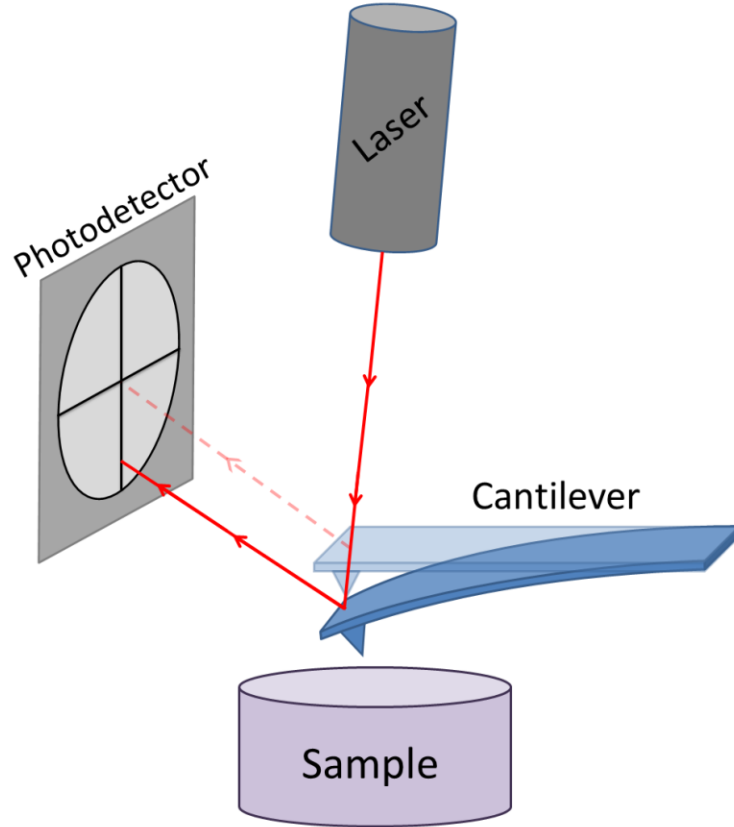


Figure 2.1: Illustration of how the cantilever deflection is detected by a photodetector and laser beam. Adapted from reference [26].

Nowadays, the cantilever deflection is normally detected by a visible laser beam reflecting off the back of the cantilever onto a photodiode detector (Figure 2.1) [26]. The degree of bending can then be traced by monitoring the displacement of the laser beam on the photodiode. The tip can be controlled to scan an area of the sample, with a resolution depending on the cone angle and radius of curvature of the tip, which are typically 30° and 10 nm respectively. There are two main AFM operating modes: the force-distance mode and imaging mode.

2.1.1 Force-distance mode

Force-distance curves are generated by bringing the probe and sample into contact while applying a particular force, and subsequently pulling them apart.

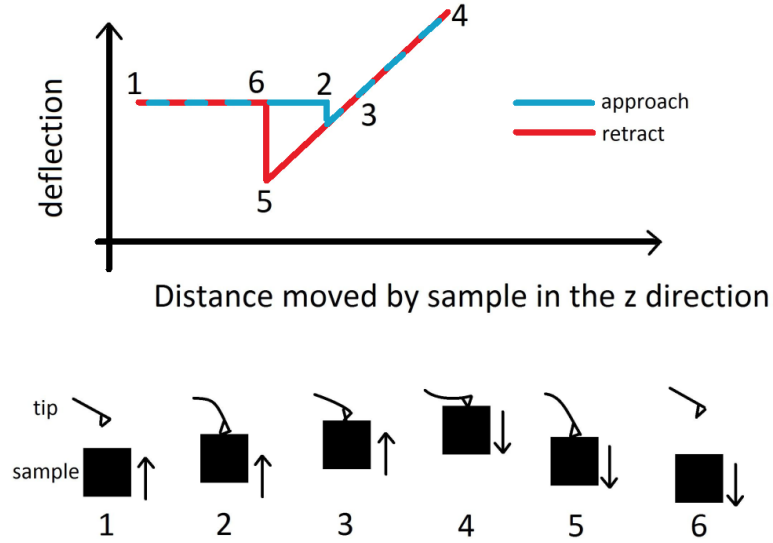


Figure 2.2: A typical force distance plot with illustrations showing each stage of the ramping cycle (stages 1-6). Arrows indicate sample movement towards the tip. Adapted from reference [26].

The measured cantilever deflection is plotted against the vertical probe-to-sample distance in the z direction. A typical force-distance curve is illustrated in Figure 2.2 [26]. Initially the probe is far away from the sample such that there is no interaction between the sample and the tip (stage 1). As the distance between the tip and the sample is reduced, the attractive forces between the two increases, but does not overcome F_{res} and the deflection remains unchanged. As the separation decrease the attractive forces eventually overcome F_{res} , which causes the cantilever to deflect and “jump” into contact with the sample (stage 2). The cantilever then returns to its undeflected position at a closer distance between the tip and sample (stage 3). As the force exerted by the tip against the sample increases, the cantilever deflects away from the sample. The pressing motion introduces a loading force, F_{load} , which acts against F_{res} (between stage 3 and 4).

No indentation will occur if both the tip and sample are hard materials, and F_{load} will only cause the cantilever to deflect more. This will yield a linear plot between stages 3 and 4, which is defined as the constant compliance region. At the end of the loading cycle (stage 4), the retracting plot follows the reverse of the approach curve initially, returning to point 3. Further retraction causes the cantilever to deflect towards the sample as the tip and sample are still bound together by attractive forces (between stages 3 and 5). When F_{res} overcomes the attractive forces, the tip separates from the surface (stage 5), and the cantilever returns to its undeflected position (stage 6).

The ramping cycle is completed when the retraction returns to stage 1,

which can be repeated for more accurate and consistent measurements. Although the resolution of the deflection along the z-axis can be as small as 10^{-4} Å [27], mechanical vibration lowers the resolution to approximately 0.1 Å in practice [28].

The force of adhesion or cohesion is one of the pieces of information that can be obtained from force-distance measurements. The force of cohesion is the attractive force between the same materials, whereas the force of adhesion (F_{adh}) is the attractive force between different materials. Both can be deduced from force-distance plots as they are represented by F_{res} , which by Hooke's Law is related to the change in deflection measured between stages 5 and 6. This technique can be performed on a wide range of materials simply by varying the materials of the tip and sample.

The force of cohesion or adhesion is often used to estimate other useful quantities, such as the work of adhesion, and surface energy. To obtain the work of adhesion (W_{adh}) or cohesion, the contact area between the sample and the tip must be determined, together with suitable contact models such as the Johnson-Kendall-Roberts model [29], or the Derjaguin-Muller-Toporov model [30]. The surface energy can then be calculated using the equation:

$$W_{adh} = 2\sqrt{\gamma_1\gamma_2} \quad (2.2)$$

Here, γ_1 and γ_2 are the surface energies of the material on the tip (1) and the sample (2) respectively.

2.1.2 Imaging mode

The sample is raster-scanned when the AFM is operating in imaging mode. The tip is moved back and forth continuously along the fast axis (*i.e.*, x-axis), while along the slow axis (*i.e.*, y-axis) the tip moves in small increments after each complete line of scanning along the fast axis. This allows an area of the surface to be traced by the tip (Figure 2.3) [26]. A feedback signal is used to maintain a constant force between the tip and the sample, allowing the tip to track the surface topography as well as preventing the tip to retract or collide with the sample surface. There are three basic imaging modes: contact mode, intermittent contact mode, and non-contact mode. They differ in the used feedback signal, and the tip-to-sample distance set for imaging.

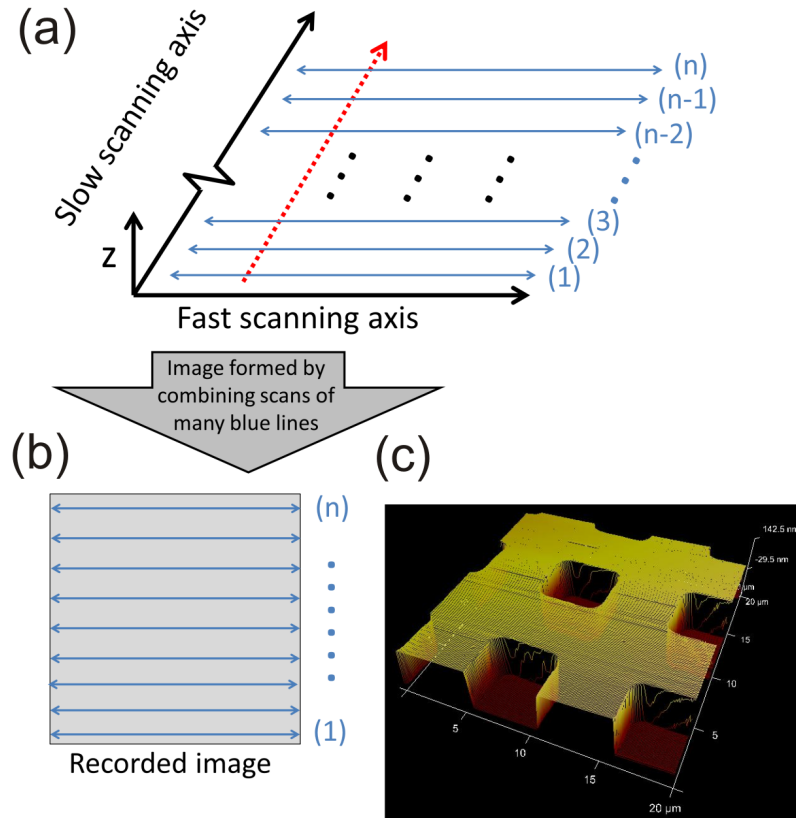


Figure 2.3: Generation of AFM images through scanning along the fast axis (a, b), and an 3-D height projection image depicting a calibration grid (c) (an artificial light source and a false colour scheme were utilized to highlight the topological features of the grid). Adapted from reference [26].

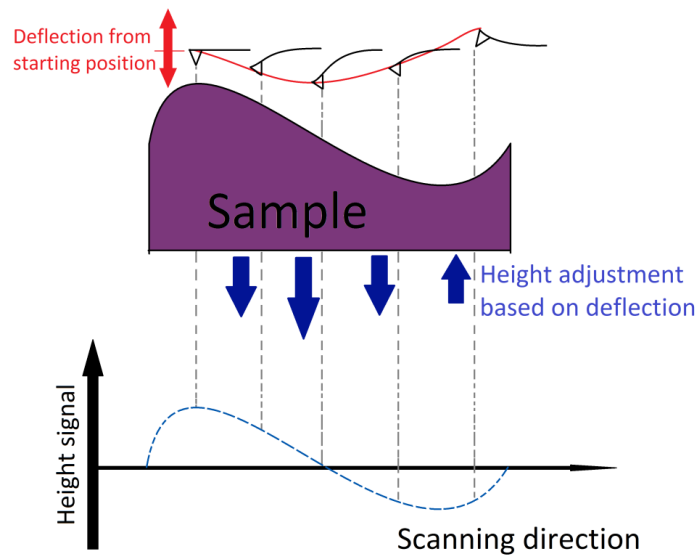


Figure 2.4: Schematic illustration of AFM contact imaging with a constant cantilever deflection, whereby the deflection acts as feedback to adjust the tip-to-sample distance. Adapted from reference [26].

Contact mode

In contact mode, the force applied is fixed to a certain value within the constant compliance region as described in Figure 2.2, which is called the deflection

setpoint. The cantilever deflection is maintained as close as possible to this value by the software of the instrument. The change in deflection can be interpreted as a change in topography, which is recorded together with the corresponding topography data to produce the deflection and height output signal respectively (Figure 2.4).

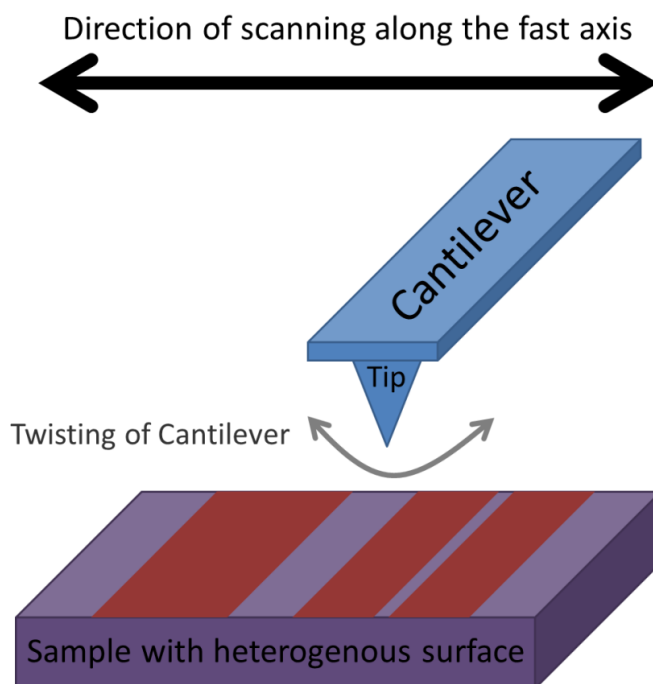


Figure 2.5: Schematic illustration of how frictional forces are detected by the cantilever lateral twisting motion in contact mode imaging. Adapted from reference [26].

A friction signal can also be obtained in addition to the deflection and height outputs. This is detected by the lateral twisting of the cantilever. If the cantilever is positioned perpendicular to the fast axis, then any changes in the lateral force exerted on the tip can be recorded (Figure 2.5), and can be interpreted as the frictional force between the tip and sample.

Probes used for contact mode imaging should have a cantilever with a low force constant, typically 0.15 Nm^{-1} , to minimise the damage to the surface, and to increase the range of deflection in response to atomic forces for better sensitivity. The deflection setpoint is normally optimised to reduce surface damage while imaging, especially for soft organic samples that can be easily scratched by the tip. When samples are found to be unsuitable for contact mode imaging, intermittent contact mode or non-contact mode are alternative imaging methods that are less destructive to the sample.

Intermittent contact mode

Intermittent contact mode is commonly known as tapping mode. It requires the base of the cantilever to be set on oscillation slightly below its resonance frequency by applying a drive amplitude, which sets the free end of the cantilever oscillating with a fixed amplitude in free space [31]. The laser and photodiode detect the amplitude of the free cantilever end, which is a function of the drive amplitude and the quality factor of the cantilever. This quality factor depends on the dimensions and material of the cantilever, as well as the surrounding environment.

The free end amplitude decreases as the tip and the sample are brought closer together, as energy is dissipated from the oscillating tip to the sample. The amplitude setpoint can be defined such that the system always adjusts the amplitude as close as possible to this setpoint by varying the tip-to-sample distance during scanning. This allows the tip to trace the surface at constant energy dissipation from the tip to the sample, yielding a height output signal. The amplitude out signal is analogous to the constant deflection signal in contact mode, and is also recorded.

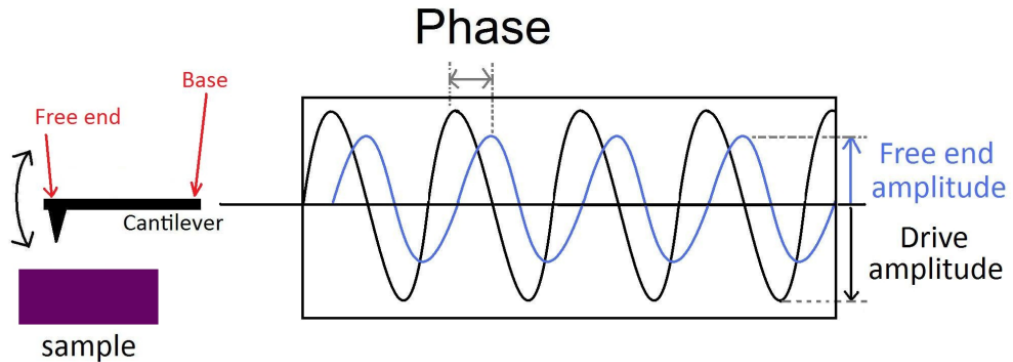


Figure 2.6: Illustration of phase signals in the AFM tapping mode arising from the phase difference between the driving vibration and the free end vibration. Adapted from reference [26].

A phase signal can also be obtained by intermittent contact mode. This originates from the phase difference between the driving vibration at the base and the free end vibration. If the cantilever is oscillating freely in space, this phase difference is expected to be 90° [32]. Any interaction between the tip and sample will induce a greater phase contrast, giving rise to the phase signal output (Figure 2.6) [26]. The phase contrast usually arises from different physiochemical properties of the sample surface [33]. However, the phase signal must be interpreted carefully, as it is also affected by many factors, including the surface roughness and topography [34].

Typical probes used for intermittent contact mode have cantilevers with force constants of around 40 Nm^{-1} , which are much stiffer than those used in contact mode. The increased stiffness reduces cantilever deflection, as very large cantilever deformations will lead to an inaccurate measurement [35]. Generally, better height resolutions along the z-axis are achieved by intermittent contact mode over contact mode, as the oscillation allows the tip to trace the surface without being “stuck” to any fluid layers such as the adsorption and condensation of water molecules in the presence of moisture.

Non-contact mode

In non-contact AFM (NC-AFM), the tip is oscillated at either its resonant frequency or just above, but is not in contact with the sample. This technique was first reported by Martin *et al.*, who obtained precise force measurement between the tip and sample over a tip-sample distance range of 3 to 18 nm [31]. By maintaining a constant tip-sample spacing by frequency modulation, imaging with a spatial resolution of 50 \AA was achieved. Later studies with NC-AFM allowed the true atomic resolution under ultra high vacuum (UHV) conditions [36, 37].

Despite the advantage of no sample damage caused by the tip, as well as the highest resolution amongst all three modes hereby mentioned, the biggest disadvantage of NC-AFM is the requirement of UHV conditions. This is often not suitable for studying organic crystals, as these conditions would significantly promote sublimation of surface molecules on these crystals. This mode would also be complicated for *in situ* studies on organic crystals.

2.2 Literature review on studying organic crystals by AFM

There has been a rapid development in the use of AFM in many scientific fields since its invention, which is demonstrated by the numerous reviews on this subject [26, 28, 37–49]. This literature review will focus on the use of AFM to study organic crystals in particular.

2.2.1 AFM as an imaging method

The subsections below will emphasise the high utility of AFM imaging in examining a broad range of physicochemical phenomena of high interest in organic solid-state chemistry. AFM imaging can be performed both *in situ* and *ex situ*.

While simple *ex situ* imaging provides useful information regarding surface behaviour, *in situ* imaging often gives better insight when analysing surface response to variations in humidity and temperature, or even the reaction between a fluid medium and the solid sample.

Crystal-growth mechanisms

Crystal properties such as defect content, morphology, purity, are determined at early crystal growth stages, and are strongly influenced by crystallisation conditions and crystal-growth substrates. AFM has proven to be an excellent tool in studying the early stages of crystal growth, and providing critical insights into crystal nucleation and the growth of macromolecules and small organic molecules [50]. Both macromolecules and small organics can be easily damaged during AFM studies, as such damage can be caused by strong mechanical forces exerted on the crystal surface [51], or capillary forces between the tip and the sample [52]. To minimise the damage of structural features on soft crystal surfaces, AFM can be performed in a controlled environment (*e.g.* lowering the operating temperature so that the material is less likely to melt) such that the surface to be monitored in real time with minimum destruction of surface features [38].

Real time *in situ* AFM studies permitted the study of the crystal growth mechanism of (melamine)·(cyanuric acid) cocrystals in water (Figure 2.7) [53]. The highly insoluble cocrystal was found to precipitate in kidneys which caused renal failure in humans and animals [54, 55]. X-ray diffraction and crystal morphology prediction techniques were used to identify the {110} as the largest crystal face. The fastest growth axis was normal to (201) which is parallel to the 2-D (melamine)·(cyanuric acid) sheets. This fastest growing direction was attributed to hydrophobic forces that minimized the surface of the 2-D hydrophobic molecular sheets in water. The slow crystal growth parallel to (201) was attributed to the ability of water molecules to inhibit the 2-D expansion of the (melamine)·(cyanuric acid) sheets running parallel to (201) (Figure 2.7). Hydrophobic forces and the fast stacking of the (201) sheets were thus responsible for the cocrystal growth along the *c*-axis in aqueous conditions. Such findings could be helpful in the development of remedies for urolithiasis.

Another AFM-based example of determination of crystal growth mechanisms is found amongst studies of polycenes. Naphthalene, anthracene (AN) and tetracene were sampled to elucidate factors that impact their crystal growth and morphology [56]. Experimental and computational studies revealed that screw dislocations on {001} have a crucial role in the crystal growth perpen-

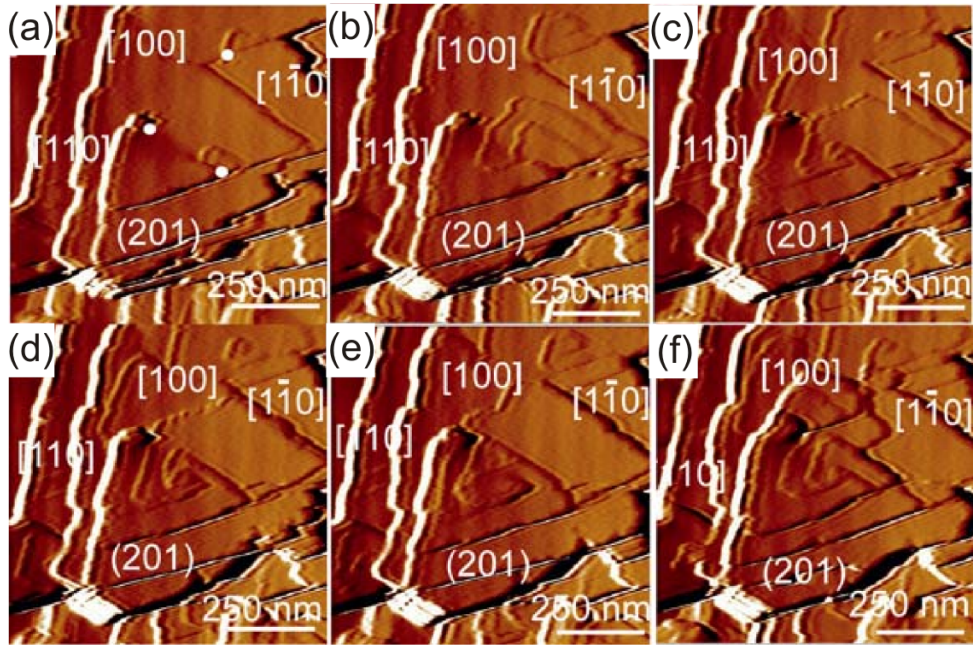


Figure 2.7: AFM contact-mode images of the (201) face of a (melamine)-(cyanuric acid) crystal recorded in an aqueous solution saturated with melamine and cyanuric acid: (a) 20 min after addition of solution to the AFM cell, (b) 20 min and 40 s, (c) 21 min and 30 s, (d) 22 min, (e) 22 min and 30 s and (f) 23 min. The white dots in (a) indicate dislocation points. Growth directions of the crystal with respect to the AFM frames are depicted in white. Adapted from reference [53].

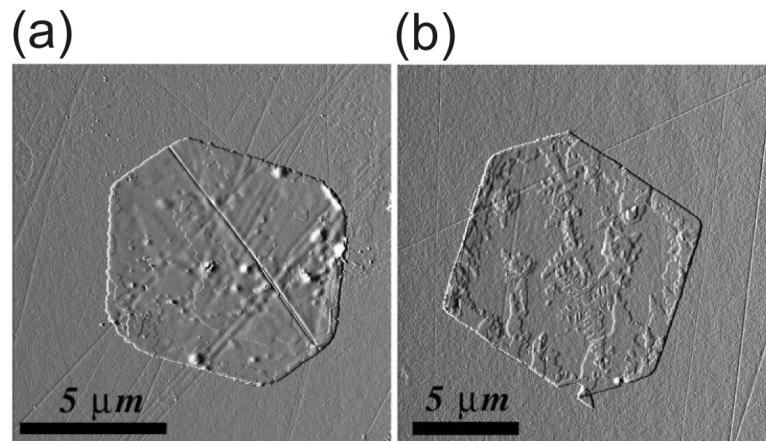


Figure 2.8: AFM images of tetracene crystals with thicknesses of approximately 10 to 15 unit cell lengths. Adapted from reference [56].

dicular to this face. The absence of screw dislocations was shown to preclude the growth of crystals with low aspect ratios, and to facilitate the growth of extremely thin platelets of several unit cell thick (Figure 2.8).

In the same study, crystal-growth conditions that govern the formation of screw dislocations, and thus the morphology development of the crystal were

also identified. These findings are likely to facilitate the development of single-crystalline thin films of technological relevance [57, 58].

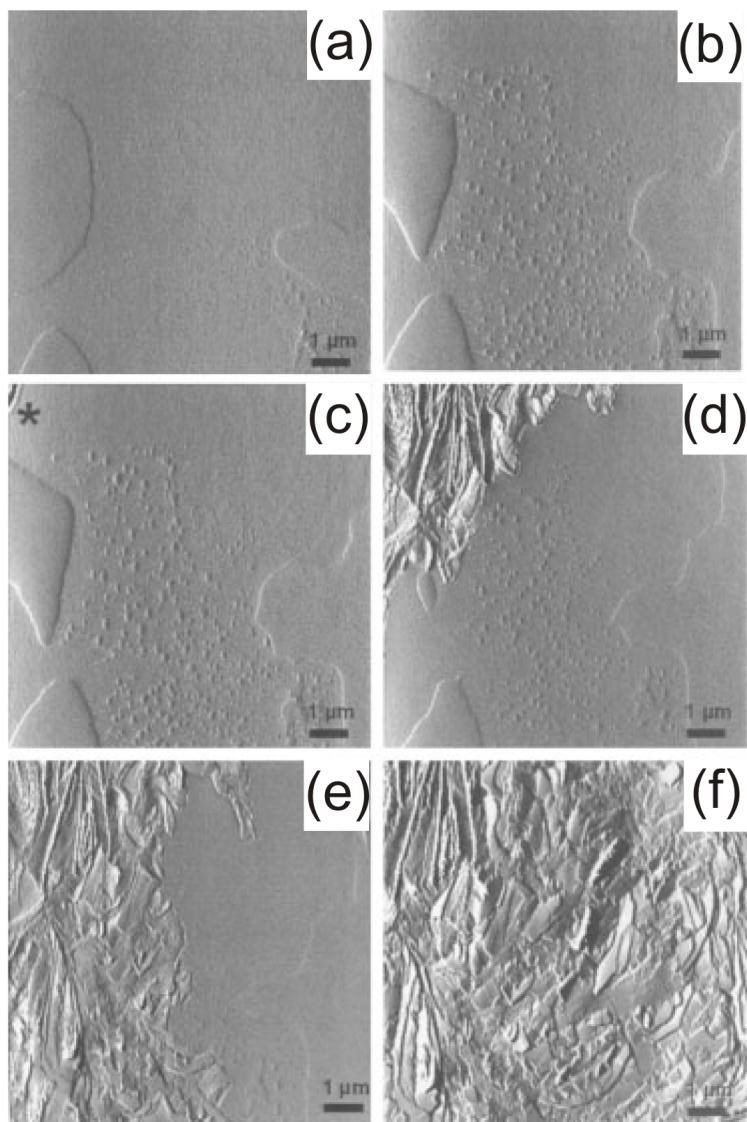


Figure 2.9: Intermittent contact mode amplitude images showing the surface reconstruction of a spray-dried lactose particle after exposure to 58% RH for: (a) 60 min, (b) 120 min, (c) 128.5 min. Sequential down-scan images are shown in (d-f). Adapted from reference [59].

Price *et al.* monitored the crystallisation of amorphous lactose prepared by spray drying in conditions of increasing humidity by AFM [59]. Their data suggested secondary nucleation and growth at 58 and 75% relative humidity (RH), and primary nucleation of α -lactose monohydrate at an elevated 94% RH (Figure 2.9). Chen *et al.* monitored the transition of anhydrous theophylline to its monohydrate form upon increasing humidity by *in situ* AFM (Figure 2.10) [60]. These findings provided insight into the hydration mechanism, indicating that the process was mediated by the formation of a surface solution generated as a result of water adsorption.

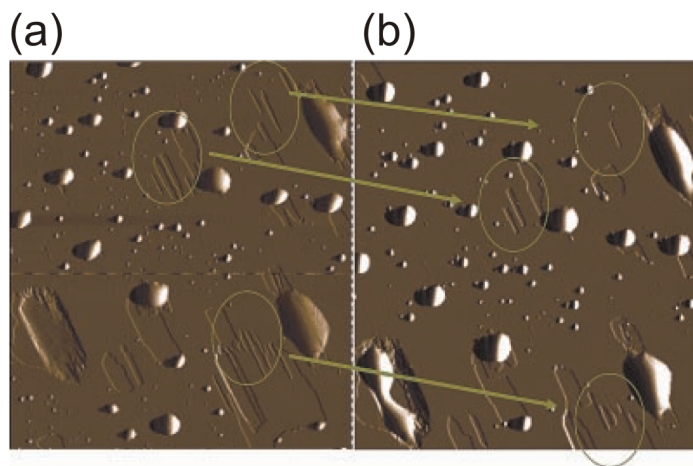


Figure 2.10: Intermittent contact mode amplitude images of an anhydrous theophylline crystal after exposure to 65% RH for: (a) 9 min, and (b) 108 min. Adapted from reference [60]. The imaging area is $10 \times 10 \mu\text{m}^2$.

Noteworthy, the study of crystal-growth by AFM has also been successfully extended to protein-crystallisation studies. More specifically, AFM was used to study the crystal-growth kinetics [61] and mechanisms [62], as well as in studies focusing on the effects of crystal growth and protein shape [63]. In addition, AFM imaging has been extensively used in studying the mechanisms of photochemical and other solid-state reactions. Several comprehensive reviews on this topic have been published in recent years [64–66], and photochemical aspects of solid-state reactions will be further explored in Chapter 7.

Epitaxial crystal growth

AFM goniometry, a method that can determine the growth modes and orientation of topographic features (*e.g.* ledges, terraces *etc.*) [68], was used to study the selective nucleation of 5-methyl-2-[(2-nitrophenyl)amino]-3-thiophene-carbonitrile (a decamorph commonly called ROY [67])(Figure 2.11) polymorphs by epitaxy on organic crystals [69]. The authors demonstrated that polymorph selectivity is very sensitive to surface features of the substrates. Specifically, crystals of yellow-needle polymorph were found to grow selectively on the (101) plane of pimelic acid as a result of epitaxy. Both AFM goniometry and computational simulations, namely geometric real-space analysis of crystal epitaxy, allowed the determination of the (001) crystal face of ROY contacting the (101) surface of pimelic acid with a crystal orientation $[100]_{YN} \parallel [010]_{PA}$ and $[010]_{YN} \parallel [101]_{PA}$. On the other hand, crystals of succinic acid were found to be less selective by facilitating the crystallisation of seven polymorphs. The low selectivity of the (010) face of succinic acid was attributed to its poor epitaxial

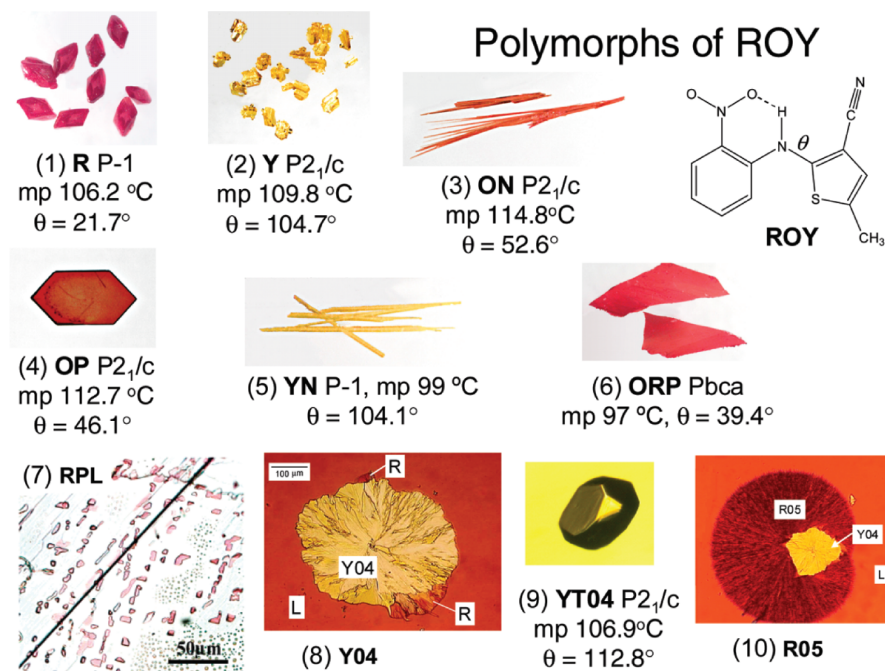


Figure 2.11: Polymorphs of ROY. Numbers 1 to 10 indicate the order of discovery. All the abbreviations correspond to different colours of the polymorphs. For example, ON, OP, and RPL represent orange needles, orange plates and red plates, respectively. Adapted from reference [67].

match with all the studied polymorphs, as determined by geometric real-space analyses.

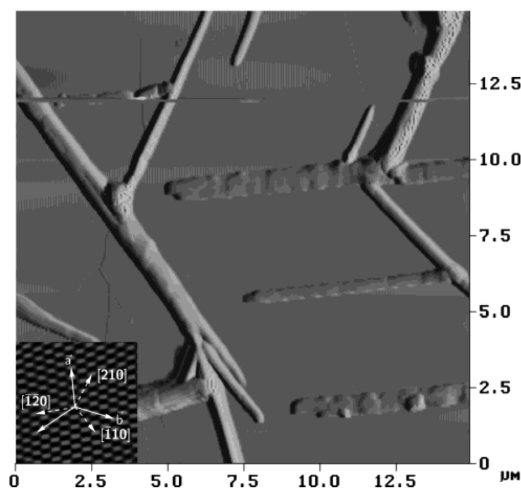


Figure 2.12: Determination of orientations of $C_{32}H_{66}$ crystals on substrate surfaces via AFM. The inset depicts an atomic-resolution image of highly oriented pyrolytic-graphite in the same area after fast Fourier transform filtering, with white arrows indicating different directions relative to the crystal orientation. Adapted from reference [70].

Another recent example of AFM application in heteroepitaxial studies illustrates the 3-D crystal growth of n-alkane crystals on non-polar highly oriented pyrolytic graphite surfaces [70]. AFM was employed to resolve structure re-

relationships between the substrate and the n-alkane crystal contact planes. It was found that the dotriacontane ($C_{32}H_{66}$) and tritriacontane ($C_{33}H_{68}$) grow in two orientations, being parallel to $\langle 100 \rangle$ and $\langle 210 \rangle$ on the highly oriented pyrolytic-graphite surface (Figure 2.12). Both n-alkane crystals were shown to contact the substrate with their (010) planes. In addition, it was determined that dotriacontane crystals grow via a growth mechanism [71] where crystal nucleation occurs on monolayers of dotriacontane molecules resulting in the growth of its thermodynamically less stable orthorhombic form. The formation of the less stable polymorph was attributed to the templating effect of the dotriacontane monolayers that formed prior to crystal nucleation. The templating effect was found to arise from the fact that dotriacontane molecules adopt the same arrangement on the monolayer as in the orthorhombic crystals.

Crystal growth kinetics

In situ imaging was used to study the kinetics of the monotropic polymorph transitions of caffeine form I to form II [72], a transition that readily occurs during tablet compaction and mechanical treatment [24]. AFM micrographs revealed that the phase transition initiates at the crystal surface, thus, allowing the use of a penetration kinetic model [73] to determine the phase transition activation energy (*i.e.* 73.8 kJmol⁻¹). Jones *et al.* further quantified the surface roughness and used such measurements to study the dehydration kinetics of trehalose dihydrate by *in situ* AFM at a controlled humidity level [74]. Notably, AFM allowed the determination of the dehydration kinetics of the bulk and the outer-layer of the crystal: while the outer layer undergoes dehydration following a zero-order-phase-boundary kinetic model, the bulk dehydrates through either an Avrami-Erofeev model or a cylindrically-symmetrical-phase-boundary model [75]. These findings show that kinetic AFM studies may lead to a deeper understanding of the reactivity and, thus, stability of molecular crystals.

Crystal growth inhibition

AFM is commonly used in studies regarding crystal growth inhibition. Numerous examples describing the stabilisation of amorphous materials [77, 78] and solid dispersions [79] by growth inhibition have been reported. In addition, crystal morphology control has been achieved by inhibiting the growth of specific crystal faces using additives [80, 81]. It was recently proposed that molecular additives could be used to prevent nephrolithiasis (*i.e.* kidney-stone disease) – a medical condition with steeply increasing prevalence worldwide.

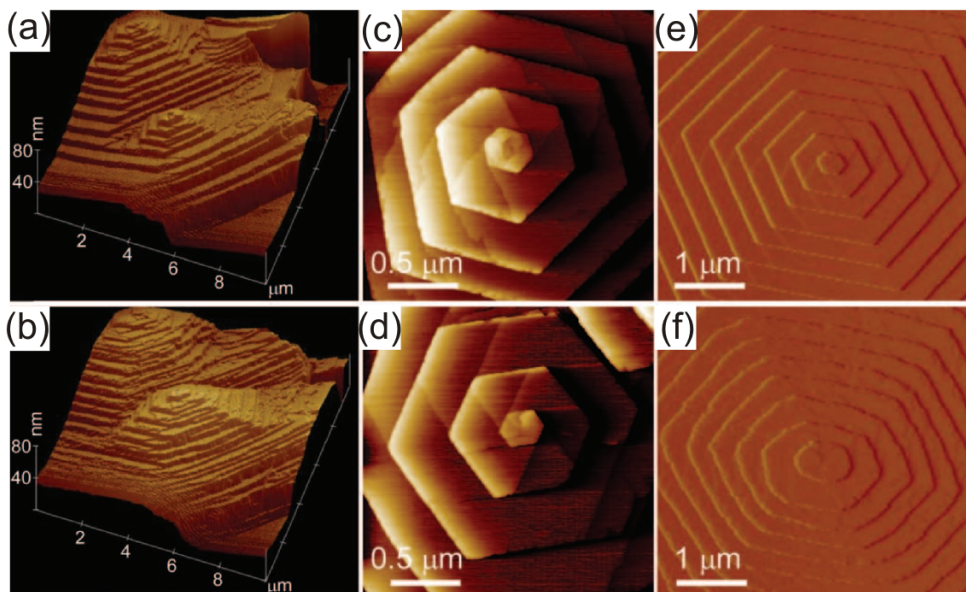


Figure 2.13: Real-time *in situ* AFM height images of a L-cystine crystal surface recorded 12 min apart (a, b). Single screw dislocations of L-cystine and D-cystine crystals during growth (c and d, respectively). AFM image of a hexagonal hillock on the (001) face of L-cystine (e) before and after the addition of L-cystine dimethylester, showing step pinning and roughening of $\{100\}$ steps (f). Adapted from reference [76].

Rimer *et al.* recently reported a real-time *in situ* AFM study and found that L-cystine dimethylester and L-cystine methylester considerably reduce the growth rates of L-cystine based kidney stones [76]. The addition of the L-cystine dimethylester resulted in the rounding of the hillock corners and the roughening of the highly linear and six-symmetry equivalent $\{100\}$ steps on L-cystine crystals. These topological changes were attributed to the dimethyl esters being adsorbed onto the $\{100\}$ surfaces through $S(\text{cysteine})\cdots S(\text{cysteine})$, $NH(\text{cysteine})\cdots O=C(\text{ester})$ and $O^-(\text{COO}_{\text{cystine}}^-)\cdots H_3N^+(\text{ester})$ hydrogen bonds, thus, simulating crystal growth through L-cystine molecules (Figure 2.13). More importantly, the attached dimethylesters would further prevent attachment of L-cystine molecules from solution due to steric hindrances caused by the ester methyl group, which ultimately results in crystal growth inhibition. This study clearly illustrates the use and importance of AFM in disease prevention and the development of therapeutic agents.

Identifying phase transitions and polymorphism

It is crucial to understand surface changes of organic crystals during chemical reactions or in response to environmental alterations. One example of *ex situ* imaging is the study of (caffeine)·(oxalic) acid and (caffeine)·(malonic) acid cocrystals, which were both reported by Trask *et al.* to be stable in 98% RH

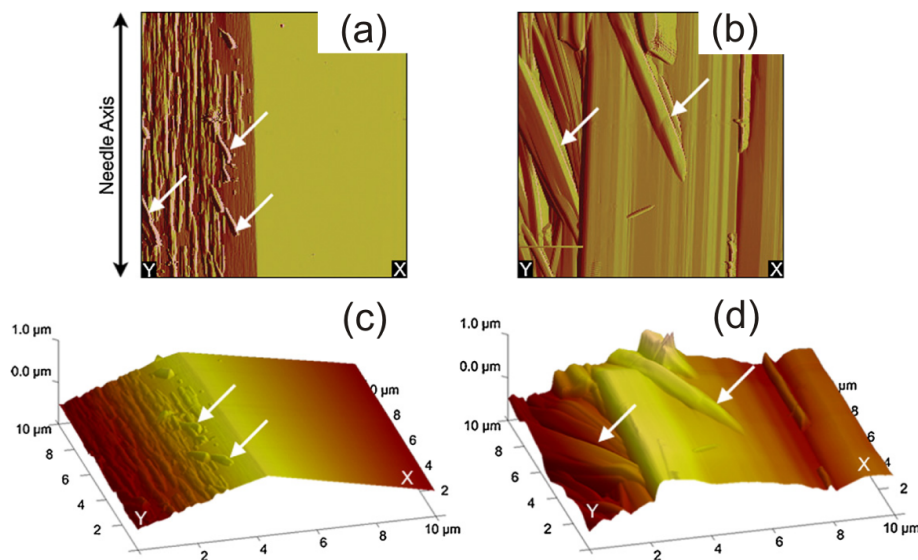


Figure 2.14: AFM images of a (caffeine)·(oxalic acid) cocrystal stored at 75% RH. The images were obtained from an area that covers (0 1 1) and (0 0 1) faces (labeled x and y, respectively). The deflection images were recorded: (a) after the sample was prepared for analysis and (b) after seven days of exposure to 75% RH. The corresponding 3D height representations are shown on figures (c) and (d). Adapted from reference [82].

and 75% RH by PXRD studies [83]. Cassidy *et al.* monitored the surface response of these cocrystals by *ex situ* AFM before and after exposure to these humidities (Figure 2.14) [82]. The authors observed that caffeine and oxalic acid exhibits a high degree of mobility on cocrystal surfaces that facilitates surface recrystallisation events. This study demonstrated that the information regarding surface changes which are not apparent from bulk measurements (such as powder X-ray diffraction) can be detected by AFM, and may be important for predicting the stability of the API-excipient interface.

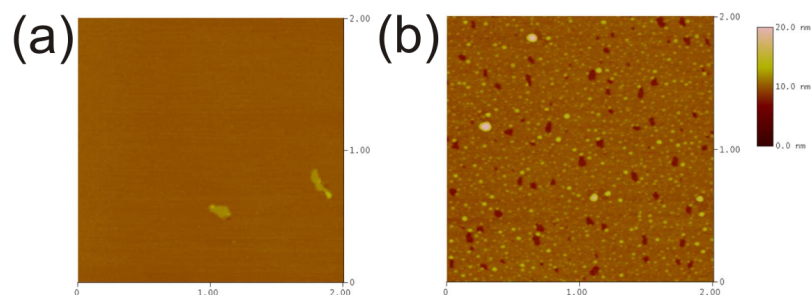


Figure 2.15: AFM height images of the (001) plane of an ingestive drug molecule: (a) before, and (b) after storage at 20°C and 40% RH for 24 h. The colour scale used to represent the topography data of both images is shown on the right. Adapted from reference [84].

Surface changes upon exposure to variable humidity were observed by AFM imaging on many other materials. Such findings add clarity to the understanding of surface reaction mechanisms. For example, Kiang *et al.* reported surface

changes of an investigational drug molecule after exposure to 40% RH environment by *ex situ* AFM (Figure 2.15) [84]. AFM revealed that the (001) plane exhibits a flat topography which upon exposure to moisture becomes significantly rougher. Specifically, the measured root-mean-square crystal-surface roughness increased from 0.173 nm to 0.749 nm. The observed change in roughness was attributed to the formation of adsorbed water layers that enabled drug dissolution and recrystallisation.

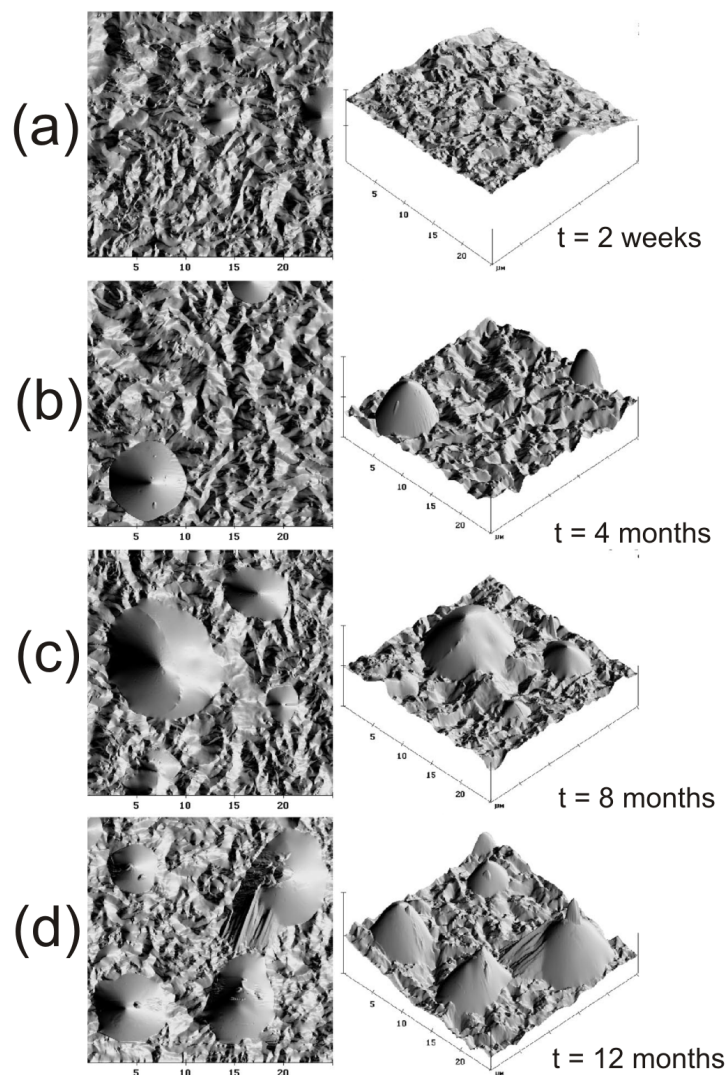


Figure 2.16: 2-D and 3-D height images of a chocolate sample obtained at various storage times. Adapted from reference [85].

AFM is also useful in quality control in the food industry, particularly in the development of confection formulations with improved textural and visual features. Recently, Sonwai *et al.* described the use of AFM phase imaging to determine how the fat-phase composition of milk affects the surface-microstructure and fat-phase-polymorphism of industrial milk chocolates (Figure 2.16) [85].

Phase imaging in intermittent contact mode is particularly useful in detecting different surface materials when the height signal does not provide useful information, as the phase signal reflects differences in material properties. Extensive AFM imaging, along with colorimetry and PXRD, revealed that the longest chocolate shelf-life can be achieved by using mixtures of milk fats and cocoa-butter equivalents where the amount of cocoa-butter equivalents do not exceed 5%. Samples with less than 5% cocoa-butter equivalents were shown to display the least polymorph transitions of fat phases and the slowest cone formation on the chocolate surface.

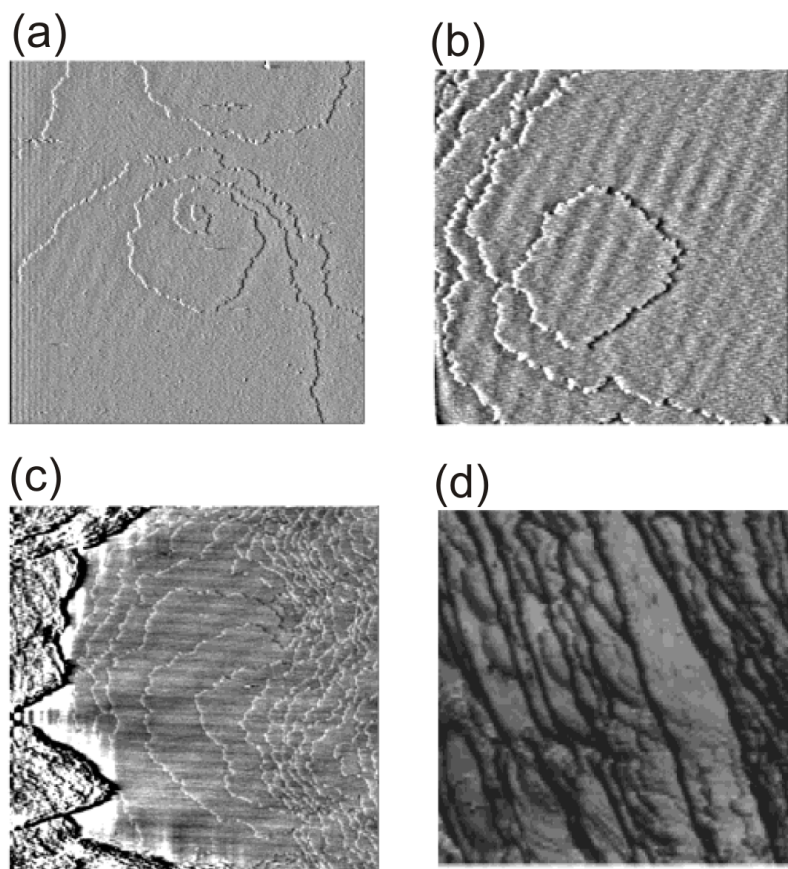


Figure 2.17: AFM images of the $\{110\}$ face of paracetamol crystals grown by: (a) dislocation mechanism, (b) 2-D nucleation, (c) step bunching at low supersaturation and (d) interface instabilities manifested at high supersaturation. Adapted from reference [86].

In situ AFM imaging was involved in the development of new methods for reducing morphological instabilities of pharmaceutical crystal surfaces [86]. Step bunching is a phenomenon occurring on crystal surfaces that entails the merging of small crystal-growth steps of heights corresponding to few unit cell lengths into large steps with heights of tens or even hundreds of unit cell lengths [87]. The morphological instability is the most prominent cause of impurity (*e.g.* solvents, melts) trapping in crystal growth. Oscillatory flowmixing

crystallizers have been used to reduce the interfacial instabilities of paracetamol. Two types of mixers, oscillatory-baffled batch crystallizer (OBBC) and impeller-driven batch crystallizer (IDBC), have been used for crystal growth, with AFM imaging monitoring the growth of $\{110\}$ faces in paracetamol crystals (Figure 2.17). This study showed that crystals obtained from OBBCs exhibit smaller volume-weighted median diameters, smoother surfaces with reduced microstrain levels and less pronounced step bunching than those obtained in IDBCs.

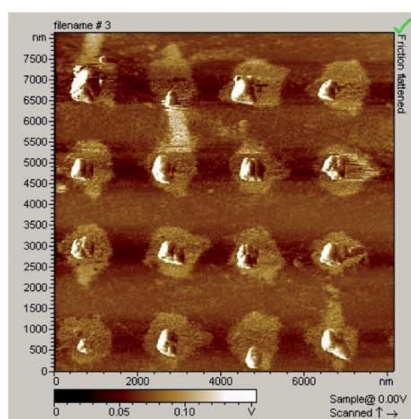


Figure 2.18: AFM images of glycine crystals grown on a patterned self-assembled monolayer substrate. Adapted from reference [88].

Recently, AFM significantly aided the study of polymorphism in glycine nano-crystals, grown on self-assembled monolayers (Figure 2.18) [88, 89]. Photolithography was used to fabricate bifunctional patterned surfaces containing hydrophilic and hydrophobic areas. The circular hydrophilic areas (diameter of 500 nm) composed of 3-aminopropyl-triethoxysilane, while the remainder of the substrate contained hydrophobic octadecyltrichlorosilane moieties. The hydrophilic surfaces of the substrate then acted as deposition sites for solution droplets of less than 500 nm in diameter, from which nano-sized glycine crystals were grown. The supersaturation of the droplet was controlled by slow cooling or by solvent evaporation, and was an important factor in the polymorphic outcome. Particularly, cooling rates ranging from $0.05 - 0.001 \text{ } ^\circ\text{Cmin}^{-1}$ resulted in the formation of the β -form, while cooling rates below $0.001 \text{ } ^\circ\text{Cmin}^{-1}$ yielded both α - and β -glycine, and slow solvent evaporation over 100 hours resulted in the realization of the α -, β - and γ -glycine. The results of this study demonstrated the potential of AFM in the development of technologically important devices (*e.g.* field-effect transistors) [90], as well as in the formulation of poorly soluble pharmaceutical materials [89]. In a related study, Ito *et al.* studied the solution mediated phase transitions of α -glycine to γ -glycine [91].

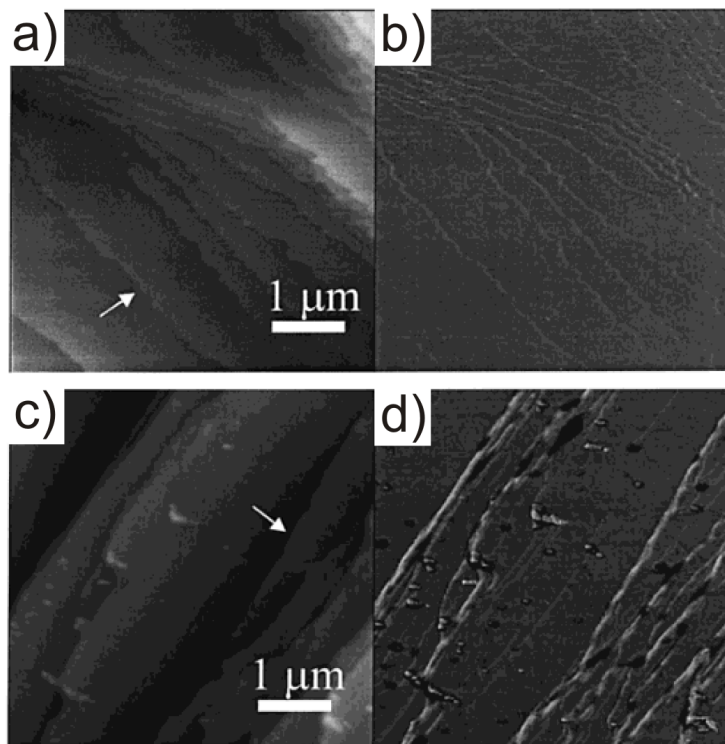


Figure 2.19: AFM height and phase images of cimetidine polymorph A (a, b) and polymorph B (c, d). Adapted from reference [92].

Danesh *et al.* [92] utilised AFM phase imaging to determine that the two different polymorphs of cimetidine (Figure 2.19) exhibit different phase angles, *i.e.* the phase difference between the oscillation of the tip and the driving oscillation at the base of the cantilever. Therefore, phase imaging can be used to map out different regions of materials on a surface [74] and in turn detect any heterogeneity in the mixing of materials [93].

Dissolution studies

A detailed mechanistic understanding of the dissolution of materials is of tremendous interest in pharmaceutical research, as it is related to the API bioavailability, which contributes to the performance of drugs in the body. In studying the dissolution and etching of materials, it is obvious that surface molecules are always the most exposed to the liquid medium, therefore being the first to be dissolved. Hence, studies that incorporate AFM imaging have been particularly invaluable in elucidating the dissolution process. Wen *et al.* [94] used *ex situ* AFM to observe changes on glycine crystal surfaces after etching with various solvents (Figure 2.20). Most of the etching patterns reflected the directionality and strength of attachment energies [95], *i.e.* the energy released when one crystal-growth slice of the thickness d_{hkl} is attached to the (hkl) crystal face.

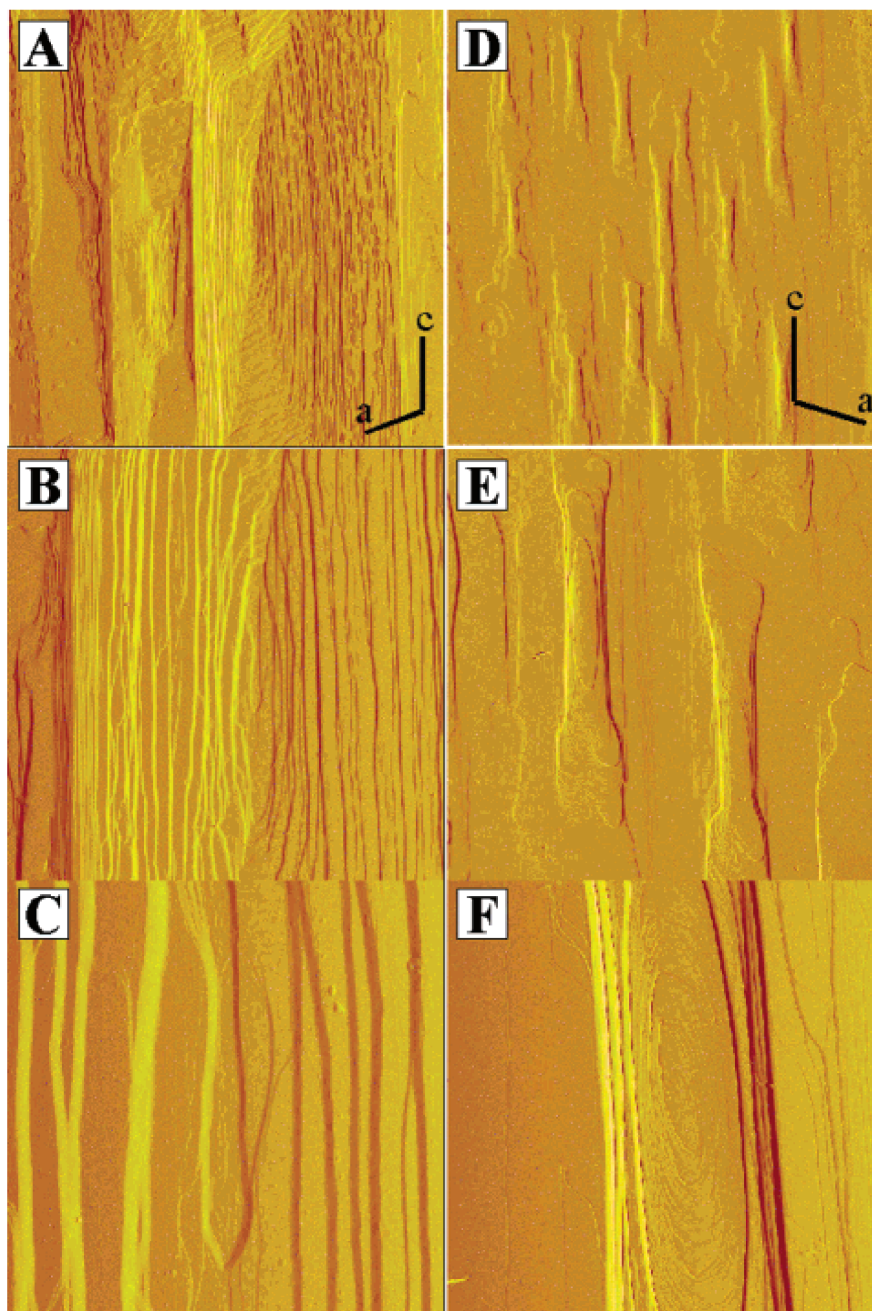


Figure 2.20: AFM images of (010) face of α -glycine etched by water (A-C) and acetone (D-F). The image sizes were $60 \times 60 \mu\text{m}^2$ (A, D), $20 \times 20 \mu\text{m}^2$ (B, E), $5 \times 5 \mu\text{m}^2$ (C, F). The images were zoomed in gradually from (A) to (C) and (D) to (F). Directions of the a-axis and c-axis are shown in (A) and (D). Adapted from reference [94].

It was therefore suggested that the crystal structure (and the related attachment energies) controls the etching process of crystal surfaces. The study also described the role of solvents in assessing the relative significance of attachment energies in various directions.

The dissolution of aspirin (ASA) has also been studied by both *in situ* [96] and *ex situ* [94] AFM imaging. These will be further illustrated in Chapter

3, which composes of a literature review on studies related to the solid state hydrolysis of ASA crystals. Meanwhile, dissolution studies by AFM have also been performed on other materials such as pathogenic biominerals [97] and kidney stones [98, 99].

2.2.2 Force-distance measurements: adhesion forces and surface energies

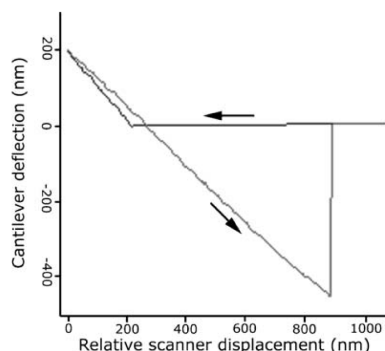


Figure 2.21: Representative force distance plot for a budesonide particle on an AFM probe ramped onto a model mica surface. Adapted from reference [100].

Force-distance measurements are very useful for quantitative surface characterisation of organic crystals. For example, the surface energy of micronized budesonide particles was calculated by Davies *et al.* using this technique (Figure 2.21) [100]. The surface energy by this method was compared to that measured by inverse gas chromatography. While the authors concluded that these two values were in approximate agreement, the values obtained from AFM measurements had a wider range owing to: (1) the assessment of localised areas, rather than the entire surface area, and (2) the presence of particulates on the studied surface. It was concluded that AFM was particularly useful in assessing the topography of drug-particle and carrier-material complexes and how particles interact with one another. Surface energies obtained by force distance measurements have also been used to identify various materials [101, 102].

The use of functionalised colloid probes in force distance measurements of pharmaceutical crystalline materials has also been explored [104–106]. Such probes can be used to assess the interactions between drug components and other materials. For example, in investigating the problem of drug particles sticking to tablet compressors during manufacturing, Wang *et al.* simulated tablet compressor walls by using silicon nitride tips coated with a layer of iron that was 20 nm thick [103]. The coated tips were then used in force distance measurements on different profen drug molecule surfaces, whereby the work of

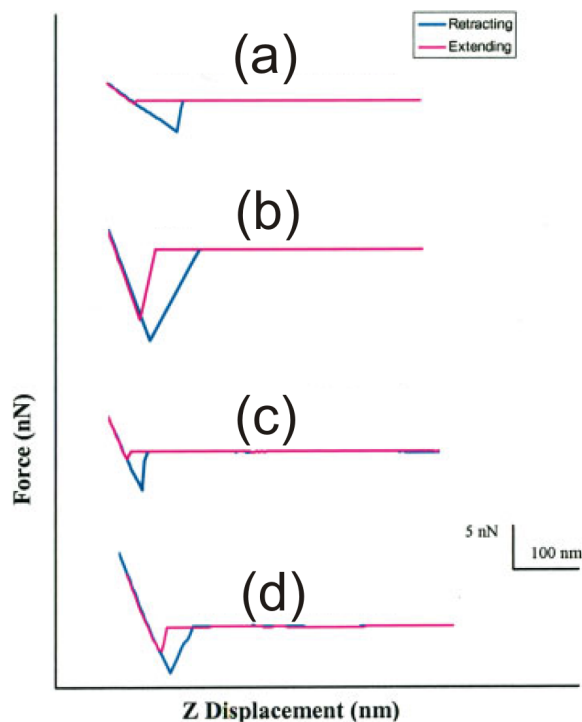


Figure 2.22: Force distance measurement plots obtained from: (a) an iron-coated tip and a flat ibuprofen surface immersed in ibuprofen-saturated water, (b) an iron-coated tip and a flat ketoprofen surface immersed in ketoprofen-saturated water, (c) an iron-coated tip and a flat flurbiprofen surface immersed in flurbiprofen-saturated water and (d) an iron-coated tip and a flat iron-coated surface immersed in water. Adapted from reference [103].

adhesion of each profen surface to the tip could be determined (Figure 2.22).

Studies of cohesion-adhesion balance between dry powder inhaler (DPI) components [107, 108], and drug-canister interactions [109] provide other examples of interesting interactions that can be addressed by this technique, even at early stages of drug formulation.

2.2.3 Nanoindentation techniques and mechanical properties of molecular crystals

Nanoindentation is a special force distance technique which uses a hard material (*e.g.* diamond) for the tip and a substantial loading force. As a result, the tip can penetrate soft samples and leave indentation marks on the surface. The local hardness and Young's modulus of the sample can be estimated from the extent of the nanoindentation [111, 112]. Perkins *et al.* studied by AFM the surface response of carbamazepine polymorphs before and after micronisation using standard silicon probes, noting an increase in surface energy after micronisation for all three polymorphs form I, II and III (Figure 2.23) [110]. The hardness measured based on the force distance plots of nanoindentation

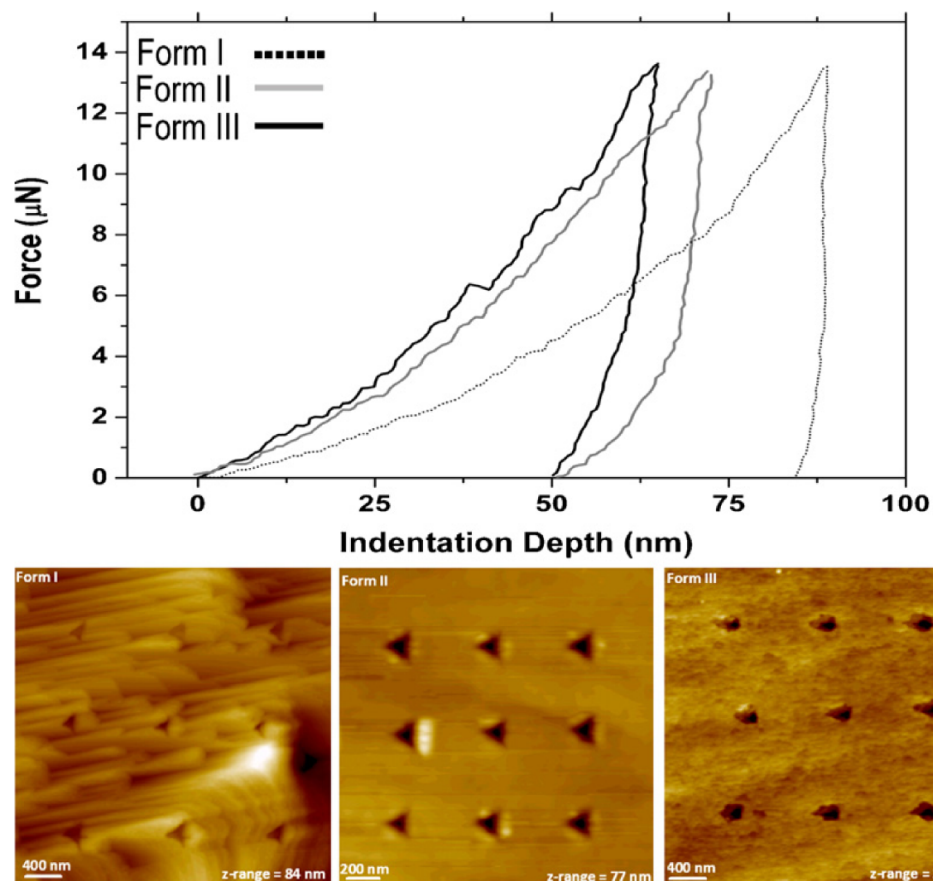


Figure 2.23: Selected force distance plots for the three forms of carbamazepine, together with respective AFM height images of these forms. The force distance plots show that each form has a different hardness based on the indentation depth using the same loading force. Adapted from reference [110].

indicated different indentation depth for each polymorph while using the same loading force, suggesting different hardness for each form. The authors also reported a correlation between the ratio of indentation hardness to Young's modulus, and the increase in surface energy upon micronisation. This study demonstrated that AFM can be particularly beneficial in predicting outcomes of manufacturing procedures such as tableting and micronisation by using small amounts of sample.

Masterson *et al.* [113] employed nanoindentation to screen for mechanical properties of various pharmaceutical compounds, ranking the compounds in terms of hardness (Figure 2.24). Ascorbic acid was found to be the hardest, followed by sucrose, lactose, and ibuprofen. Cao *et al.* [114] obtained the elastic modulus and hardness for similar pharmaceuticals from nanoindentation (Table 2.1), and related this to the compaction performance. It was found that materials with very low or high particle hardness most likely exhibit poor compaction performance, while materials with medium particle hardness exhibit

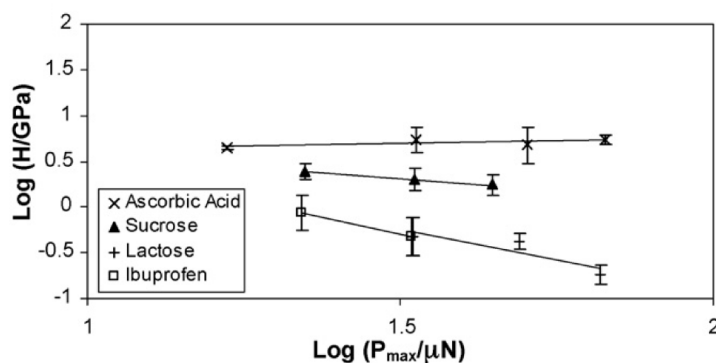


Figure 2.24: Plot of hardness [$\log(H)$] vs. maximum peak load on the cantilever [$\log(P_{max})$] for ascorbic acid, sucrose, lactose, and ibuprofen. Adapted from reference [113].

Materials	H(Hpa)	E_r	E (GPa)	H/ E_r
SAT	0.7	1.9	1.7	0.37
Ibuprofen, Lot A	0.6	2.1	1.9	0.29
Ibuprofen, Lot B	0.4	1.2	1.1	0.33
Ibuprofen, Lot C	0.22	0.9	0.8	0.24
UK-370106	0.4	1.1	1	0.36
Acetaminophen	1	1.9	1.7	0.53
Phenacetin	0.9	2.2	2	0.41
PHA-739521	1.1	2.4	2.2	0.46
Sucrose	2.3	4.1	3.7	0.56
MCC	1.4	2.9	2.6	0.48
Fluconazole	2	3.1	2.8	0.65
Ascorbic acid	5	5	4.6	1
Probenecid	4.9	4.3	3.9	1.14
Tartaric acid	4.7	4	3.7	1.18
SSG	4.6	4.8	4.4	0.96

Table 2.1: Mechanical properties of particles of pharmaceutical materials determined by AFM nanoindentation. Adapted from reference [114].

good compaction behaviour (Figure 2.25). However, it is also important to note that hardness is not the only factor that should be considered in tablet compaction.

Nanoindentation techniques were also employed to rationalize the bending of organic crystals [115]. Bending was shown to be a result of the crystal packing, rather than the crystal morphology. The authors further demonstrated that bending arises in crystals where strong and weak interactions occur in approximately perpendicular directions (Figure 2.26). AFM nanoindentation was employed in this case to demonstrate the crystal-packing anisotropy in 2-(methylthio)nicotinic acid crystals by the measuring the crystal hardness along three crystal directions.

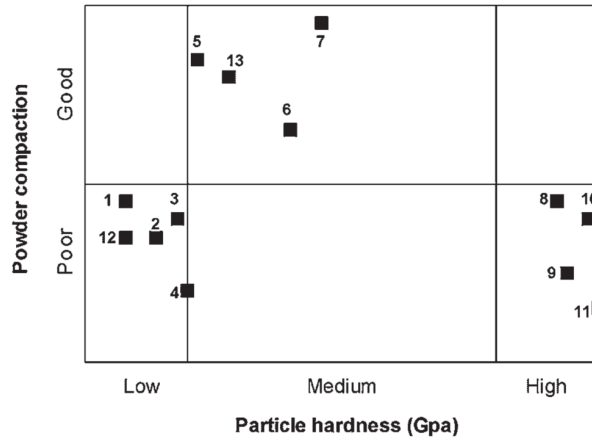


Figure 2.25: A correlation plot between particle hardness and powder compaction performance. Numbering scheme: 1. ibuprofen, 2. sodium acetate trihydrate, 3. phenacetin, 4. acetaminophen, 5. microcrystalline cellulose, 6. fluconazole, 7. sucrose, 8. sodium starch glycolate, 9. tartaric acid, 10. probenecid, 11. ascorbic acid. Adapted from reference [114].

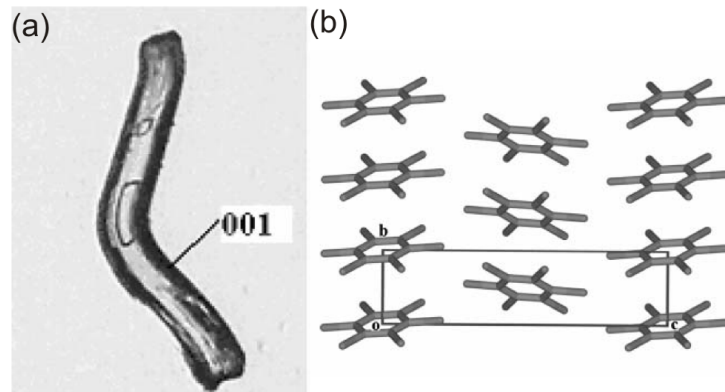


Figure 2.26: (a) A hexachlorobenzene crystal bent along the (001) face, and (b) the crystal packing of hexachlorobenzene. Adapted from reference [115].

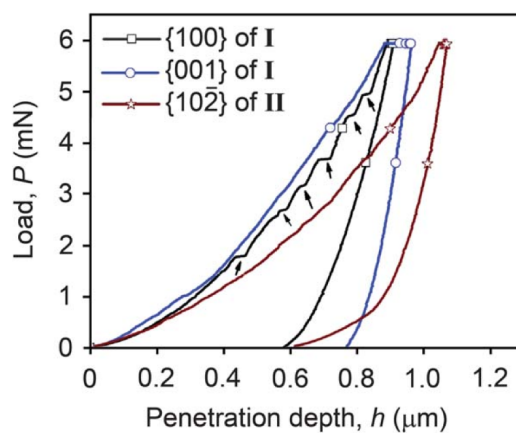


Figure 2.27: Representative load versus depth-of-penetration curves of saccharin obtained with indentation normal to the (100) and (011) planes. The arrows in the graph indicate possible discrete displacement bursts or pop-ins. Adapted from reference [116].

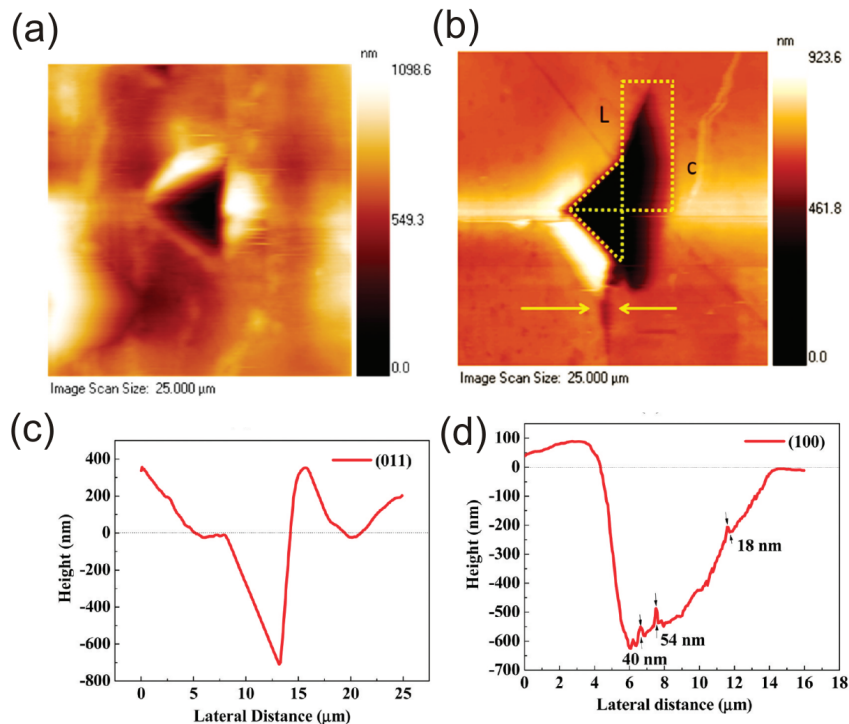


Figure 2.28: AFM height images of saccharin showing: (a) cracks along two corners of the indenter on the (100) face formed at a 6 mN peak load, (b) no radial cracks observed on the (011) face under equal load, (c) horizontal cross-section at the center of indentation shown in (a), (d) horizontal cross-section at the center of indentation shown in (b). Adapted from reference [116].

AFM nanoindentation technique was also used to determine the correlation between mechanical properties of organic crystals and their internal structures. Kiran *et al.* reported a nanoindentation study that aimed to assess the mechanical anisotropy of saccharin single crystals [116]. The authors studied plastic deformation on the (011) and (100) faces of saccharin crystals (Figure 2.27). The studied faces showed approximately 5% difference in Young's moduli which was attributed to the anisotropic interaction characteristics within the crystal.

Upon indentation, the load displacement curves obtained from (011) revealed that the crystal undergoes a homogeneous plastic deformation (Figure 2.28 (a) and (c)). This deformation was attributed to the presence of various possible slip systems parallel to the plane of indentation. On the other hand, (100) showed discrete displacement bursts that were 18 nm in magnitude and occurred in integer multiples of 18 nm (Figure 2.28 (b) and (d)).

In 2011, Karunatilaka *et al.* utilized AFM nanoindentation to characterise mechanical properties of photoactive cocrystals of both macro- and nano-dimensions that undergo a single-crystal-to-single-crystal reaction [117]. A cocrystal consisting of 5-cyanoresorcinol and trans-1,2-bis(4-pyridyl)-ethylene was found to undergo a [2+2] photodimerisation upon UV-irradiation accom-

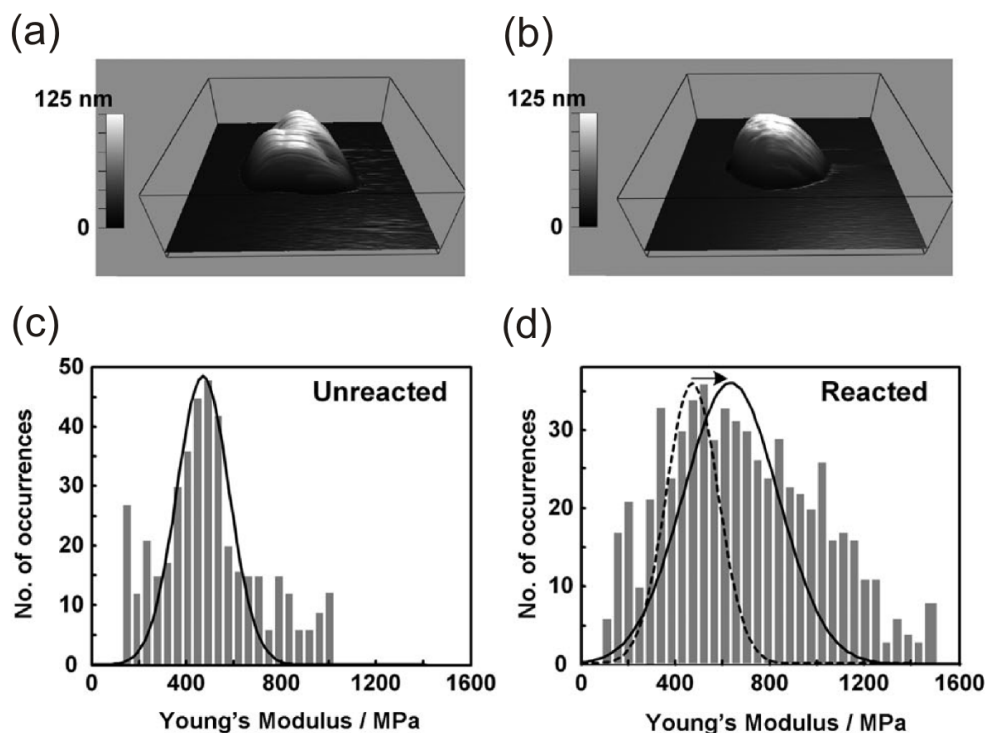


Figure 2.29: AFM height images of: (a) an unreacted, and (b) a reacted nano-cocrystal of similar height, and Young's moduli values of nano-cocrystals before (c) and after photoreaction (d). Adapted from reference [117].

panied by a change in Young's modulus, and a small change in crystal density (0.1%). While macro-dimensional crystals softened and exhibited a decrease in Young's modulus from 260 MPa to 150 Mpa (40% change), nano-dimensional crystals were found to harden around 40% showing an increase in Young's modulus from 460 MPa to 635 MPa (Figure 2.29). The opposite changes in stiffness of macro- and nano-dimensional crystals was attributed to the high surface-to-volume ratio of the nano-crystals, which allowed efficient stress and strain relaxation. AFM nano-indentation was performed on crystals isolated from a bulk sample before and after UV-irradiation, as well as *in situ* during the course of the photoreaction.

Jing *et al.* recently reported a novel nanoindentation based method for systematic studies of slip planes in molecular crystals [118]. The method required the use of a non-axisymmetric cube-corner indenter to generate inhomogeneous stress fields whereby various slip planes were activated by rotation of the sample. Succinic acid was used as a model compound, and the authors identified the (111) and (010) planes as major slip planes. Notably, other crystallographic planes were identified as slip planes that were not previously reported in the literature, and could not be predicted by attachment-energy calculations. The developed nanoindentation method, therefore, represents an important tool in

understanding milling abilities of pharmaceutically relevant materials.

Kaupp *et al.* recently used nanoindentation and nanoscratching to study molecular movements under various crystal faces of thiohydantoin [119]. The AFM tip was used to scratch the (110) face, breaking the hydrogen bonds mechanically thus enforcing the covalently saturated fragments to migrate along the unobstructed cleavage plane followed by the reinstatement of the hydrogen bonds. It was also proposed that hydrogen-bond dimers, trimers, or hexamers of thiohydantoin are the most likely migrating species (if not the isolated molecules). The authors proposed that related studies might open up new opportunities in nanotechnology and surface structuring. Based on the results obtained in a similar study, Kaupp *et al.* proposed that nanoscratching and the observation of induced anisotropic molecular movement in crystals can be used to predict whether a crystal is suitable for solid-state reactions (*e.g.* photochemical, thermal, *etc.*), given that the chemical structure of the molecules in the crystal allows such reaction [120].

2.2.4 Concluding remarks

The use of AFM has not been limited to the techniques described above. There has been a continuous exploration of new AFM techniques, including the use of thermal probes [121–125], conductive probes [43, 126–130], Kelvin probe force microscopy [131, 132] and combining confocal raman spectroscopy with AFM [133]. In conclusion to this chapter, AFM has been developed to become an important tool in various research fields. Bearing in mind that physicochemical properties of crystals strongly depend on their surface morphologies and properties, as well as the indispensability of AFM in surface studies, it is clear that AFM needs to become a standard tool in studying organic crystals.

Chapter 3

A literature review on the hydrolysis of aspirin (ASA)

For more than 2000 years, willow tree barks and leaves have been used to relieve fevers and pains. The ingredient found in willow trees that gives rise to its medical effect is salicin, which transforms to salicylic acid (SA) in the body as the main metabolite in the body. Aspirin (ASA), closely related to SA, was first synthesized by Charles Frederic Gerhardt in 1853 [134]. It was only until 1897 when Bayer further developed and globally commercialised ASA as a new drug. Nowadays, it is one of the most widely used medications in the world, not only for fever and pain relief, but also for long term prevention of heart attacks and strokes.

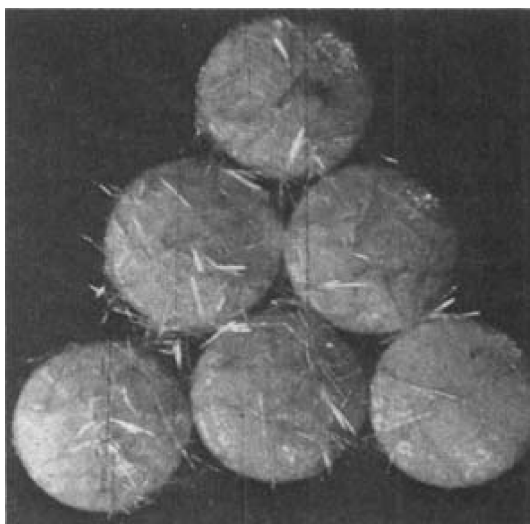


Figure 3.1: ASA tablets aged in 80% RH and 50°C for 98 days, containing needle-shaped crystals of SA on the surface. Adapted from reference [135].

ASA, salicin, and SA are classified as nonsteroidal anti-inflammatory drugs. ASA is normally the preferred form for manufacturing oral dosages, as it is less

irritating to the lining of the mouth and stomach than SA and salicin. As it is important to the pharmaceutical industry to study and understand the stability of any drug products, the hydrolysis of ASA to form SA has always been a research topic of interest (Figure 3.1). However, while the solution [136–140] and solid state [135, 141–146] hydrolysis of ASA form I have both been studied extensively, the latter reaction in particular is still not well understood.

There are two polymorphs of ASA crystals, where form II was first reported in 2005 [147]. Although there was some ambiguity concerning the crystallinity of the new form and whether form II domains were a result of a stacking disorder [148, 149] of the original form I structure [150], Bond *et al.* later confirmed its existence by characterising single crystals of “pure” ASA form II [151]. There were also reports on new cocrystals [5, 152] and salts [153] of ASA which were either less prone to hydrolysis, or had other improved physicochemical properties. While the continuous search for improved ASA derivatives is beneficial, the importance of further understanding ASA degradation via hydrolysis must not be overlooked. In this chapter, an overview of studies involving the solid-state hydrolysis of ASA from the literature will be presented. The validity and limitations of previous bulk hydrolysis studies will be assessed, and recent studies involving ASA crystal surfaces will be reviewed, highlighting the importance of considering the ASA crystal surfaces in future hydrolysis studies.

3.1 Bulk studies on the hydrolysis of ASA

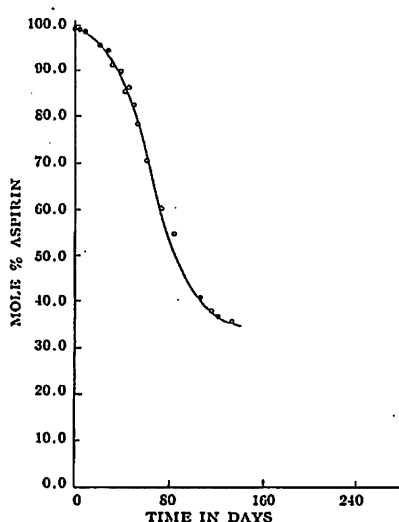


Figure 3.2: Typical ASA decomposition curve in the presence of humidity at 60°. Adapted from reference [141].

Leeson and Mattocks were one of the first to report kinetic studies on the

hydrolysis reaction of ASA in the solid-state [141]. The degree of hydrolysis was measured by detecting the amount of SA in the aged compound. A spectrophotometric technique was employed to achieve this, which required the dissolution of the aged solids prior to detection. The authors suggested that in the absence of water vapour, the reaction would not occur. In the presence of humidity, a sigmoid curve was observed when plotting the amount of SA formed over time, indicating an initial acceleration in the rate of hydrolysis (Figure 3.2). The mechanism proposed for this solid-state reaction was water initially being adsorbed onto the sample particles, followed by the diffusion of ASA molecules into solution, then acid hydrolysis in the resultant liquid phase on the particle surface.

Gore *et al.* later reported that the measurement of SA as an indicator of the extent of hydrolysis was not accurate, as a significant amount of SA would have sublimed under the studied conditions as well as during the dissolution of the aged solids in preparation for spectrophotometry [135]. This most likely led to the underestimation of the hydrolysis kinetics. To circumvent these issues, the authors suggested an improved UV spectrophotometric method which allowed the determination of the residual ASA content directly.

This system was further studied by Hasegawa *et al.*, whom discarded the surface solution mechanism that was initially proposed by Leeson and Mattocks [145]. Though they observed a sigmoid curve in ASA degradation similar to the previous authors, further tests showed that the presence of acidic decomposition products SA and acetic acid did not cause the initial change in hydrolysis rate. Moreover, the degradation of ASA was monitored by optical microscopy, and the reaction occurred only at partial areas of the crystals before spreading all over the surface. A surface nucleated mechanism was suggested to explain the hydrolysis instead. While this mechanism was supported by Ball [144], it has been challenged by different mechanisms proposed by others [142, 143, 146]. Furthermore, there have also been numerous studies on the effect of excipients on the hydrolysis of ASA crystals [154–165].

3.2 Limitations of bulk studies

Despite numerous studies on the solid-state hydrolysis of ASA in the past, the nature of the reaction remains unclear. Before further investigation, it is first worth addressing the limitations of the bulk studies that were reviewed in the previous section:

- The bulk studies relied on spectrophotometry or HPLC [166] for the de-

tection of ASA and SA, which is an indirect method that required the dissolution of the solid samples prior to detection.

- The temperature was raised above room temperature during the degradation process in order to accelerate the rate of hydrolysis. This was required to ensure sufficient chemical change in bulk content for detection over a reasonable timescale. Although this is a common practice for pharmaceutical research, the sublimation of SA at such temperatures can lead to inaccurate kinetic measurements [135].
- Most of the studies did not take into account the effect of the particle size and surface area on sample degradation. Only one report considered these factors, but the decomposition curves did not fit the models that incorporated particle size effect [145]. The results were inconclusive, and the authors suggested that although the decomposition could not be fully described by any simple reaction model, particle size and surface area does seem to affect the decomposition.

Amongst these limitations, the last one is the most significant factor. Based on the observation that hydrolysis occurs in the presence of water, it is more sensible to consider the hydrolysis as a surface reaction, as only the outermost molecular layers of the particles are in direct contact with moisture. Therefore, studies based on bulk characterisation techniques are not accurate, as they only detect the combined reactivity of the bulk and surface of a crystal. In order to better understand the degradation of ASA, only the surface of crystals or particles should be considered.

3.3 The anisotropy of crystal faces

One further complication in studying particle surfaces is the anisotropy of different ASA crystal faces. This was first evident in a study by Tawashi [167], who observed samples recrystallised from either ethanol or hexane had different dissolution rates. Initially it was proposed that the difference in rates was due to different polymorphs produced, one from each solvent. This was found to be incorrect, although ASA form II was discovered several decades later [147–149, 151]. In fact, it was the difference in morphology of the crystals used for Tawashi’s study that gave rise to different dissolution rates. As each face has its unique properties, the change in the exposed surface area of each face can significantly affect how the sample behaves.

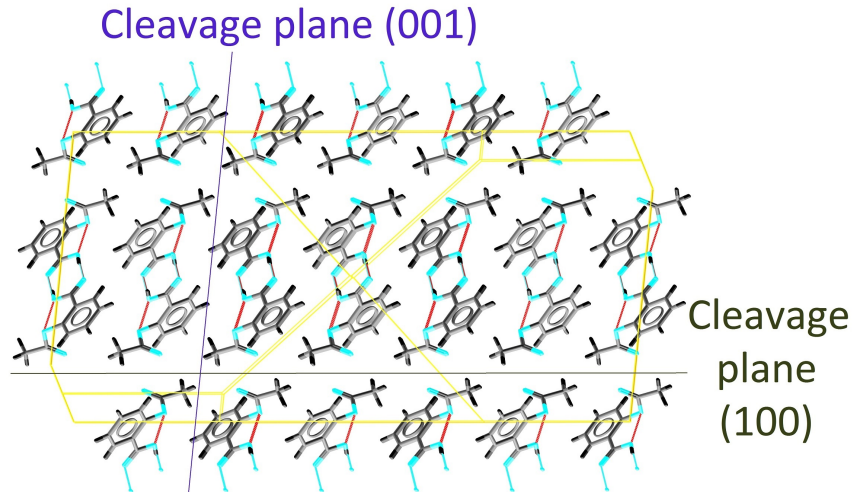


Figure 3.3: Crystal structure (CSD code ACSALA01 [168]) and predicted BFDH growth morphology of ASA, showing planes (100) and (001) which do not interfere with the hydrogen bonding pattern between ASA dimers.

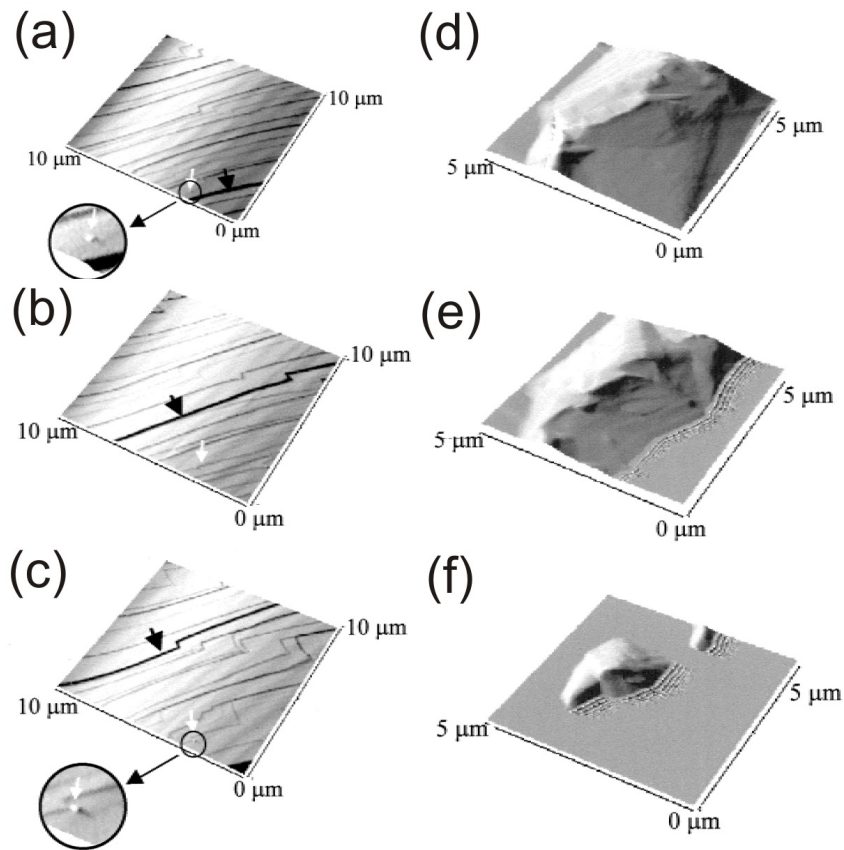


Figure 3.4: $10 \times 10 \mu\text{m}^2$ AFM images of ASA (001) surface under dissolution at (a) $t = 0$ s, (b) $t = 132$ s, (c) $t = 197$ s; $5 \times 5 \mu\text{m}^2$ images of ASA (100) surface under dissolution at (a) $t = 0$ s, (b) $t = 267$ s, (c) $t = 444$ s. Images are artificially illuminated from the left. Adapted from reference [96].

Anisotropy of crystals arises from the nature of crystalline materials. In a perfect crystal, molecules are locked in position and orientation. The exposed

surface of each face reveals different functional groups. The two main cleavage planes (100) and (001) of ASA is a good example. As these planes do not interfere with the hydrogen bonding pattern, the crystals are easily cleaved along them (Figure 3.3). There are two possible truncations on the (100) face, one intersecting the hydrogen bonding pattern exposing the carboxylic acid groups, another exposing the ester terminal groups of ASA molecules. The latter truncation is more likely to occur, as this is more energetically favourable than breaking the stronger hydrogen bond between the dimers. Regardless of which truncation, the functional groups exposed on (100) are different to that of (001), which have more C-H_x character. Therefore, as crystals of different morphology have different surface area exposed for each face, their overall properties can vary, including the dissolution rate, chemical reactivity, flow properties, *etc.*

The anisotropic nature of ASA crystals has been studied by various groups. Danesh *et al.* was the first to study the dissolution rate of (100) and (001) by *in situ* AFM imaging [96]. The results showed that in an acidic medium, the (001) face dissolves by receding step edges (Figure 3.4(a) to (c)), six times slower than the dissolution of the (100) face, which dissolves via a terrace sinking mechanism (Figure 3.4(d) to (f)).

Ex situ AFM dissolution studies were conducted by Wen *et al.* [94]. Etching patterns on (100) were analysed, and the results indicated that these patterns were affected by the attachment energy, solvents with different solubilizing ability and surface adsorption potential (Figure 3.5). The attachment energy was the dominant factor, as faces of higher surface energy were dissolved, with resulting etching patterns mainly containing steps aligned to the faces of smallest surface energy, which in the case of ASA crystals, were {001}, {011}, and {010}.

The wettability and hydrophilicity of ASA faces was investigated by Heng *et al.* [169] using sessile drop contact angle measurements and X-ray photoelectron spectroscopy (XPS). Large crystals of more than 2 cm in length were grown in acetone, and cleaved crystal faces of (100), (001), and (011) were studied. Contact angle measurements using water droplets indicated that out of the three faces, (011) was the most hydrophilic, followed by (100) and (001). This ranking was supported by XPS findings, as (011) and (100) had a higher proportion of C=O functionality than (001) due to the terminal ester group or carboxylic acid group being exposed on (011) and (100), while (001) had more C-H_x functionality, accounting for its more hydrophobic nature (Figure 3.6).

ASA surface hydrophilicity was also studied by Aubrey-Medendorp *et al.* [170], whom reported different contact angle measurement results. Only (100)

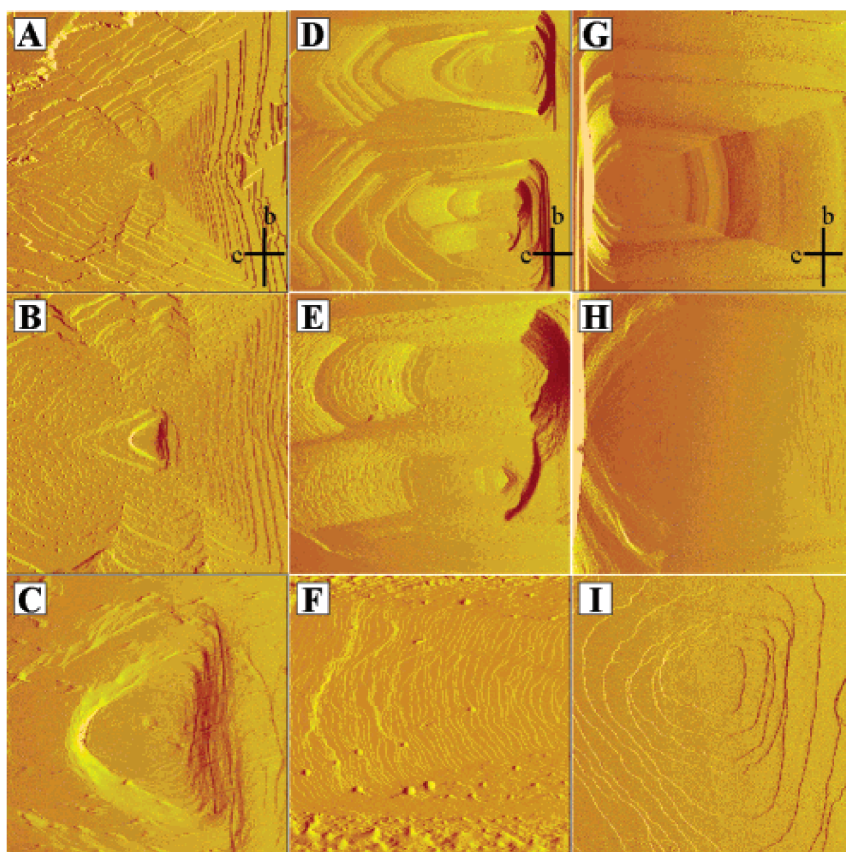


Figure 3.5: AFM Deflection images of ASA (100) face etched by water (A-C), acetone (D-F), and ethyl acetate (G-I) with image sizes of $60 \times 60 \mu\text{m}^2$ (A, D, G), $20 \times 20 \mu\text{m}^2$ (B, E, H), and $5 \times 5 \mu\text{m}^2$ (C, F, I). Directions of the b and c axis are shown in figures A-C. Adapted from reference [94].

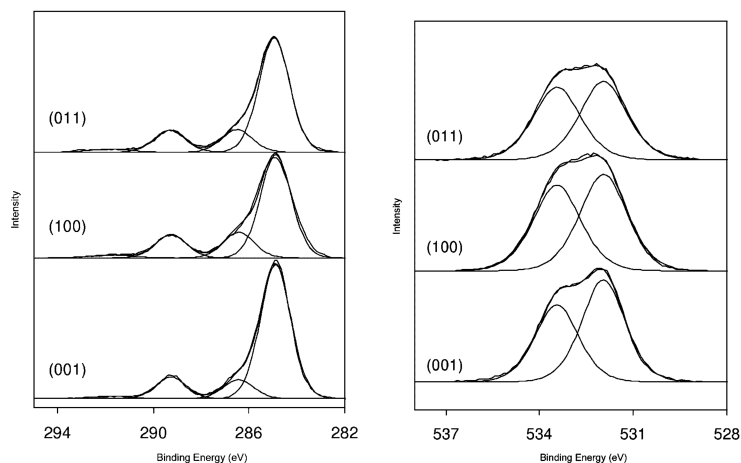


Figure 3.6: Carbon 1s (left) and oxygen 1s (right) XP spectra of ASA crystal faces, showing the deconvoluted C and O environments. Adapted from reference [169].

and (001) were considered, and from the water contact angle measurements, the results indicated that in fact (001) was more hydrophilic than (100). This was in contradiction with Heng's findings. The authors, however, did not report any other complementary analytical techniques to support their contact angle

measurements, and the hydrophilicity ranking of the two faces was not clearly justified.

Based on both reports, the only main difference between the two water contact angle studies conducted by Heng *et al.* and Aubrey-Medendorp *et al.* was probably how the crystals were prepared. While Heng's crystals were recrystallised from acetone, Aubrey-Medendorp *et al.* only reported that the crystals were recrystallised in either acetone or ethanol, but did not specify which one. The reason for the discrepancy in hydrophilicity ranking is unknown, and there have been no reports on whether a change in solvent used for recrystallisation could affect the behaviour of resulting cleaved crystal faces. Heng's XPS data provides stronger evidence that (100) is the hydrophilic face. However, further experiments are required to confirm these contact angle measurements.

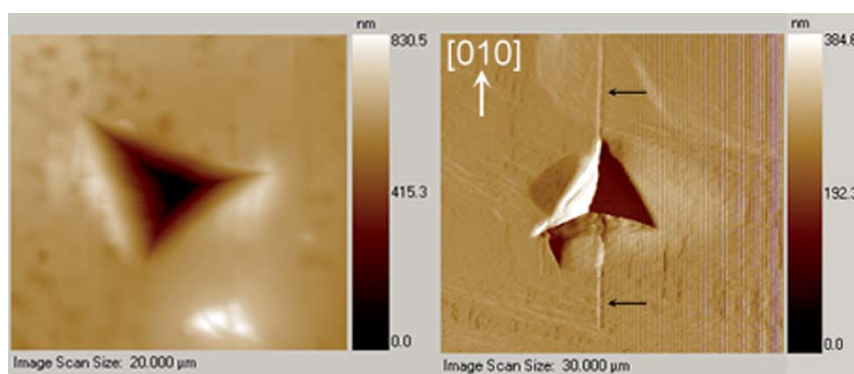


Figure 3.7: AFM image of (001) [left] and (100) [right] after nanoindentation. Adapted from reference [171].

More recently, nanoindentation was used to study ASA crystal faces [171]. (100) and (001) of ASA form I were studied, and each face was characterised by its hardness, elastic modulus. The hardness of the two faces were similar, but (001) had a significantly greater elastic modulus than (100). The resulting nanoindentation pattern also revealed that cracks formed along (100) but not in (001), due to the presence of a slip plane along [001] but not along [100] (Figure 3.7). The higher elastic modulus of (001) was also due to the presence of slip planes along [001].

3.4 Importance of surface studies on the solid-state hydrolysis of ASA

Considering the anisotropic nature of ASA surfaces, it is likely that each face will respond differently upon exposure to moisture and hydrolysis. Despite many studies on the solid-state hydrolysis of ASA in the past, only one of

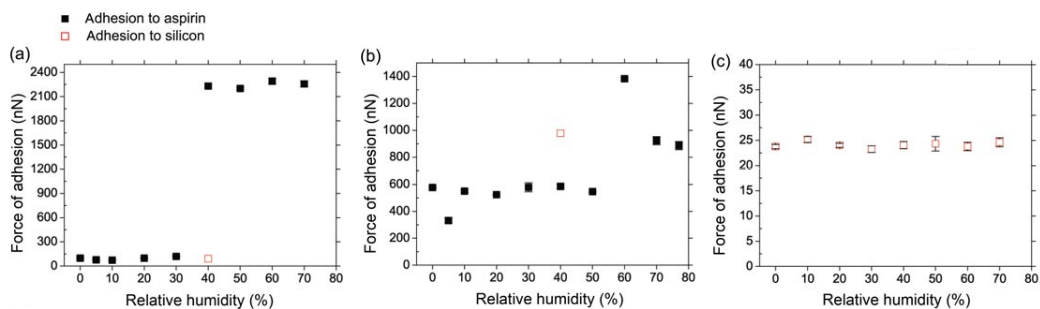


Figure 3.8: The measured force of adhesion values at different RH levels between dicalcium phosphate probes and (a) ASA (100); (b) ASA (001); and (c) a Si reference surface. Adapted from reference [172].

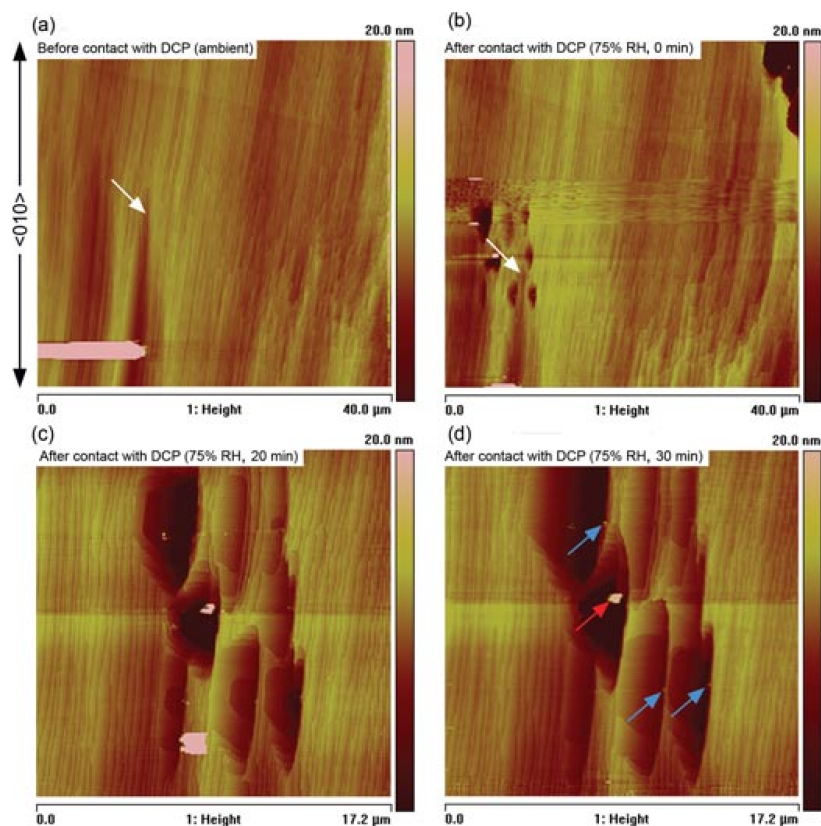


Figure 3.9: AFM height profile of ASA (100)(a) under ambient conditions before dicalcium phosphate contact; (b) at 75% RH after dicalcium phosphate contact; (c) after 20 min; (d) after 30 min. The same sites in (a) and (b) are marked by white arrows. The blue and red arrows in (d) are areas of growth normal to (100). Adapted from reference [172].

them have taken surface anisotropy into account. Cassidy *et al.* studied the surface response of the (100) and (001) faces in the presence of moisture and dicalcium phosphate dihydrate [172], which is a common drug excipient. Colloid probes of dicalcium phosphate were used to measure the force of adhesion between dicalcium phosphate and each of the two ASA faces at different relative humidity (RH) levels (Figure 3.8). While the force of adhesion showed a strong dependence on RH for the interactions between dicalcium phosphate

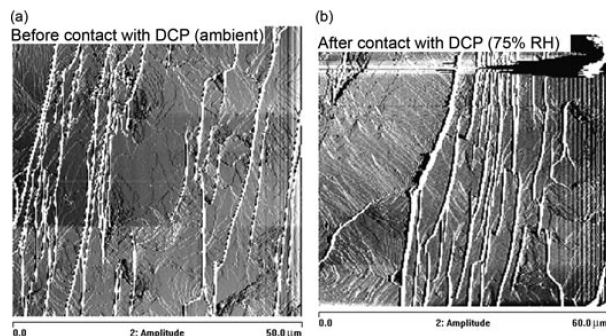


Figure 3.10: AFM amplitude profile of ASA (001) under ambient conditions before contact with dicalcium phosphate. (b) AFM amplitude profile of the same location as (a) at 75% RH after contact with dicalcium phosphate. Adapted from reference [172].

and (100), with stronger interactions occurring at higher RH, much weaker interactions were measured between dicalcium phosphate and (001) under all RH conditions. Moreover, the authors used AFM imaging to monitor the changes on each face before and after dicalcium phosphate contact. At 75% RH, contact between dicalcium phosphate and (100) led to the development of etch pits (Figure 3.9), and in some cases needle growth normal to the surface, postulated to be SA. No such changes were observed for the contact between dicalcium phosphate and (001). Instead, step movement was observed on (001) (Figure 3.10), which was not a result of the dicalcium phosphate in contact but of the partial dissolution of the surface. Therefore, it was concluded that there was strong reaction between dicalcium phosphate and (100) but no reaction between dicalcium phosphate and (001).

Cassidy's study has clearly highlighted the difference in hydrolysis reactivity on different ASA crystal faces. In Chapter 6, a study involving the surface response of ASA crystals to humidity (without excipients) will be presented, in hope to obtain a more fundamental understanding of the nature of this reaction.

Chapter 4

Experimental Methods

4.1 Optical microscopy

Two optical microscopes were used for recording micrographs. A Leica DM1000 LED transmission optical microscope equipped with a JVC colour video camera was used to record micrographs of samples, while a binocular GX reflective optical microscope equipped with a Motticam 2000 microscope digital camera was used to record micrographs of samples on an AFM metallic sample disc. Objectives ranged from $\times 4$ to $\times 60$.

4.2 Attenuated total reflection – Fourier transform infrared spectroscopy

Attenuated total reflection Fourier transform infrared (ATR-FTIR) spectra of samples were collected on a ThermoNicolet Nexus FT-IR spectrometer with an XT-KBr beam splitter, Smart Golden Gate Single Reflection ATR accessory. Samples were measured from 500 to 4000 cm^{-1} at a resolution of 4 cm^{-1} and 32 scans.

4.3 Powder X-ray diffraction

Powder X-ray diffraction (PXRD) was used for identifying crystalline structures. Data was collected on a laboratory Philips X'Pert Pro diffractometer, using Ni-filtered $\text{CuK}\alpha$ ($\lambda = 1.5418 \text{ \AA}$) at 40 kV and 40 mA with an X-Celerator RTMS detector. Each sample was analysed in the range of $5^\circ \leq 2\theta \leq 50^\circ$ with a total scanning time of approximately 3 minutes. Samples were supported on a flat glass slide with a shallow depression to accommodate the material.

A plot of diffracted intensity versus the 2θ diffraction angle gave a fingerprint pattern that was unique for each crystal structure. These patterns were compared with the powder patterns simulated by structures found in the Cambridge Structural Database.

4.4 The Cambridge Structural Database and BFDH morphology prediction

The Cambridge Structural Database (CSD) contains data for over 600000 small molecule crystal structures. Conquest version 1.15 was used to search the CSD for the required crystal structures. Mercury was used to generate simulated PXRD patterns from the searched structures. These patterns were used as identification for crystal structures obtained from experiment.

The predicted crystal morphology of different crystal structures was obtained using the Bravais-Friedel-Donnay-Harker (BFDH) geometric model [173], included in the Mercury software. These were compared to the experimental crystal morphologies to index and determine the orientation of the crystal face that was studied.

4.5 Atomic Force Microscopy

4.5.1 Instrumental details

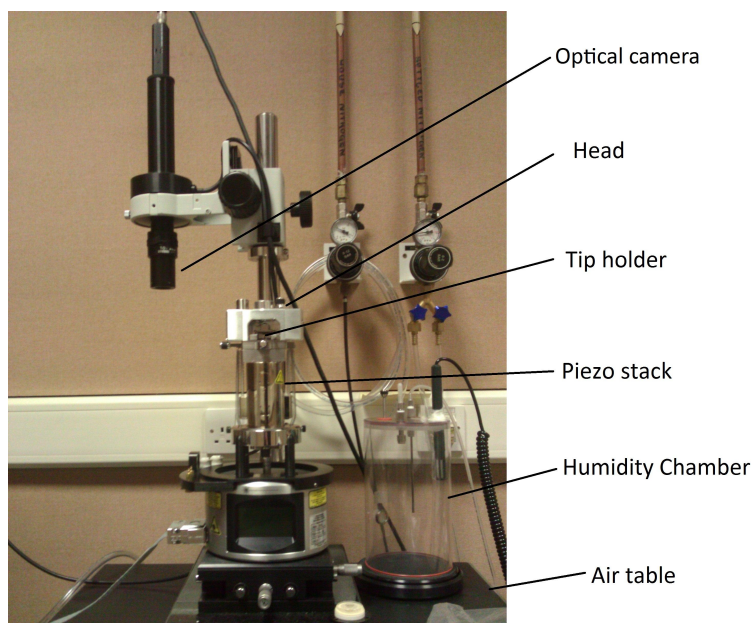


Figure 4.1: Picture of the Multimode AFM instrument with labelled parts.

The AFM images were recorded using a Multimode AFM (Figure 4.1), operated by a Nanoscope IIIa controller, with a Quadrex extender module interface (Veeco Instruments, Cambridge, UK).

Two scanners, namely E and J, were available and used for imaging. The E scanner has lateral scan size of approximately $10 \times 10 \mu\text{m}^2$, with a $2.5 \mu\text{m}$ height range, while the J scanner has a lateral scan size of approximately $120 \times 120 \mu\text{m}^2$, with a $5 \mu\text{m}$ height range. The E scanner was used for most experiments, as it had a better accuracy in scanning areas of $10 \times 10 \mu\text{m}^2$ or less. The J scanner was used for experiments that required the use of a chamber to control the RH level. This was because the humidity chamber prevented the access to the knobs for adjusting the tip position. Tip re-positioning could only be achieved by the software, and the area that the tip could cover was limited by the scanner. The J scanner was therefore selected to provide greater flexibility in choosing areas for imaging.

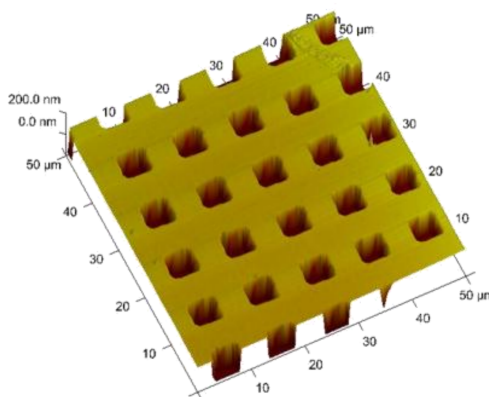


Figure 4.2: 3-D height profile of a standard calibration grid ($50 \times 50 \mu\text{m}^2$).

Standard calibration grids were imaged (Figure 4.2) regularly to ensure the accuracy of the instrument. The grid images were measured to be within 2% of the correct dimensions before imaging other samples of interest. The instrument would require calibration if errors exceeded such values, or if distorted images were observed due to bowing and creeping effects of the piezo stack.

The optical microscope shown in Figure 4.1 is equipped with a digital camera, which aids the positioning of the tip on to the sample, and allows the tip to be repeatedly mapped onto the same area of interest if required.

4.5.2 Cantilever selection and tip-to-sample force

Intermittent contact mode imaging was the main imaging mode used, due to the soft nature of the organic crystals studied. Commercially available FESP

18 series or TESP 15 series sharpened Si probes were used. The nominal k_{cant} values are 3.5 N/m and 40 N/m respectively, and both tips have an average radius of curvature of 10 nm, and a cone angle of less than 30° (Mikromasch, Estonia).

The tip-to-sample force can be measured using the amplitude setpoint ratio between that during imaging and when freely oscillating (A/A_0). Typical setpoint ratios used for imaging are above 0.8 to minimise any tip influence on the surface.

4.5.3 Sample preparation and area of selection

Samples were generally prepared on glass or mica coverslips by one of the two methods:

1. Evaporation of a drop of solvent containing dissolved material, yielding crystals adhered onto the coverslips.
2. Mounting preformed crystals onto coverslips using quick dry glue or epoxy resin.

The coverslips were then attached to stainless steel AFM sample discs, which “snapped” onto the (magnetic) sample stage.

In choosing area of imaging, the optical microscope was used to identify surfaces that were flat and contained no distinct features at the optical scale (Figure 4.3). This was to ensure that any fluctuation in the height of the sample was minimized and was within the height range detected by the AFM (2.5 or 5 μm , depending on the scanner).

4.5.4 Recording and processing AFM images

Data was recorded using the Nanoscope software version 6.13. Prior to imaging, the amplitude setpoint was optimised such that the tip was tracing the surface of the sample with minimum force exerted on the sample by the tip. Images were recorded with a scan rate of 1 Hz, with scan size varying from $1 \times 1 \mu m^2$ to $20 \times 20 \mu m^2$. In some cases, imaging at a lower scan rate and harder tip-to-sample force was required. Data acquired from the instrument was processed using NanoScope Analysis version 1.4.

Plane fitting and flattening

Recorded images were plane fitted to remove the effect of any inclination of the sample relative to the tip, resulting in a better representation of the surface

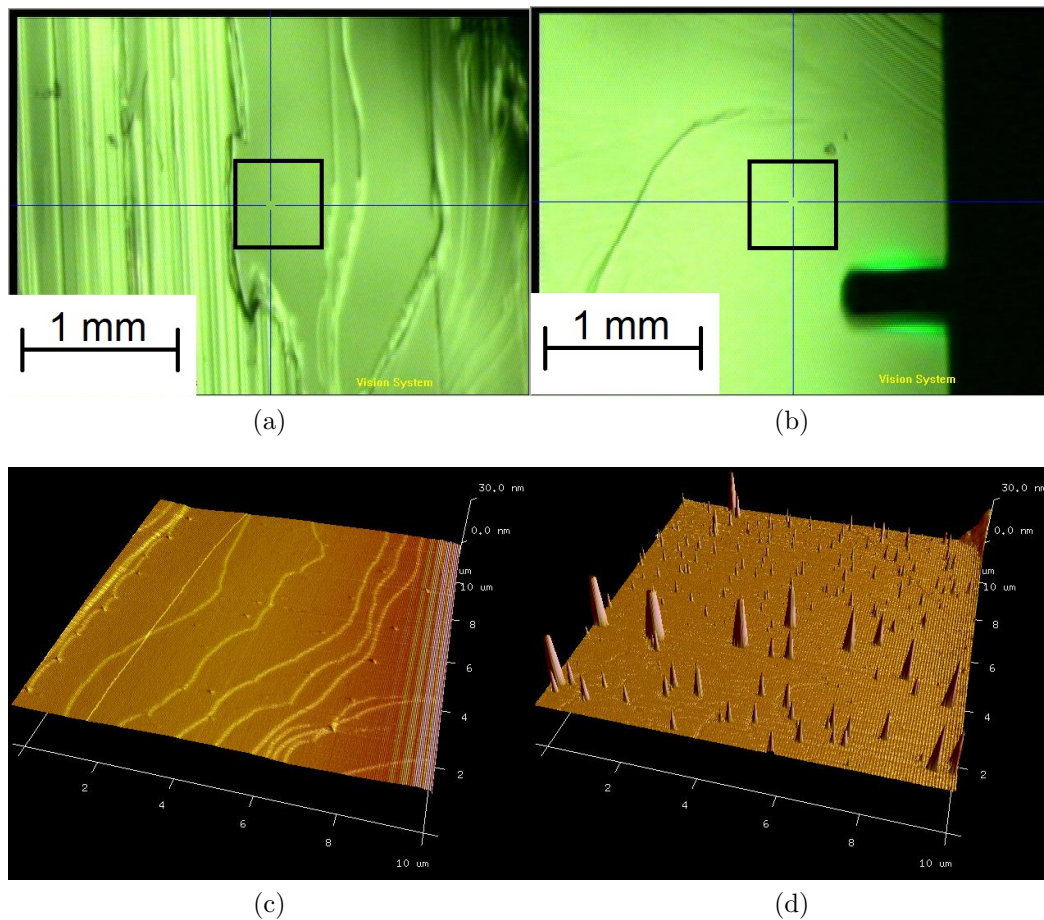


Figure 4.3: Optical microscope image of two aspirin crystal surfaces (treated under different conditions)((a), (b)); 3-D height profile of the two surfaces ((c), (d)), which was recorded within the area enclosed by the black rectangles in (a) and (b) respectively. The area of both images are $10 \times 10 \mu\text{m}^2$, with the height range of 80 nm.

topography. First order plane fitting was usually sufficient. In some cases, a second or third order plane fit gave rise to a better representation of the surface, removing the bowing artifact introduced by the piezoelectric set up of the instrument.

Some images required flattening, which is a process that removes image artifacts due to vertical scanner drift. This modifies each line of the image, removing the vertical offset between adjacent scan lines in the fast scan direction by calculating a least squares fit polynomial for a scan line, and subtracting it from the polynomial fit from the original line.

Colour scales and 3-D images

A colour scale was use to represent the vertical height (along the z -axis) or the amplitude response at each pixel of the imaged area. In the case of vertical height, the colour scale starts with a dark brown colour indicating low

topography, and gradually turning to a light pink colour to represent higher topography. The colour scales can also be applied to 3-D images for better visualisation of surface features.

4.5.5 Surface roughness

The surface roughness can be measured based on a quantified area on a sample surface. For this thesis, the root mean square surface roughness (Rq) was used, which is the average deviation in the topography from an average plane running perpendicular to these deviations:

$$Rq = \left[\frac{1}{N} \sum_{n=1}^N (y_n)^2 \right]^{\frac{1}{2}} \quad (4.1)$$

In the equation above, N is the total number of data points within a given area, and y_n is the difference between the height value of each data point and the average height value within the given area.

4.5.6 Cross sectional analysis

For crystal surfaces that are flat on the optical scale, step features of 5 to over 40 Å thick were normally present. Another feature that often appeared on surfaces was the emergence of “tall” features. Using a cross sectional height analysis, the height of these steps and tall features could be measured, as shown in Figure 4.4(a) and (c). Better accuracy in measuring the step heights was obtained by taking the average height measured by several cross sectional lines running across the step (Figure 4.4(b) and (d)).

4.6 Relating surface orientation to crystal structure

Face indexing and the orientation of the surface relative to the crystal structure were determined by 1-D XRD and comparison of experimental and predicted morphology respectively. The normal PXRD instrument was used for 1-D XRD, but instead of a powder sample, it was replaced by a coverslip containing the crystals prior to AFM imaging. A plot of diffracted intensity versus 2θ was used to identify the top crystal face. An example of a cleaved aspirin crystal is shown in Figure 4.6, which only 1 reflection was observed in the 1-D XRD spectra (Figure 4.5 (b)). This corresponded to d_{002} , and confirmed that (001)

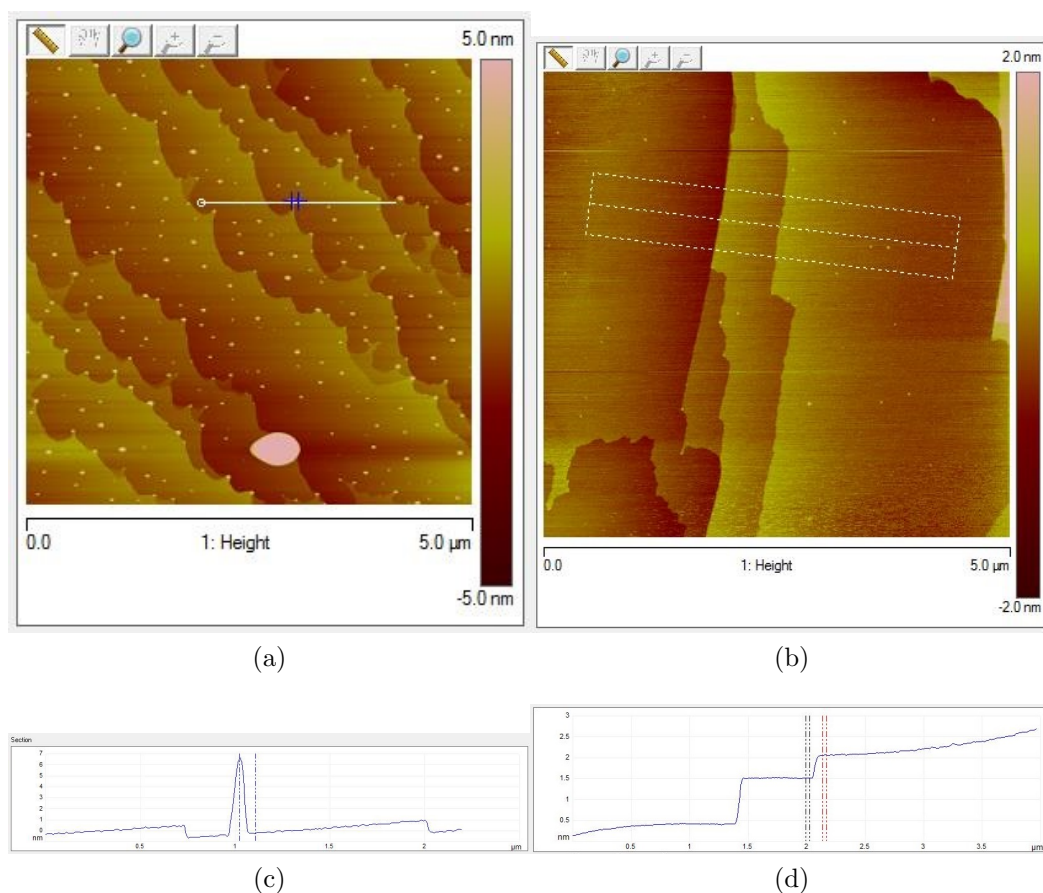


Figure 4.4: (a) AFM height profile of an aspirin crystal surfaces showing both molecular steps as well as tall features growing perpendicular to the surface ($5 \times 5 \mu\text{m}^2$); (b) AFM height profile of another aspirin crystal surface showing only molecular steps ($5 \times 5 \mu\text{m}^2$); (c) A cross sectional plot along the white line in (a), allowing the height of features to be measured; (d) The average cross sectional plot taken across the step enclosed by the broken lines in (b), which provides a better accuracy to measuring the step height.

was the top face (there is a systematic absence for d_{001}).

For crystals formed by evaporation of solvent on the coverslip, 1-D XRD only provides an average representation of the many small crystals on the coverslip (Figure 4.7). However, as most crystals studied had a strong preferred orientation to crystallise with the dominant growth face on the top of the coverslip, the resulting XRD spectra contained only the reflections arising from the d_{hkl} spacing (corresponding to the dominant face (hkl)). From the spectrum of these ASA crystals, d_{100} , d_{200} , d_{300} , d_{400} were observed (Figure 4.7 (a)), confirming that the top face is (100).

Once the top face was indexed, the morphology was used as an indicator to map out the relative orientation of the crystal surface relative to the structure, as shown in Figure 4.8.

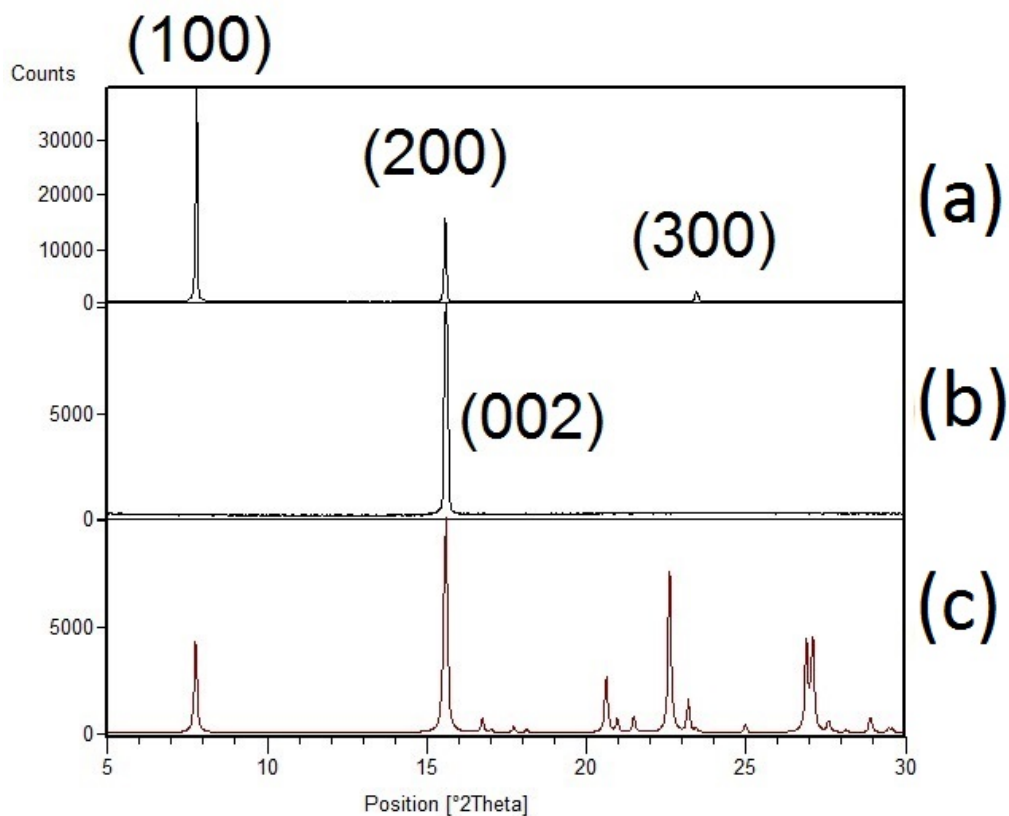


Figure 4.5: 1-D XRD spectra of (a) ASA crystals formed by direct evaporation crystallisation on the coverslip, showing 3 reflections corresponding to d_{100} , d_{200} , and d_{300} ; (b) recrystallised ASA crystals (in acetone) of over 5 mm in length mounted on an AFM sample disc (Figure 4.6), which gave rise to only one reflection corresponding to the d_{002} spacing; (c) simulated PXRD pattern of ASA form I (CSD ref code ACSALA01) [168].



Figure 4.6: Picture of two sections of a large single crystal prepared by cleaving along the length of the crystals. The crystals were glued onto coverslips that were attached to stainless steel discs.

4.7 Controlled humidity environment

For experiments conducted under controlled humidity, desiccators of different relative humidity (RH) were set up at room temperature. P_4O_{10} was added to the desiccator that maintained a 0% RH environment, while saturated solution

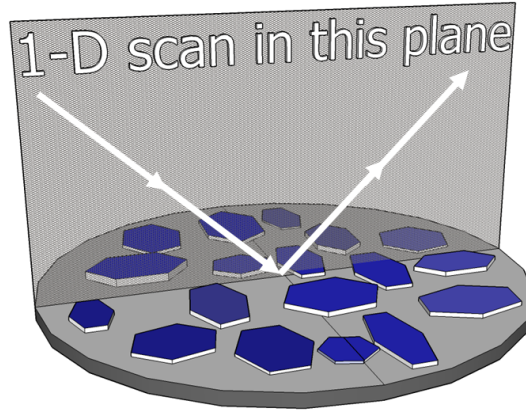


Figure 4.7: Schematic illustration of a 1-D X-ray diffraction on coverslip containing crystals to be studied by AFM, with most crystals having the dominant face on top.

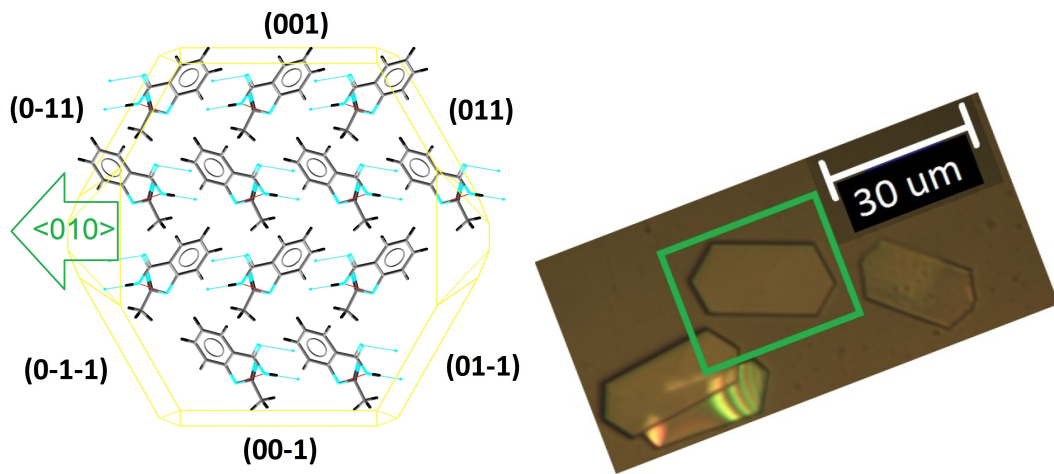


Figure 4.8: Crystal structure of ASA viewed onto $\{100\}$ (left) compared to the optical microscope image of the crystal surface prepared by quick evaporation (green rectangle)(right).

of salts for other RH environments were used, *e.g.* $\text{Mg}(\text{NO}_3)_2$ for 53% RH and K_2SO_4 for 98% RH [174]. These chambers were monitored with humidity-indicator cards available from the Sigma-Aldrich Company. Although the temperature was not controlled and was observed to vary from 18 to 23°C, the fluctuation of the humidity is expected to be no more than 2% RH.

4.8 X-ray photoelectron spectroscopy

X-ray photoelectron spectroscopy (XPS) studies presented in this thesis were conducted by collaborators Sven Schroeder and Lauren Newton from University of Manchester. Details of the experiment can be found in reference [175]. In summary, the spectra were recorded with a Kratos Axis Ultra instrument using a monochromatic $\text{AlK}\alpha$ source (1486.69 eV) and a hybrid hemispherical analyser (electrostatic and magnetic). The X-ray source power was set to 180

W (15 kV and 12 mA), with a pressure lower than 10^{-8} mbar during data acquisition. High-resolution spectra were measured for the C 1s spectral range with 0.1 eV steps and 1000 ms dwell time per data point. Repeats were carried out to verify if there was any radiation damage.

Theoretical spectra were generated based on the identity of the molecule in a crystal structure. These were compared with the obtained experimental spectra in order to identify the chemical environment of the carbon atoms detected on the studied crystal surface.

Chapter 5

Organic surfaces imaged by AFM

5.1 Introduction

5.1.1 The nature of AFM imaging technique and organic crystals

In the previous chapter, an introduction to AFM was given, together with various studies of organic crystals using this technique. This chapter will focus on addressing potential issues concerning the nature of organic crystals, as well as the AFM imaging technique.

Compared to metals and inorganic crystals, organic crystals are generally softer and have weaker intermolecular forces that hold molecules together. As a result, organic crystals tend to have higher vapour pressures, and are more susceptible to sublimation. During sublimation, molecules at the surface are more likely to sublime than molecules in the bulk crystal. Therefore, when accounting for any changes observed on organic crystal surfaces imaged by AFM (*e.g.* step rearrangement), the natural sublimation of the material must be considered in addition to other factors.

As the nature of AFM imaging involves physical interaction between the tip and the sample surface, there is a possibility of the tip influencing the imaged surface, especially for soft organic crystals. This has been demonstrated by Matlis *et al.* [176], who studied benzamide crystal surfaces by AFM continuous imaging using both tapping and contact mode. Monomolecular steps were observed to move across the imaged areas, which corresponded to the sublimation of molecules at the step edge (Figure 5.1). The sublimation rate on the crystal surface was measured by recording the time taken for one molec-

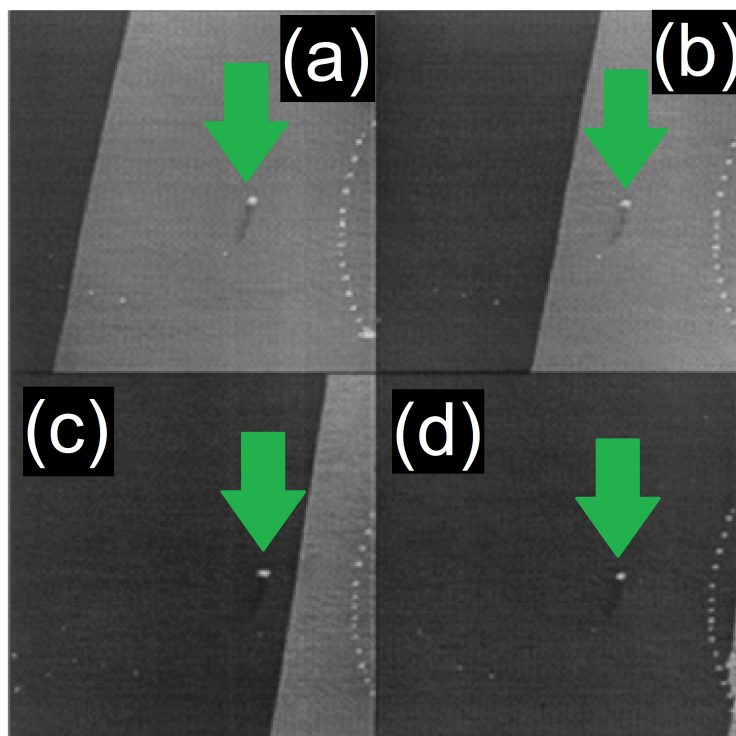


Figure 5.1: Four consecutive AFM height images of a benzamide crystal surface ((a) to (d)). The arrows indicate a reference feature. Each image area was $4.5 \times 4.5 \mu\text{m}^2$. Adapted from reference [176].

ular step to move across the imaged area, which was found to increase as a greater tip-to-sample force was applied to imaging (for both contact and intermittent contact modes). This provided evidence that the tip can influence the behaviour of soft sample surfaces, especially at greater tip-to-sample forces.

While there have been reports of intentionally promoting surface changes by applying a greater tip-to-sample force [133, 177], the focus of this chapter is drawn towards identifying any unintentional tip influence on the samples that are to be studied by AFM, and whether the tip influence can be prevented by any means.

5.2 Natural sublimation of organic crystals and the influence of the AFM tip

Four organic materials were selected for this study, namely aspirin (ASA), salicylic acid (SA), anthracene (AN), and theophylline (TP). All of the four starting materials were sourced from Sigma Aldrich. Each chemical was dissolved in ethyl acetate until the solution was saturated. The solutions were then filtered, and one drop of each resultant solution was evaporated on cover-

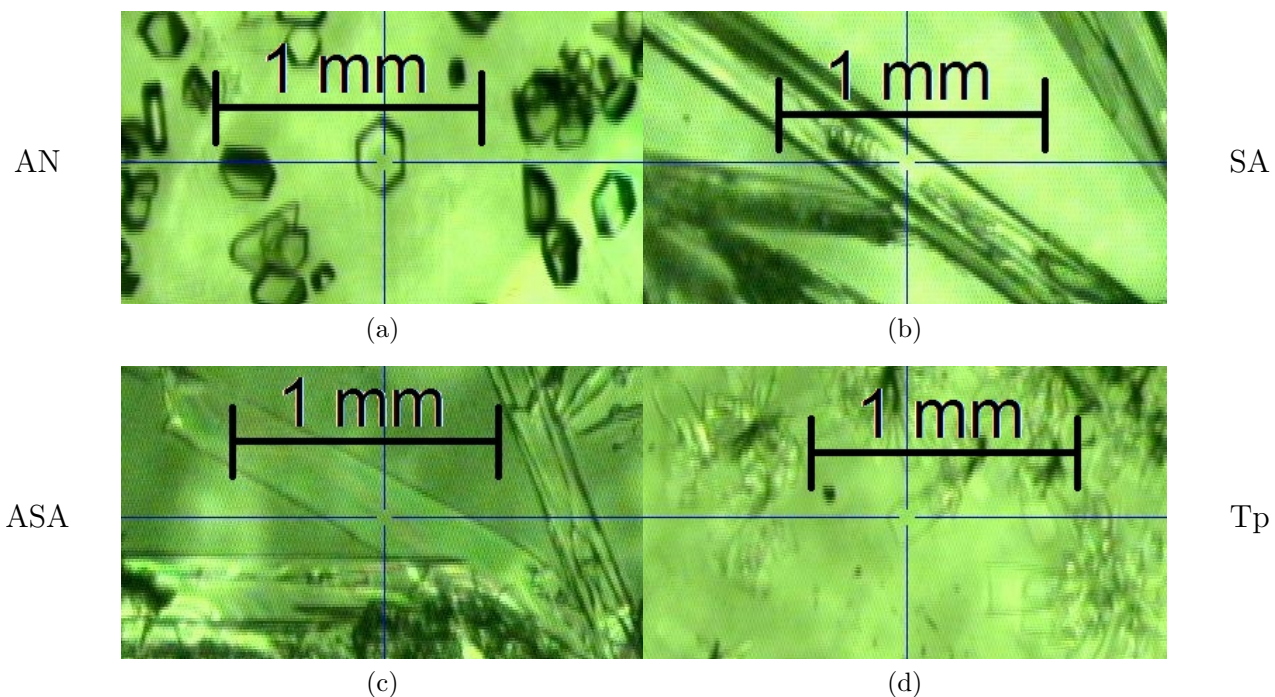


Figure 5.2: Optical microscope images of crystals formed on coverslips: (a) anthracene (AN), (b) salicylic acid (SA), (c) aspirin (ASA), and (d) theophylline (TP). The crystal at the middle of each image was selected to be studied by AFM.

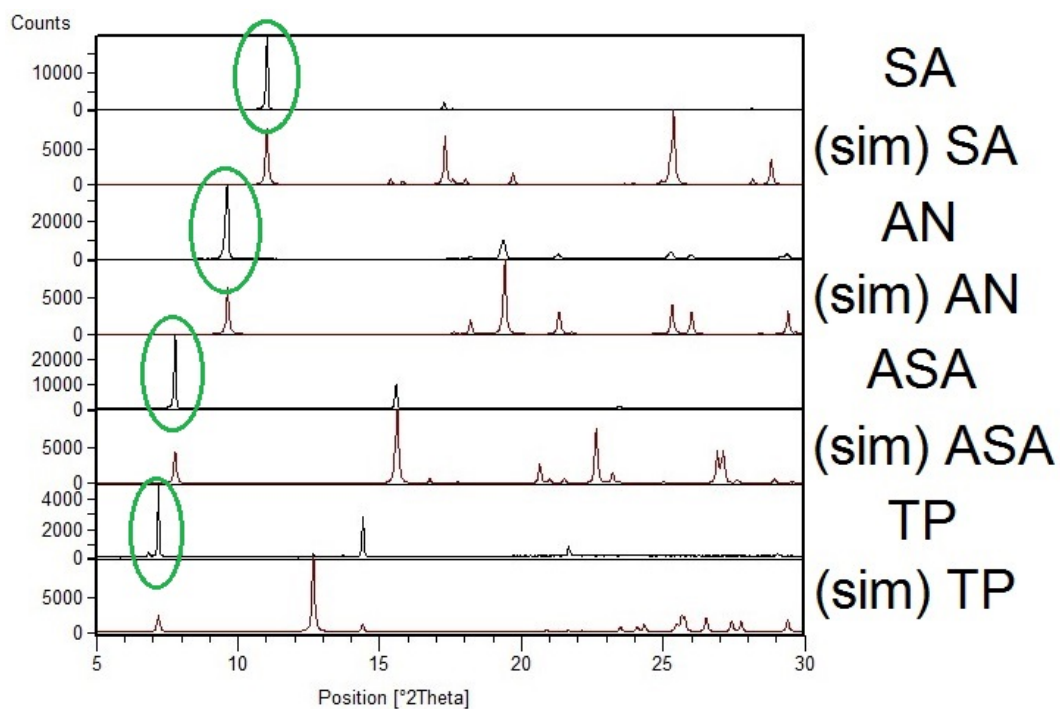


Figure 5.3: 1-D XRD pattern of crystals grown on coverslips and the corresponding simulated powder pattern. The peaks circled in green suggest that the top crystal surfaces on the coverslips are (001) for AN, (011) for SA, (100) for ASA, and (200) for TP. The simulated powder patterns were generated according to crystal structures from references [168, 178–180].

slips. Crystallisation occurred on the coverslips (Figure 5.2), and the general orientation of the crystals were determined by 1-D XRD (Figure 5.3) together with a comparison between experimental and predicted morphologies. The top crystal surfaces were identified as (001) for AN, (011) for SA, (100) for ASA, and (200) for TP.

Each sample was imaged by tapping mode using a fixed amplitude set-point ratio of $A/A_0 = 0.8$. The AFM imaging sequence was as follows:

1. An image of $5 \times 5 \mu\text{m}^2$ was recorded initially
2. A closeup area in the middle region ($3 \times 3 \mu\text{m}^2$) was continuously imaged for 10 frames, at a scan rate of approximately 4 minutes per frame.
3. A final image of the original size ($5 \times 5 \mu\text{m}^2$) was recorded.

Throughout this imaging sequence, the repeatedly imaged area in the middle would have experienced greater tip interaction than its surroundings. Therefore, a comparison between these two areas on the surface could determine whether there was any significant influence on the surfaces exerted by the tip. As the surrounding area was the least disturbed by the AFM tip, this was used as an indicator of any natural sublimation occurring on the surface.

Representative AFM images of each crystal are shown in Figures 5.4 to 5.7. The main features on each surface were steps of one to two molecules thick. Some round tall features were also observed on SA and ASA. Although the chemical composition of these features are not known, these features did not change in height or position within the studied period. Therefore, these features, together with some distinct step patterns, were used as reference points to relate the exact position of all the images recorded for each crystal (circled in green).

In the case of AN (Figure 5.4), step movement was detected in the area that was repeatedly imaged, as well as its surrounding area. This is believed to be a result of the natural sublimation of AN molecules on the surface. In addition, tall features emerged from the surface, which is suspected to be the photodimerisation of surface AN molecules under room lighting conditions. The mechanism of the photochemical reaction to form these features will be probed further, and is discussed in Chapter 7.

Even greater step rearrangement was observed on the SA surface for both the repeatedly imaged region and its surrounding (Figure 5.5), suggesting that the sublimation activity on SA is greater than that of AN. In contrast, there were no changes on the ASA surface apart from one step rearrangement in a

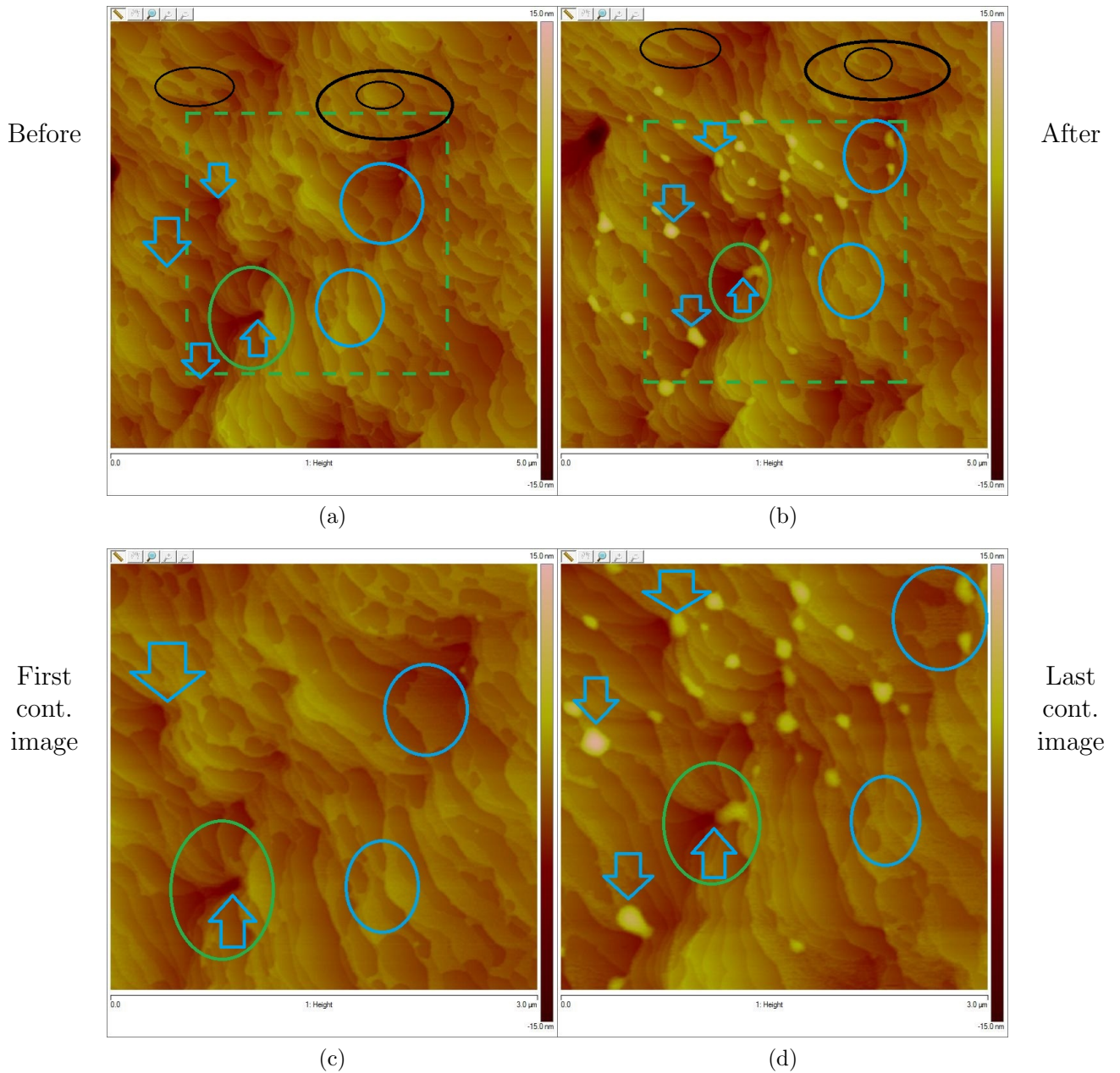


Figure 5.4: AFM height images of AN (001) surface before (a) and after (b) continuous imaging ($5 \times 5 \mu\text{m}^2$). Continuous imaging was conducted over an imaging area of $3 \times 3 \mu\text{m}^2$. (c) and (d) show the first and last of the continuous imaging series, which correspond to the area enclosed by the dotted green rectangles in (a) and (b) respectively. The green circle shows common features observed on all four images. The black circles indicate regions of step movement outside the repeatedly imaged area, while the blue circles indicate step movement within the repeatedly imaged area. The blue arrows indicate formation of new features.

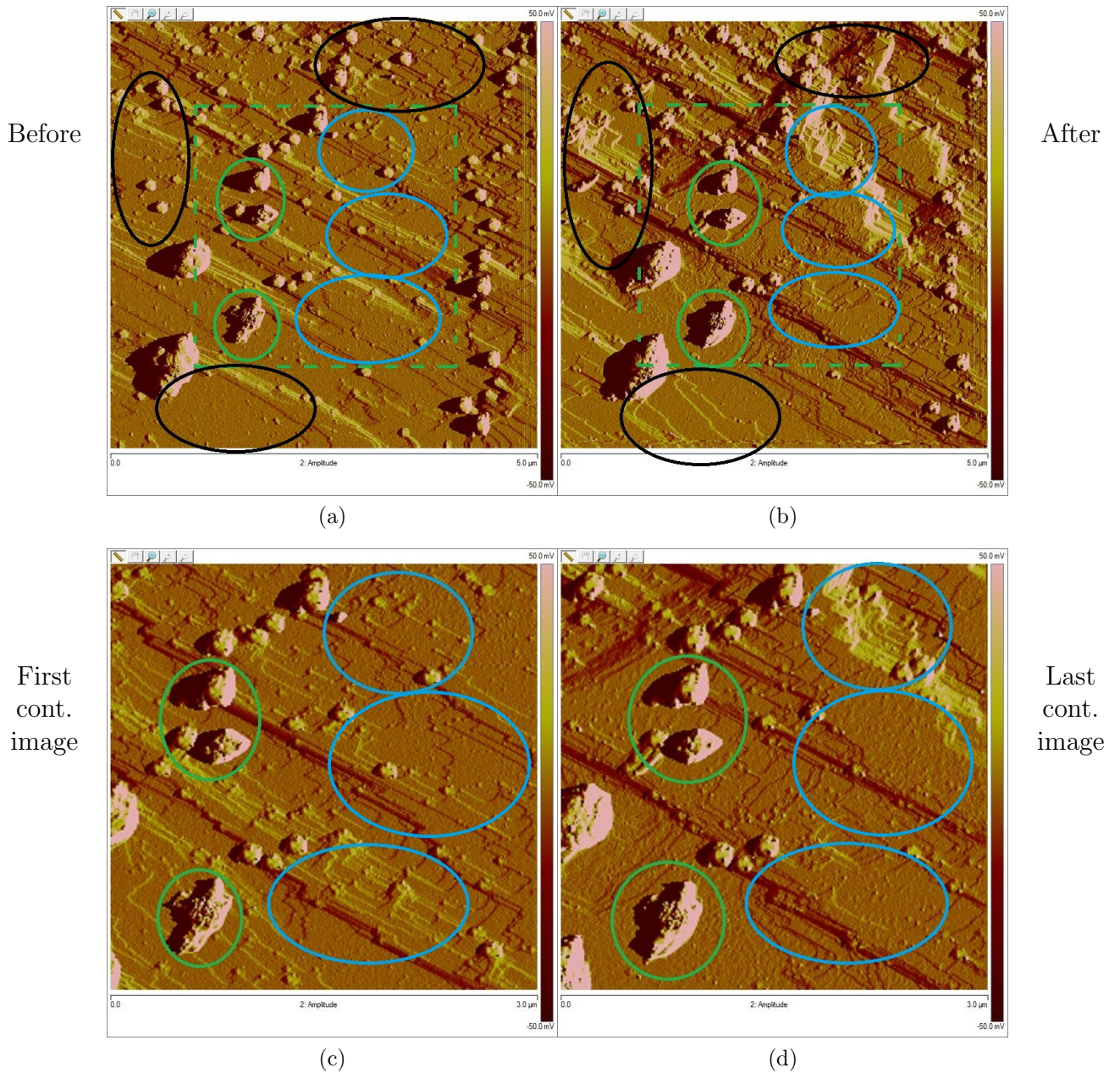


Figure 5.5: AFM amplitude images of SA (011) surface before (a) and after (b) continuous imaging ($5 \times 5 \mu\text{m}^2$). Continuous imaging was conducted over an imaging area of $3 \times 3 \mu\text{m}^2$. (c) and (d) show the first and last of the continuous imaging series, which correspond to the area enclosed by the dotted green rectangles in (a) and (b) respectively. The green circle shows common features observed on all four images. The black circles indicate regions of step movement outside the repeatedly imaged area, while the blue circles indicate step movement within the repeatedly imaged area.

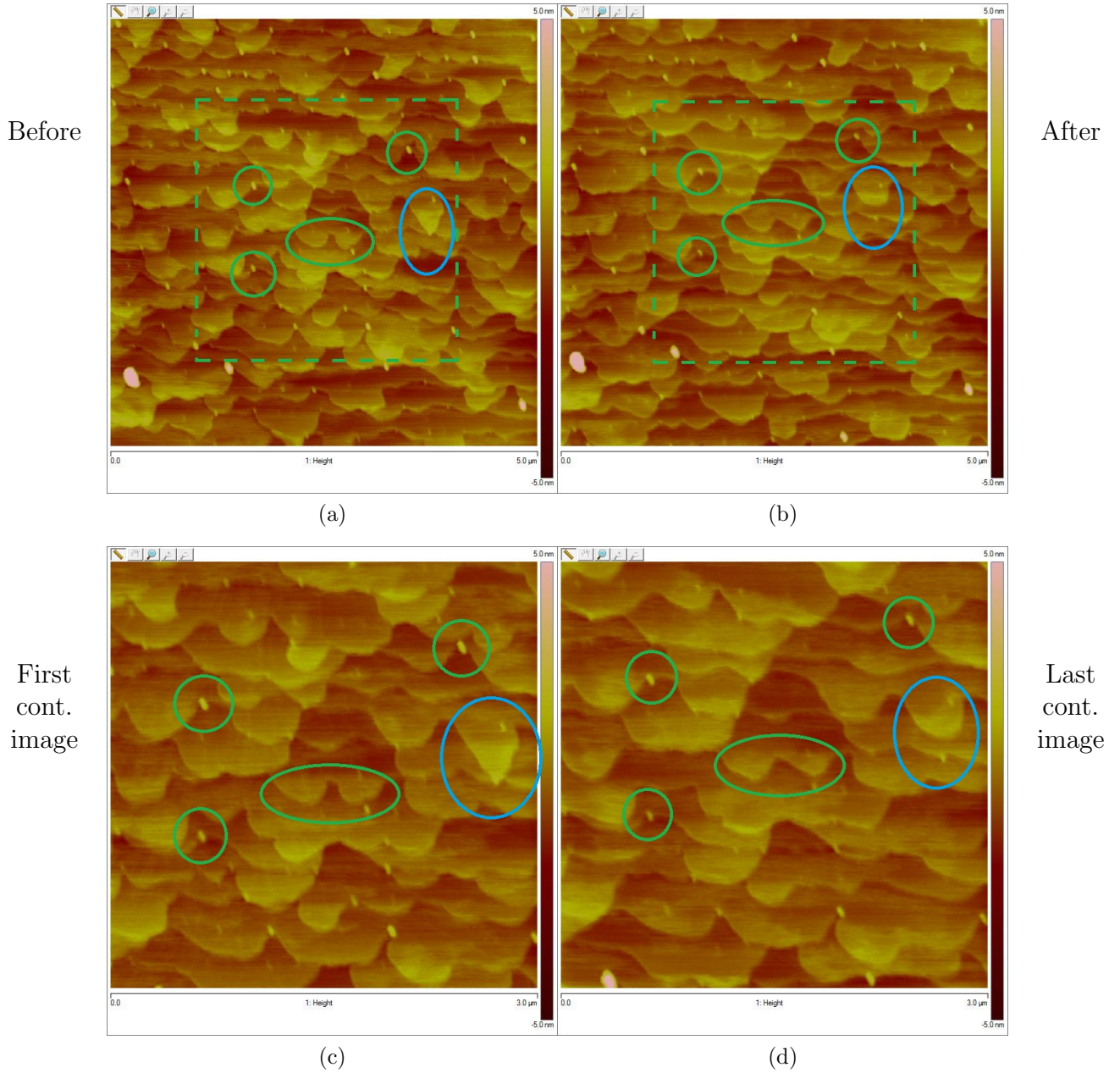


Figure 5.6: AFM height images of ASA (100) surface before (a) and after (b) continuous imaging ($5 \times 5 \mu\text{m}^2$). Continuous imaging was conducted over an imaging area of $3 \times 3 \mu\text{m}^2$. (c) and (d) show the first and last of the continuous imaging series, which correspond to the area enclosed by the dotted green rectangles in (a) and (b) respectively. The green circle indicates the common features observed in all four images, while the blue circles is the only area of minor step arrangement observed throughout the surface.

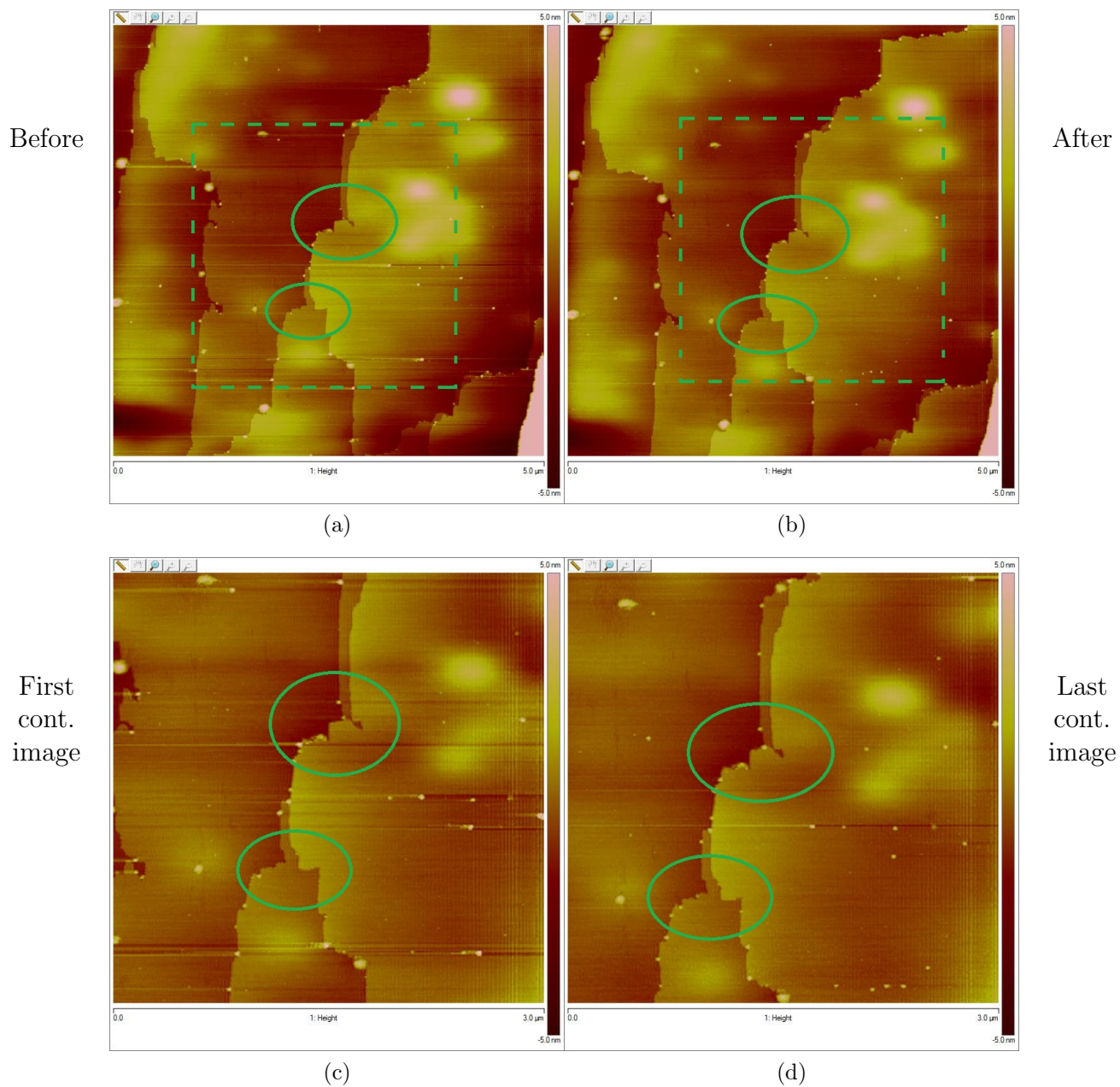


Figure 5.7: AFM height images of TP (200) surface before (a) and after (b) continuous imaging ($5 \times 5 \mu\text{m}^2$). Continuous imaging was conducted over an imaging area of $3 \times 3 \mu\text{m}^2$. (c) and (d) show the first and last of the continuous imaging series, which correspond to the area enclosed by the dotted green rectangles in (a) and (b) respectively. The green circle indicates the common features observed on all four images. No significant changes were observed throughout the imaged area.

small part of the imaged area (circled in blue) (Figure 5.6). No changes were detected at all in the imaged TP surface (Figure 5.7), suggesting that ASA and TP are much less likely to undergo sublimation.

The tip influence on the surfaces was determined by comparing the repeatedly imaged region and its surrounding area. On the AN surface, new tall features mainly emerged within the repeatedly imaged region, whereas less features emerged in the surrounding areas. Therefore, it is possible that there might be some degree of tip influence that promoted the surface photoreactivity of AN. For SA, ASA, and TP, there were no significant differences between the two regions, indicating insignificant tip influence on the studied surfaces.

5.2.1 Preventing and determining the influence of the tip on areas imaged by AFM

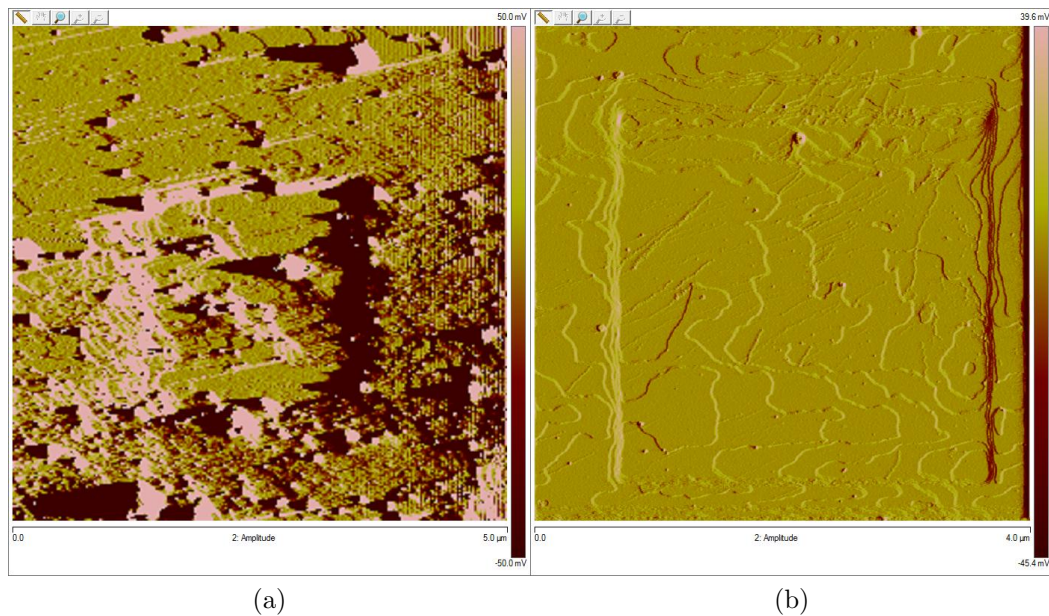


Figure 5.8: Representative AFM amplitude image of (a) SA (011) ($5 \times 5 \mu\text{m}^2$), and (b) AN (001) ($4 \times 4 \mu\text{m}^2$). The middle areas in both images were repeatedly imaged several times prior to recording these images, which indicate significant tip influence causing the formation of “frame” features.

In order to minimize any tip influence on the area of imaging, the tip-to-sample force was always minimized such that the tip was just close enough to the sample to trace the surface properly. However, despite the best efforts to eliminate tip influence, this did not always guarantee success, particularly for long periods of continuous imaging periods. Two examples are given in Figure 5.8, which show significant differences between the repeatedly imaged middle region and its surrounding area. As the degree of tip influence on the surface

was found to be rather unpredictable, an image of a larger area was always recorded at the end of a continuous imaging study, in order to verify if any distinctive “frame” features were observed, which would indicate significant tip influence.

5.3 Predicting surface sublimation

Material	ΔH_{sub}^{298K} [kJ mol ⁻¹]
Salicylic acid	99 ± 2
Anthracene	104.5 ± 1.5
Aspirin	109.7 ± 0.5
Theophylline	142 ± 0.3

Table 5.1: Sublimation enthalpy of selected organic crystals. From references [181–183].

In attempt to predict the likelihood of surface sublimation of different organic crystals, the sublimation enthalpy was considered (Table 5.1) [181–183]. Based on the study in the previous section, a correlation could be drawn between the degree of step rearrangement observed at the surface of each crystal and the corresponding sublimation enthalpy of the material. The lower the sublimation enthalpy, the more sublimation of molecules is expected, therefore, more significant step rearrangement is expected.

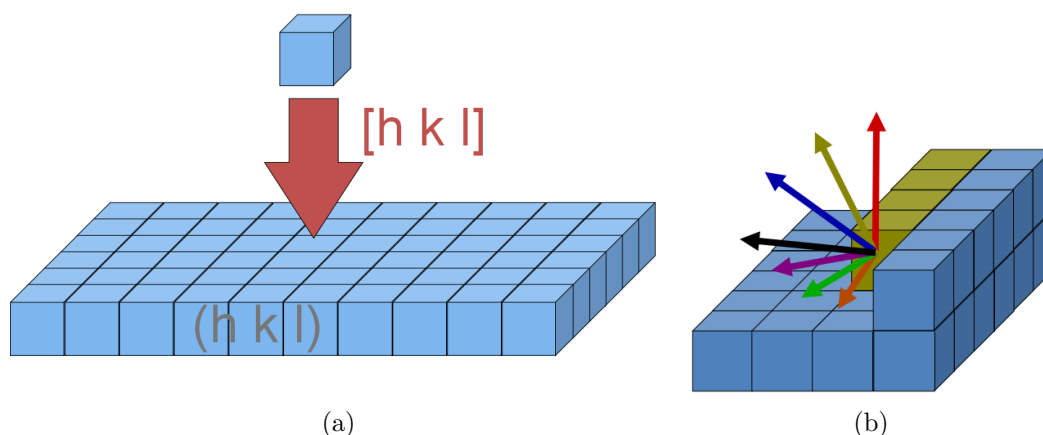


Figure 5.9: (a) Schematic illustration of the 2-D nucleation energy model (developed by Dinesh-Ramesh Mirpuri Vatvani). The model assumes that the growth rate of a certain crystal face is directly proportional to the energy released when one molecule is added to that crystal face; (b) Schematic illustration of the sublimation of molecules at step edges and kinks (dark yellow blocks). The arrows in different colours indicate the possible directions of the molecule leaving the surface.

Despite good agreement between the sublimation enthalpy and experimental observations, sublimation enthalpy is a bulk property. In an effort to improve the agreement, face specific energy calculations were also considered. These calculations were based on a morphology prediction model developed by Dinesh-Ramesh Mirpuri Vatvani [184], together with the use of the UNI forcefield [185, 186]. A schematic illustration of this model is shown in Figure 5.9(a). It assumes that the rate of growth of a certain crystal face is directly proportional to the energy released upon the binding of the first molecule onto a perfectly flat surface of this face.

As the sublimation of surface molecules is simply the reverse of the binding of molecules onto the surface, it is possible that the tendency for a molecule to sublime is related to the energy calculations obtained from this morphology prediction model. However, while the model calculates the energy of one molecule binding or leaving a perfectly flat surface, this is not likely the same as the energy of molecules binding or leaving a step or kink site. Yet amongst other models, this was found to be the model that relates closest to the study of surface sublimation observed by AFM.

In an attempt to model the surface sublimation of molecules at the step, the following assumptions were made:

1. There are several possible directions that the molecule at the step can follow while leaving the surface (Figure 5.9(b)).
2. The energy required for the molecules leaving the step along a specific trajectory $[h_n k_n l_n]$ equates to the negative of the binding energy of the corresponding $(h_n k_n l_n)$ face calculated using the 2-D morphology prediction model.
3. The molecules at the steps can escape via any direction away from the surface, but preferentially along directions that have smaller binding energy (in terms of magnitude).

For each crystal, the binding energies of all (hkl) planes were calculated, where h, k, and l are integers that ranged from -4 to +4. It is hereby noted that these binding energy calculations were performed by Dinesh-Ramesh Mirpuri Vatvani. The calculated energies were ranked and combined into a histogram for each crystal, which showed the number of faces with energy falling into bin sizes of 5 kJmol^{-1} .

The resultant histograms are shown in Figure 5.10. The binding energy of the face of each material that was studied by AFM is circled in black in

Binding energy distribution based on the 2-D nucleation model

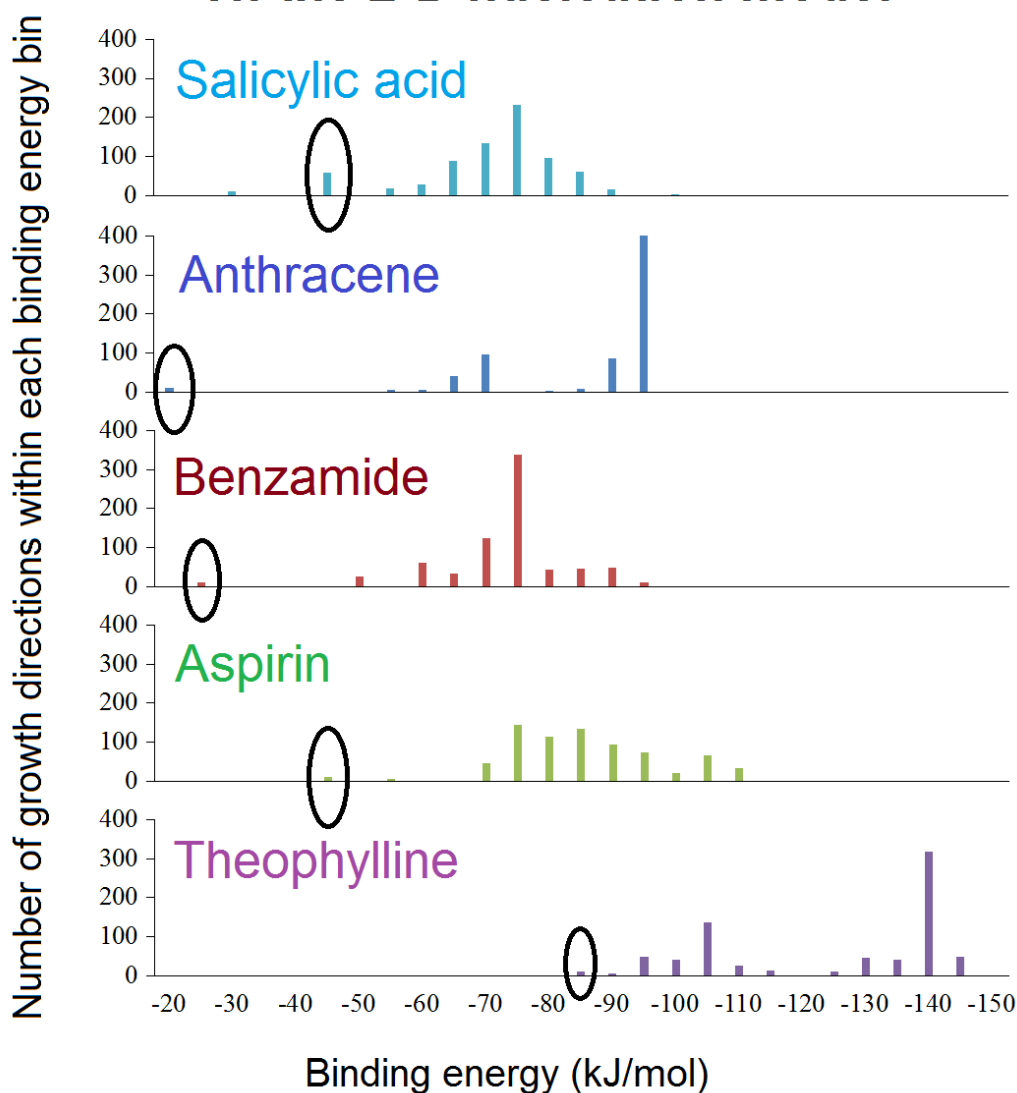


Figure 5.10: Histograms of the binding energy calculations for each material based on the 2-D nucleation morphology prediction model. The bins circled in black on the histogram of each crystal correspond to the dominant face that was studied by AFM.

each histogram. These values do not show much correlation to the degree of surface rearrangement observed experimentally for each material. AN (001) had the smallest binding energy but the step movements on this surface was less significant than that observed on SA (011). SA (011) and ASA (100) had similar binding energies, but the former surface underwent much more significant rearrangement, while the latter surface hardly changed.

Even when all the calculated binding energies are taken into account, the range of binding energies found for ASA, SA, and AN are relatively similar. While the distribution of binding energies for each crystal was different, it is

hard to determine how this affects the sublimation behaviour observed on each crystal surface. However, it is clear that the binding energies calculated for TP are significantly larger in magnitude than the other four materials, which seems to agree with the experimental observation that no step movement occurred on the TP (002) surface.

Although this model does not show strong indication of the tendency of sublimation on the surface of different materials, it highlights the complexity of the sublimation of molecules at the surface, which is not addressed by sublimation enthalpy values. Despite the fact that the sublimation enthalpy values agree well with the experimental observation of sublimation on the surface of crystals, it should only be used as a rough guide to whether or not sublimation is expected on the surface when imaged by AFM.

5.4 Chapter conclusion

Based on the results from this chapter, the following conclusions were established:

1. The step rearrangement observed on selected organic crystal surfaces can be caused by the sublimation of molecules on the surface.
2. The likelihood of the sublimation of molecules on the surface imaged by AFM roughly varies according to the sublimation enthalpy value of the crystal.
3. As the tip influence on the imaged area is sometimes unpredictable, it is important to verify whether the tip altered the surface after continuous imaging. This can be done by imaging a larger area and compare the repeatedly imaged region and its surrounding area.

By acknowledging the possibility of surface sublimation on organic crystal surfaces, and determining changes caused by the AFM tip, this establishes an important foundation for the upcoming results chapters, in order to allow a more accurate interpretation of the surface response detected by AFM imaging.

Chapter 6

Surface study of the solid-state hydrolysis of aspirin (ASA)

6.1 Introduction

In Chapter 3, the bulk studies of aspirin (ASA) hydrolysis was reviewed, and the importance of studying isolated crystal surfaces was highlighted, given the anisotropic nature of ASA crystal surfaces. In this chapter, a study of solid-state ASA hydrolysis by AFM is presented, and a surface reaction mechanism is proposed based on the findings.

6.2 Selecting a suitable ASA crystal surface

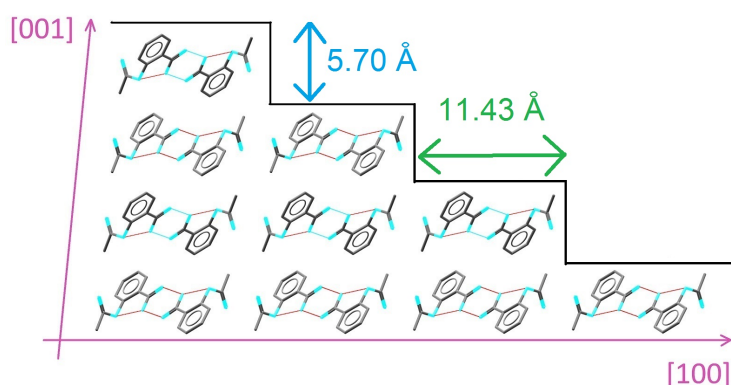


Figure 6.1: Crystal structure of aspirin (ASA) form I viewed along the $[010]$ direction. Steps of around 5.7 \AA are expected to be observed on the (001) surface, corresponding to one molecule thick, while steps of roughly around 11.4 \AA are expected to be observed on the (100) surface, corresponding to the thickness of one pair of ASA molecules.

The crystal structure of ASA form I is shown in Figure 6.1 (CSD code ACSALA01) [168]. The unit cell parameters are as follow:

- $a = 11.43 \text{ \AA}$, $b = 6.59 \text{ \AA}$, $c = 11.40 \text{ \AA}$
- $\alpha = 90^\circ$, $\beta = 95.68^\circ$, $\gamma = 90^\circ$
- Space group: $P 2_1/c$; Unit cell volume = 854.2 \AA^3

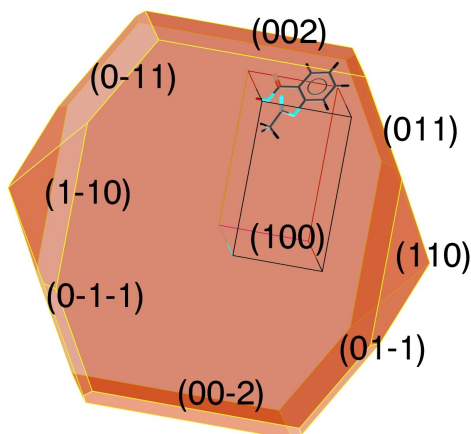


Figure 6.2: The BFDH morphology prediction of ASA form I crystals

The most suitable surfaces for AFM study are ones that are flat at the molecular scale and contain steps of few molecular layers thick. In selecting the best method to prepare ASA crystals for this study, a method that produced consistent quantity of suitable crystal surfaces was required. The BFDH morphology model prediction of ASA form I is shown in Figure 6.2, which predicts $\{100\}$ and $\{001\}$ to be the most dominant faces of crystal growth. Based on the crystal structure, these two faces are potentially good cleavage planes that can produce a surface that is flat at the molecular scale, which is ideal for AFM studies.

The following methods of crystal preparation were tested:

1. Crystal growth by sublimation
2. Quick evaporation of a saturated solvent
3. Slow solution crystal growth

For all of the methods above, the starting material, ASA, was sourced from Sigma Aldrich (research grade). 1-D XRD patterns were recorded for each sample (Figure 6.3) to identify the orientation of the crystals prepared on the coverslips. Each sample was also ground for a PXRD to be recorded, which matched the simulated powder pattern of ASA.

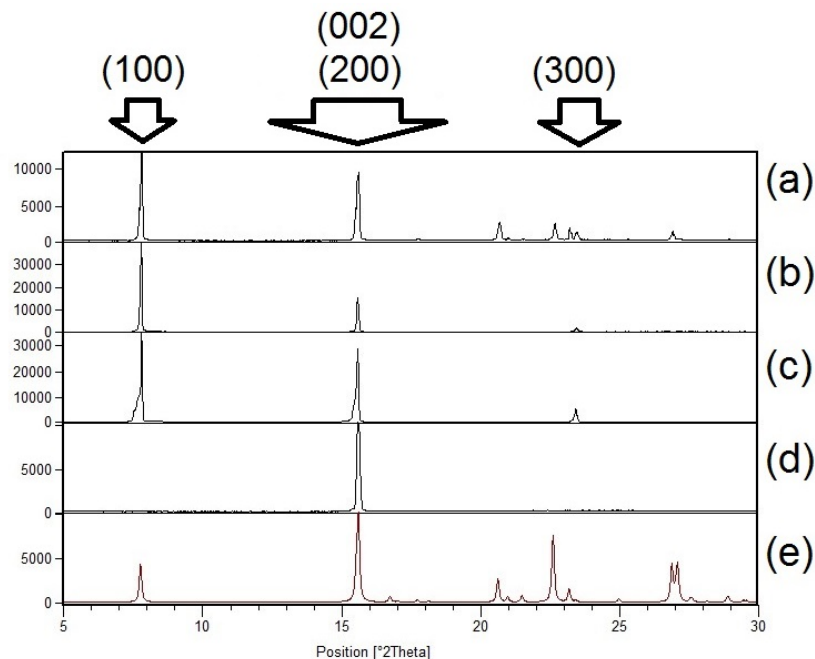


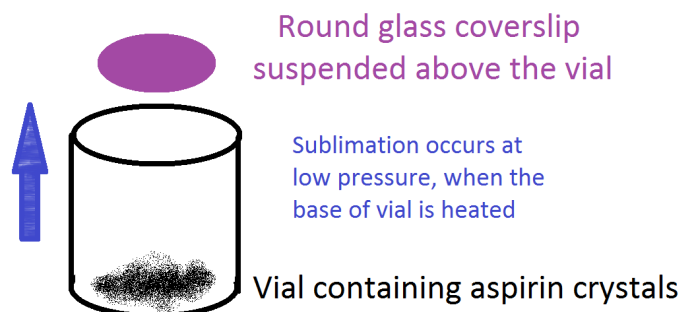
Figure 6.3: 1-D XRD scans of ASA crystals grown by (a) sublimation; (b) quick evaporation of a solution of ASA saturated in toluene; (c) slow solution crystallisation from acetone or ether, where the pattern was recorded about the dominant face; (d) slow solution crystallisation in acetone, where the XRD was recorded on a crystal face cleaved along (002); (e) simulated powder pattern of ASA form I. The arrows indicate the face of the d-spacings that gives rise to the intensity at certain 2θ values. Each sample was also ground for a PXRD to be recorded (not shown), which matched the simulated ASA pattern.

6.2.1 Sublimation growth

A 2 dram vial that contained approximately 1 g of ASA powder was placed in a freeze dryer (Figure 6.4(a)), with a glass coverslip suspended on top of the vial. The freeze drier was set to approximately 1500 μ bar, while the base of the vial was heated to 80°C. As the crystals sublimed, crystallisation occurred on the walls of the vials as well as on the suspended coverslip (Figure 6.4(b)).

Compared to the simulated powder pattern (Figure 6.3(e)), The 1-D XRD of the product formed on the coverslip showed a stronger intensity at around $2\theta = 7.8^\circ$ (Figure 6.3(a)), which corresponded to the $d_{\{100\}}$ spacing. However, as other reflections were also observed, there was no specific orientation of the crystals on the coverslips that could be detected. There was also a mixture of morphologies, with both hexagonal as well as rectangular crystals (Figure 6.4(c) and (d)). Based on the morphology prediction, the top hexagonal face of the crystal in Figure 6.4(c) was expected to be the dominant $\{100\}$ face, and was selected to be imaged by AFM.

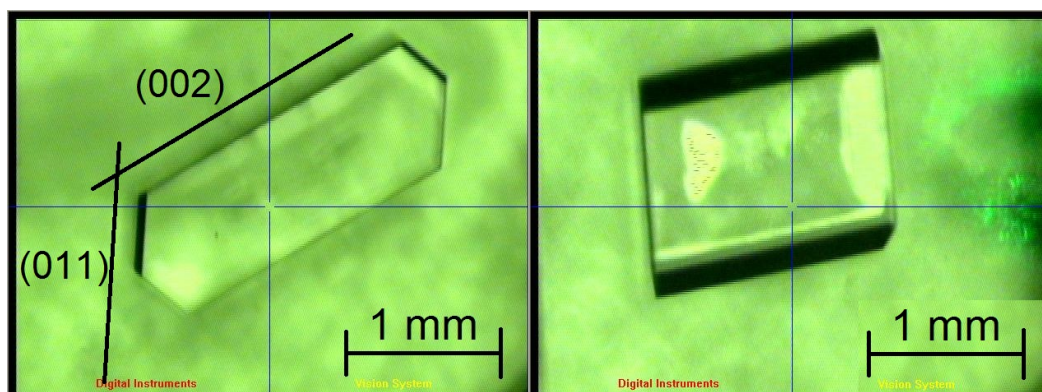
A representative AFM height profile is shown in Figure 6.5. The main features observed on the surface were monomolecular steps, where many of these steps were aligned along the (001) face. The step heights measured approxi-



(a)



(b)



(c)

(d)

Figure 6.4: (a) Schematic illustration of ASA crystal growth by sublimation; (b) Photo of the resulting ASA crystals; (c, d) Optical microscope images showing examples of ASA crystals grown from the vapour with different morphologies.

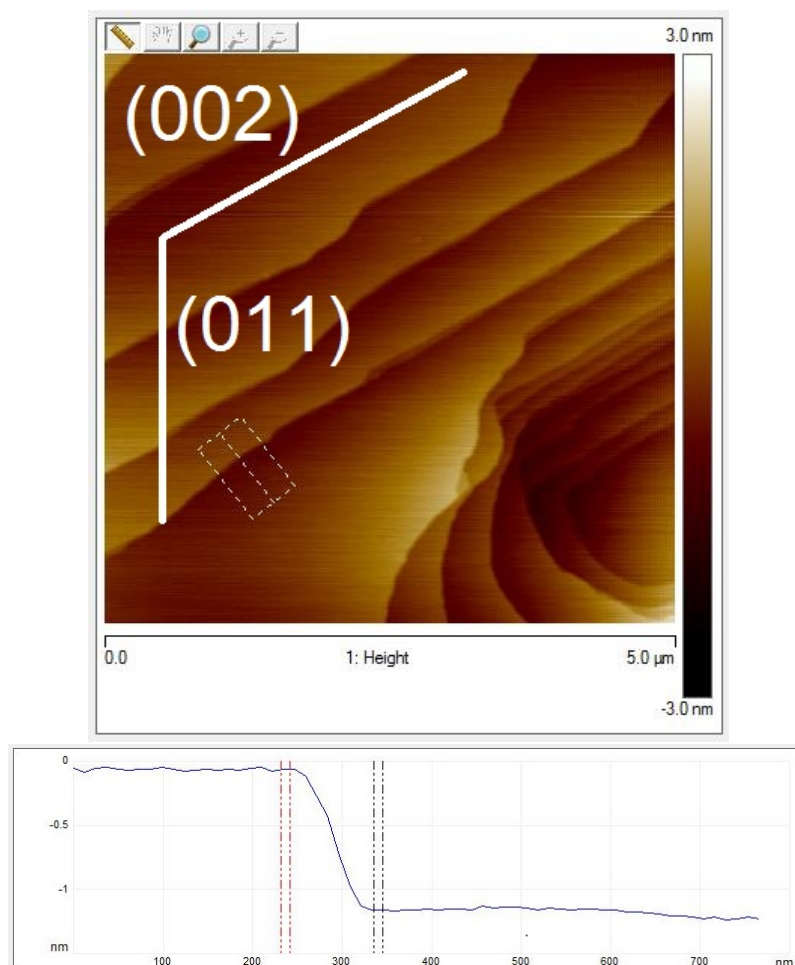


Figure 6.5: Representative AFM height profile of an ASA $\{100\}$ crystal surface grown by sublimation ($5 \times 5 \mu\text{m}^2$). The plot below is a cross section of the average height taken across the step enclosed by the broken lines in the image, which measures the step height to be 11 \AA .

mately $11 \pm 0.3 \text{ \AA}$, which matched the step height predicted in Figure 6.1 and confirmed that the step thickness is equivalent to one pair of ASA molecules.

Although crystals prepared by sublimation were desirable as there are no solvent effects introduced during growth, crystals prepared by this method were not selected for the hydrolysis studies. The main reason was the lack of control of where crystals formed, and very often crystallisation occurred only on the walls of the vials but not on the coverslips.

6.2.2 Fast evaporation of a saturated solvent

ASA was dissolved in toluene at room temperature (approximately 20°C) until the solution was saturated. A drop of the formed solution was added onto a glass coverslip and left to evaporate, which took less than one minute. ASA crystals of approximately 10 to $30 \mu\text{m}$ in length were formed (Figure 6.6(a)).

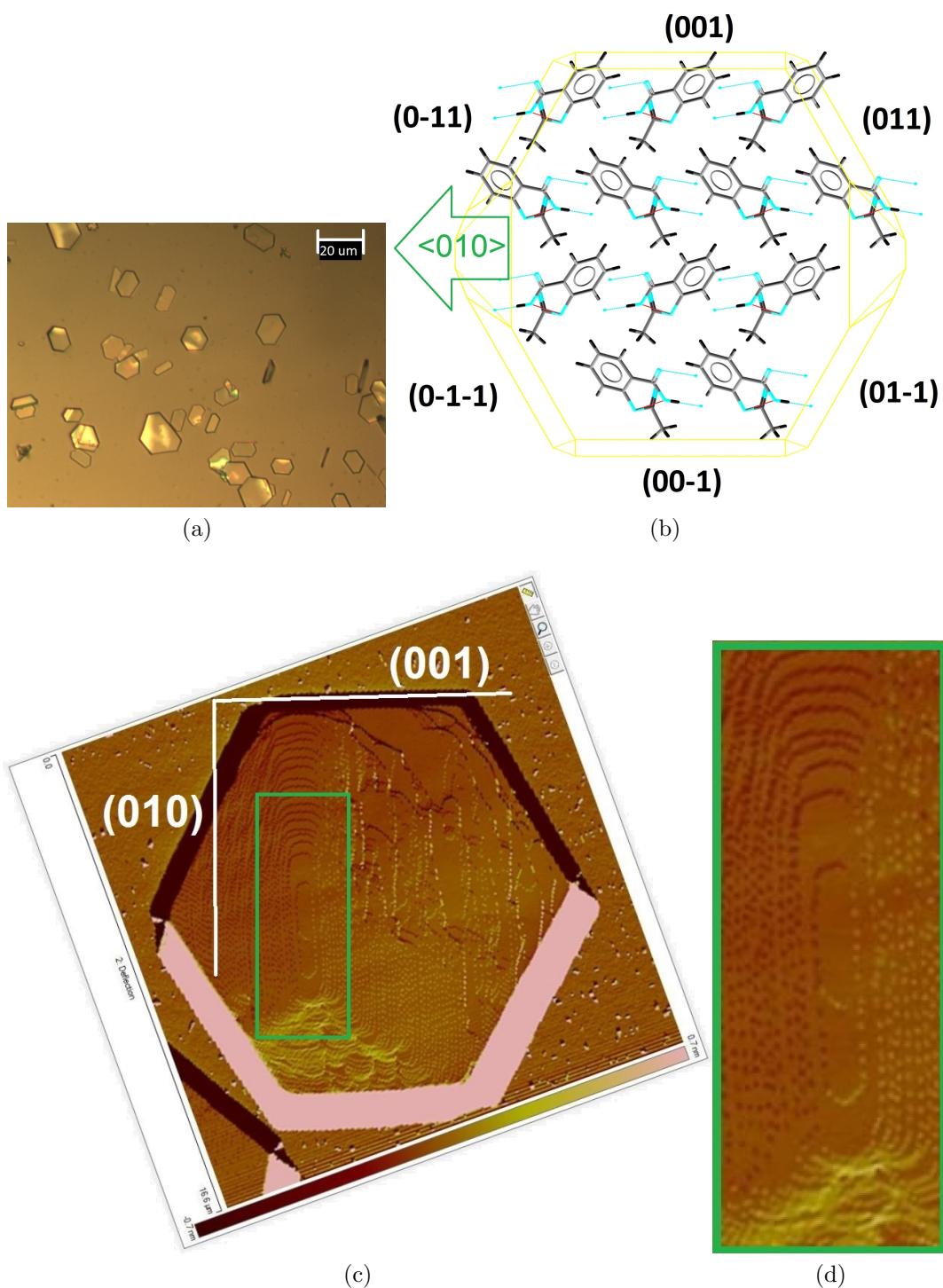


Figure 6.6: (a) Optical microscope image of ASA crystals prepared by rapid evaporation; (b) Crystal structure of ASA viewed along the $[100]$ direction, together with the predicted morphology (in yellow), showing the hydrogen bonding pattern running horizontally along $\langle 010 \rangle$; (c) Representative AFM amplitude profiles ($16.6 \times 16.6 \mu\text{m}^2$) of an ASA (100) surface formed by quick evaporation, rotated to match the orientation of the crystal structure in (b); (d) closeup image of a screw dislocation, enclosed by the green rectangle area in (c). The average step density along $[010]$ and $[001]$ near the screw dislocation were measured to be $0.1 \mu\text{m}/\text{step}$ and $0.3 \mu\text{m}/\text{step}$ respectively. The step height measured was 11 \AA , which corresponds to the length of one pair of ASA molecules along $[100]$.

Most crystals had a hexagonal morphology, which matched the BFDH prediction (Figure 6.6(b)). The 1-D XRD pattern recorded contained reflections corresponding to $d_{(100)}$, $d_{(200)}$, and $d_{(300)}$ (Figure 6.3(b)), confirming that $\{100\}$ was the main exposed face (same as for the crystals grown from vapour).

A representative AFM image of the crystal surface is shown in Figure 6.6(c, d), where a screw dislocation was observed. Hillocks were formed during crystal growth, with steps of around 11 Å in height, corresponding to one pair of ASA dimer in length along the $[100]$ direction (Figure 6.1). The orientation and shape of the screw dislocation indicates a strong difference in growth rates along the $[010]$ and $[001]$ directions. The average step density along $[010]$ and $[001]$ were both measured across 10 steps, and were found to be 0.1 $\mu\text{m}/\text{step}$ and 0.3 $\mu\text{m}/\text{step}$ respectively, indicating that the rate of crystal growth along $[001]$ was 3 times faster than that along $[010]$.

6.2.3 Slow solution growth

Two grams of ASA was dissolved in approximately 20 ml of acetone and the resulting solution was split into several 2 or 4 dram vials. The vials were covered with plastic lids that contained 3 or 4 holes pierced by a needle, and the solutions were left to evaporate slowly at room temperature over one or two weeks. For some crystallisation setups, 40 ml of ether was used instead of acetone, which produced similar results.

The crystals formed were all of mixed morphology and sizes, ranging from millimetres to over one centimetre (Figure 6.7(a) to (c)). A rectangular crystal was initially selected to be studied by the AFM, and the largest crystal face was confirmed by 1-D XRD to be $\{100\}$ (Figure 6.3(c)). The crystal was mounted on to the AFM with $\{100\}$ on top (Figure 6.7(d)). A representative AFM image of the surface shows that the surface is much rougher than the previous surfaces studied (Figure 6.8). No molecular step features were present, and some trench features were observed running approximately along the vertical direction of the image. The cross sectional height profile was used to measure the depth of these trenches, which varied from a few nm to over 10 nm.

Cleaved ASA crystal surfaces

In order to obtain a flatter surface, the crystals grown in solution were cleaved. Several long cylindrical crystals with a hexagonal cross section morphology were selected, which were easily cleaved along the hexagonal cross section with a razor blade (Figure 6.9(a)).



(a)



(b)

(c)

(d)

Figure 6.7: ASA Crystals of mixed morphologies grown from solution (a - c); A large ASA crystal mounted on the AFM for imaging, with (100) facing the top (d).

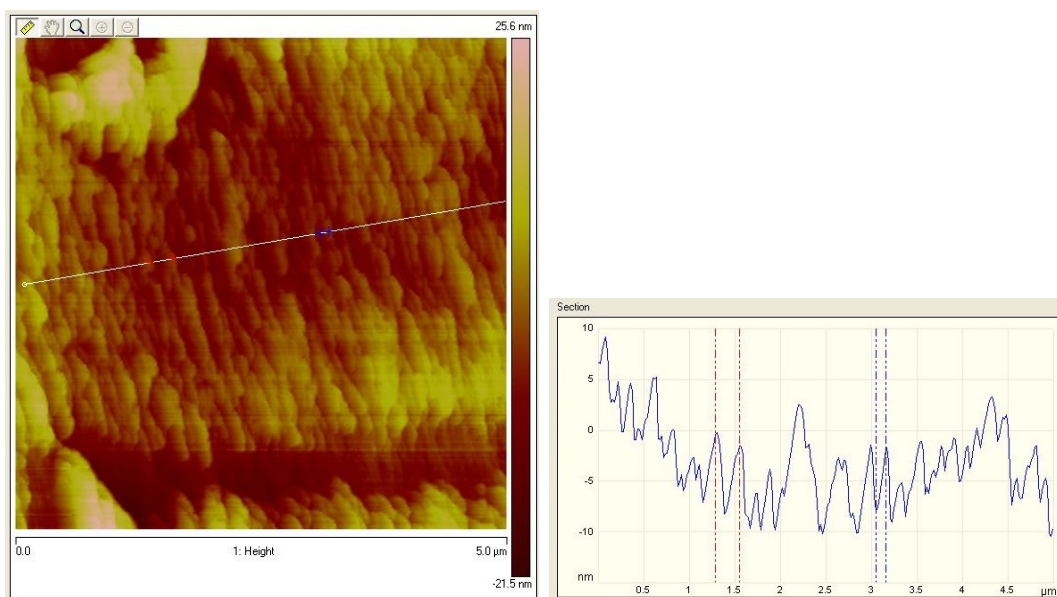
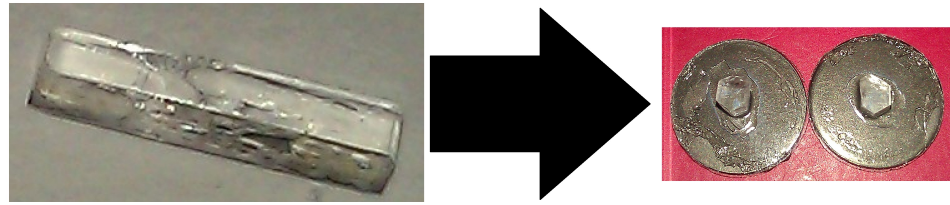
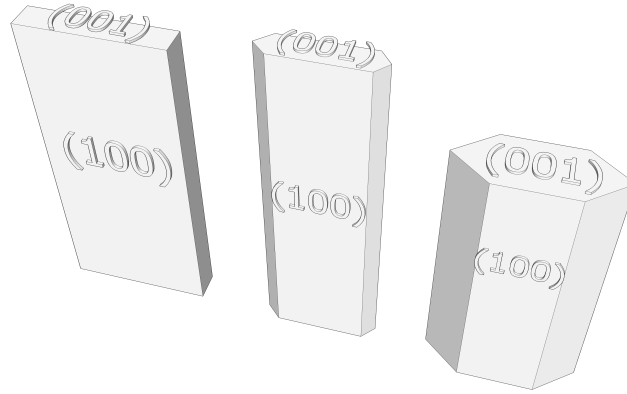


Figure 6.8: Left: a representative AFM height image of the ASA (100) surface ($5 \times 5 \mu\text{m}^2$). Right: the cross sectional height along the white line in the image. The crystal was prepared by slow solution growth in ether.

As the cross sectional area was hexagonal in shape, it was thought that this was the $\{100\}$ cleavage plane. However, the 1-D XRD on this face revealed that this was in fact the $\{001\}$ due to the systematic absence of $\{001\}$ from



(a)



(b)

Figure 6.9: (a) Preparation of ASA {001} face for AFM imaging by cleaving long ASA crystals along the cross sectional area; (b) Schematic illustration of some morphologies of ASA crystals that were obtained experimentally.

the pattern (Figure 6.3(d)). The {100} face of these crystals was instead along the length of each crystal (Figure 6.9(b)).

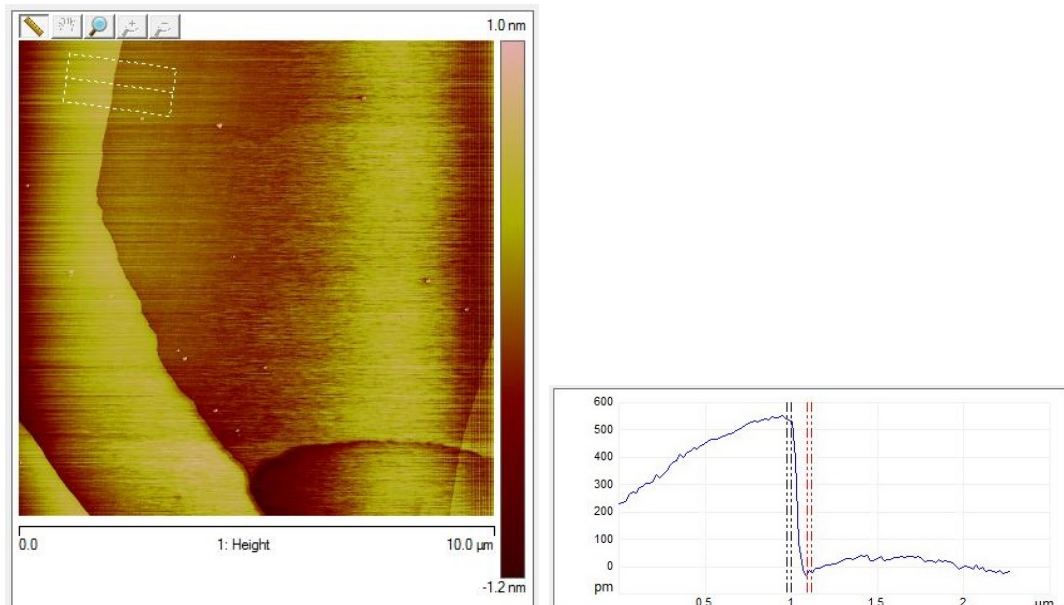


Figure 6.10: A representative AFM height image of a cleaved {001} surface (left) ($10 \times 10 \mu\text{m}^2$). The plot on the right is a cross section of the average height taken across the step enclosed by the broken lines in the image, which measures the step height to be 5.5 \AA .

The cleaved {001} face was studied by AFM, a representative image is

shown in Figure 6.10. The main features that were observed are steps, which were measured to be 5.4 ± 0.2 Å in height, matching the thickness of one molecule of ASA along the {001} direction (Figure 6.1). Other areas on the fresh surface were also sampled, which showed similar step features of the same height.

In summary of the methods to prepare ASA surfaces for AFM, the {100} face can be obtained by sublimation growth, fast evaporation growth, as well as slow solution growth. The {001} face can be obtained by slow solution growth, which can be cleaved to expose a surface that is flat at the molecular scale.

Out of all the surfaces studied so far, the cleaved {001} was found to be the best to be used for the hydrolysis studies due to the following reasons:

1. The long crystals could be reproduced easily, and each one could be split into many segments to give rise to several fresh {001} surface by cutting along the length of the crystal.
2. The cleaved surface was the flattest amongst all others, containing only few monomolecular steps. Crystals prepared by sublimation and quick evaporation were too small to be handled with tweezers, and it was only possible to cleave big crystals grown from solution. This was the closest to a “perfect” crystal surface that could be obtained experimentally.

Although these long crystals did not match the morphology as predicted by BFDH, the production of such crystal morphology was quite consistent for the same source of ASA used for this study. It is unclear what gives rise to ASA crystals of such morphology, which might be due to the impurity in the sample or solvent affecting the crystal growth on different faces. However, this is another research topic which is not further pursued in this thesis, and the cleaved {001} was selected as the model surface for the hydrolysis study for the rest of this chapter. Reference to Figure 6.1 gives an idea of the arrangement of ASA molecules with regard to this plane.

6.3 Following surfaces of ageing ASA crystal {001} face in different moisture levels

Cleaved ASA {001} surfaces were prepared and aged in the each of the following conditions for 2 months (60 days):

1. 0% relative humidity (RH)

2. 50% RH
3. room humidity (*ca.* 40% RH)
4. 98% RH
5. toluene atmosphere

In order to prevent any effects of different solvents on the surface and morphology of the crystals produced, only crystals recrystallised from acetone were selected for this study. All of the chambers that held the samples were left in the same room, so every sample experienced the same fluctuation in temperature over the aging period. The surface aged under room conditions also experienced a fluctuation in RH level (between 30% RH and 60% RH), while other samples were left in different controlled RH environments (the setup of such environments is described in Chapter 4). The sample aged in a toluene atmosphere was studied as well to observe the response of the surface exposed to an organic vapour instead of moisture.

For this study, continuous imaging could not be applied. As the rate of degradation obtained by bulk studies in the past were shown to be very slow even at elevated temperature, the rate at room temperature is expected to be even slower. Thus the aging period was set to be 2 months in hope that there would be significant changes on the studied surfaces before and after aging, which was not a reasonable timescale for continuous imaging. Therefore, only non-continuous imaging was applied to study these samples.

Four areas ($5 \times 5 \mu\text{m}^2$) were imaged for each crystal before aging. Monomolecular step features observed on these imaged areas were found to be $5.4 \pm 0.2 \text{ \AA}$ in height (Figure 6.11). This measurement was based on the average height and standard deviation of a total of 20 steps from all freshly cleaved surfaces, which indicated that the step height was quite consistent. As it was not possible to return to the same areas that were imaged before aging, four areas of the same size ($5 \times 5 \mu\text{m}^2$) were chosen at random to be imaged for each sample after aging. The images obtained before and after aging were compared to identify the changes on the surface exposed to different conditions.

To ensure that the observed surface changes corresponding to different environments are reproducible and significant, at least two crystals were studied for each environment. All the surfaces studied under the same condition exhibited similar features that are described in the following sections.

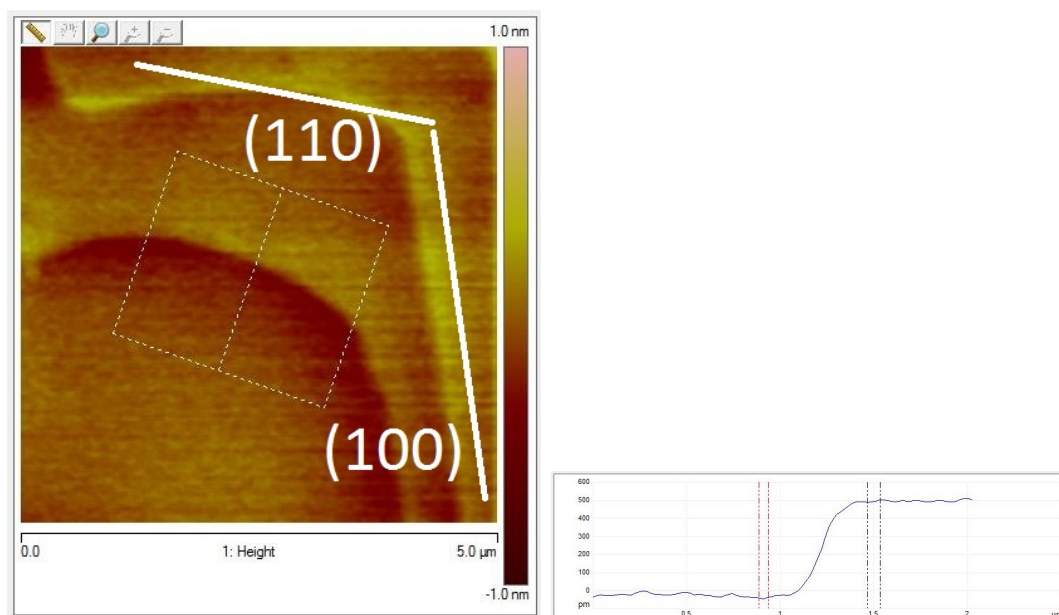


Figure 6.11: A representative AFM height image of a cleaved $\{001\}$ surface (left) ($5 \times 5 \mu\text{m}^2$). The orientation of (100) and (110) faces are indicated by the white lines. The plot on the right is a cross section of the average height taken across the step enclosed by the broken lines in the image, which measures the step height to be 5.4 \AA .

6.3.1 0% RH

The AFM images of the crystal surface after two months in 0% RH showed no significant changes (Figure 6.12). Apart from the step features corresponding to one or two molecules thick (also observed on the fresh surfaces before ageing), the rest of the surface was flat at the molecular scale. To consider even further storage effects, the surface after 4 months in 0% RH showed no changes, which suggested that in the absence of moisture, no reaction is expected on the surface, and the surface remains stable.

6.3.2 Room humidity (*ca.* 40% RH)

For the crystal left in room conditions for over two months, the surface showed significant changes (Figure 6.13). Several tall surface features were observed, which ranged from 200 \AA to over 1000 \AA in height. Few steps of one or two molecules thick (5.4 and 11 \AA) were still present, but most of the steps observed were over 100 \AA in height aligned to (100) and (110), which might have aggregated from the original monomolecular steps (known as step bunching). Most of the tall features observed were located at the edges and corners of these macrosteps.

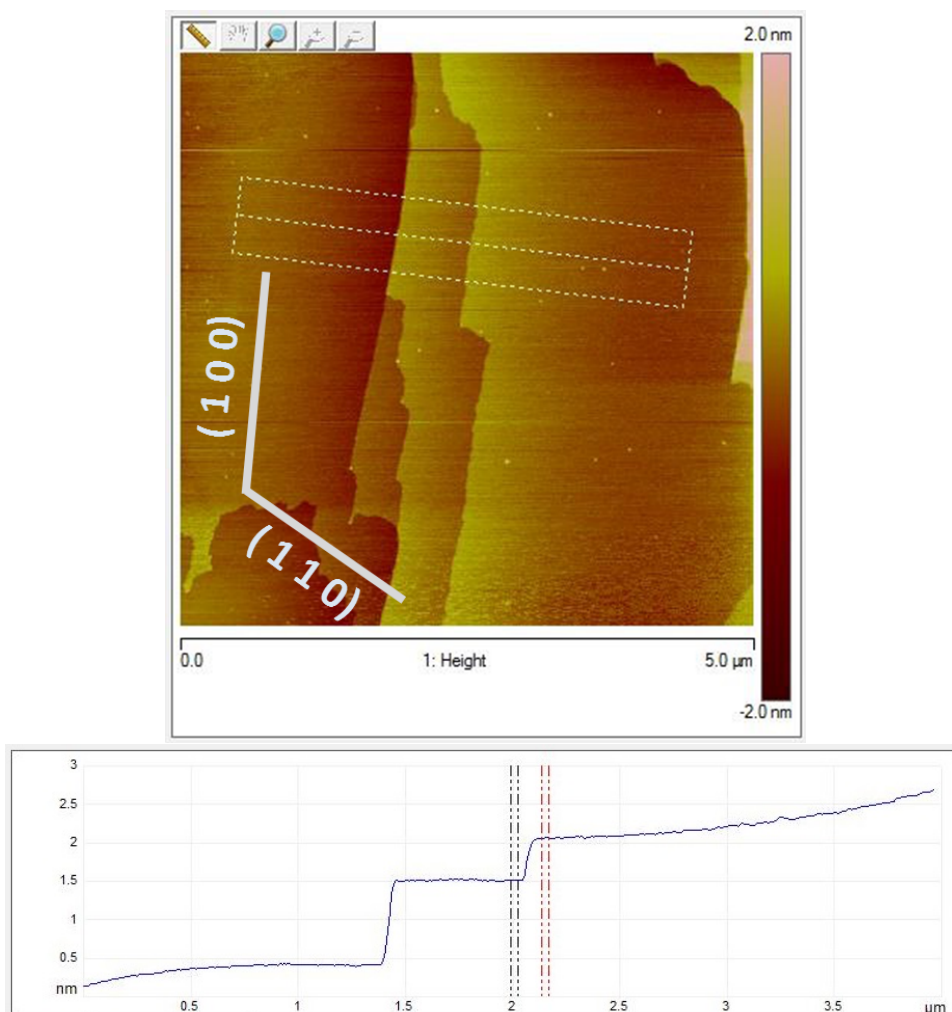


Figure 6.12: A representative AFM image of an ASA surface aged in 0% RH for two months ($5 \times 5 \mu\text{m}^2$). The orientation of (100) and (110) faces are indicated by the white lines. The plot below is a cross section of the average height taken across the steps enclosed by the broken lines in the image, which measures the step height to be 5.4 and 11 Å. This corresponds to the length of one and two ASA molecules thick along [001] respectively.

6.3.3 50% RH

The surface aged in 50% RH was similar to the sample aged in room humidity (Figure 6.14). This was as expected because both samples experienced similar level of RH, only that the room condition had a bigger RH fluctuation. The height of tall features on the surface ranged from 300 to over 2000 Å in height, while macrosteps of over 50 Å were measured. Again, most of the tall features were situated along the edges and corners of these macrosteps, where the macrosteps were aligned to the (100) and (110) faces.

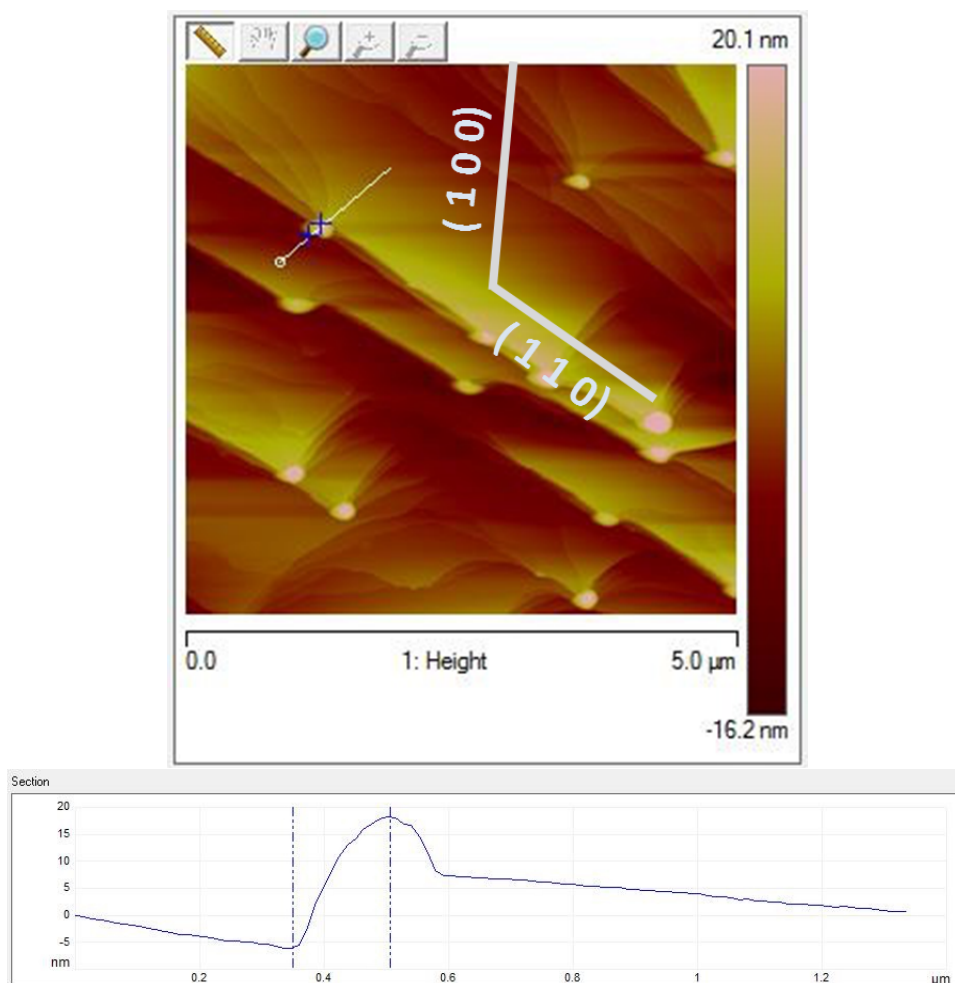


Figure 6.13: A representative AFM image of an ASA surface aged at room humidity for two months ($5 \times 5 \mu\text{m}^2$). The orientation of (100) and (110) faces are indicated by the thick white lines, where in this image steps mainly aligned to (110). The cross sectional height of the thin white line in the image is shown below. A tall surface feature was measured to be over 220 \AA in height from the base of the lower terrace, while the macrostep step aligned to (110) was measured to be 130 \AA in height.

6.3.4 98% RH

Surprisingly, the sample aged at 98% RH did not show any formation of tall features on the surface. The two images in Figure 6.15 appear to be very different. The first image shows irregular step edges and “islands” of thickness ranging from 10 to 30 \AA , while the steps in the second image have straighter edges and are more aligned to the (100) face, which resembles that of the surface stored in 0% RH. The height of the step features (both macrosteps and microsteps) ranged from 6 \AA to over 50 \AA in height. The height of ten monomolecular steps were measured, and the average height (and standard deviation) was $6 \pm 0.5 \text{ \AA}$. Compared to the monomolecular step heights measured on the fresh crystal surface ($5.4 \pm 0.2 \text{ \AA}$), the steps observed on the surface stored in 98% RH had a greater average height, but the higher standard deviation indicated that these

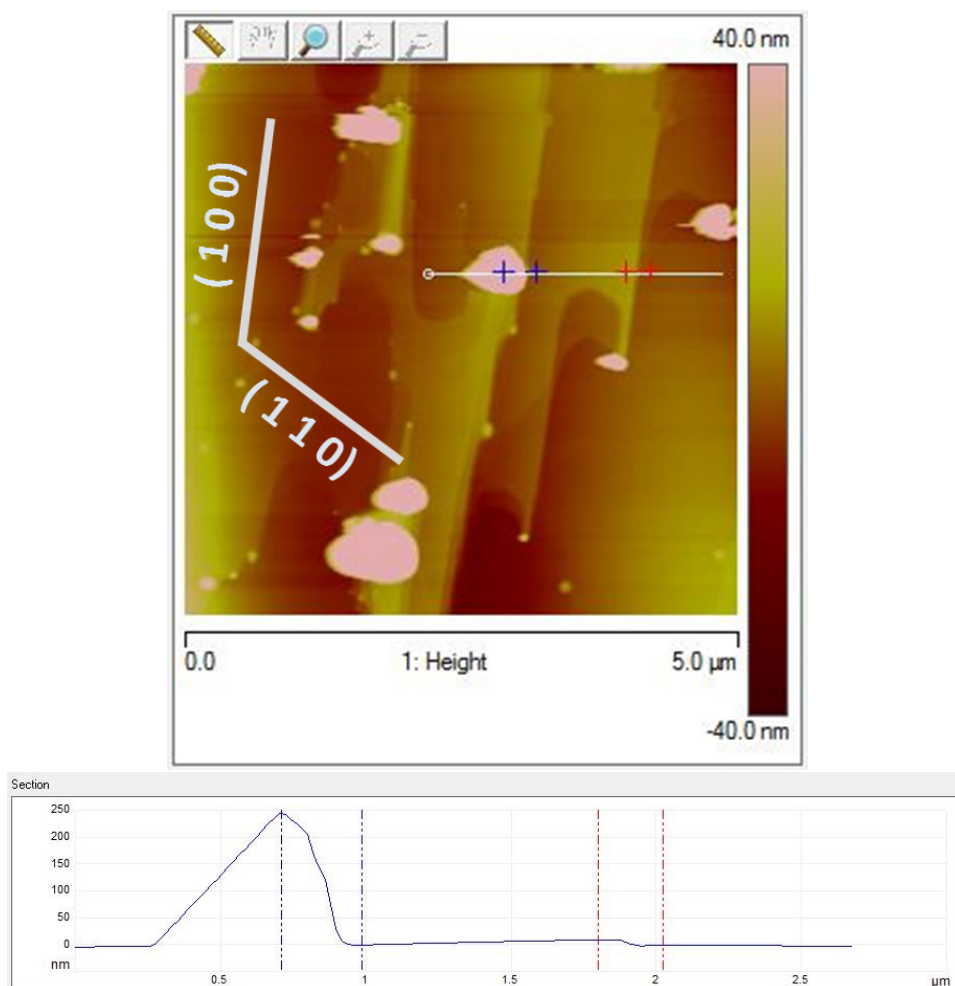


Figure 6.14: A representative AFM image of an ASA surface aged at 50% RH for two months ($5 \times 5 \mu\text{m}^2$). The orientation of (100) and (110) faces are indicated by the thick white lines. For this image the steps were aligned to (100). The cross sectional height of the white line in the image is shown below, which measures a tall surface feature to be over 2400 Å in height (blue), and a step feature of 110 Å (red).

values were more dispersed. As a change in step height would suggest a change in chemical composition on the surface, it is possible that a new species has formed. This might be salicylic acid (SA), as under such conditions, hydrolysis of ASA is likely to occur.

6.3.5 Toluene atmosphere

Tall features were observed on the surface aged in toluene atmosphere for 2 months (Figure 6.16). The height distribution measured was disperse, ranging from 70 to over 400 Å. The surface also contained step features of one or two molecules thick (5.4 and 11 Å), which were similar to those of the fresh surface.

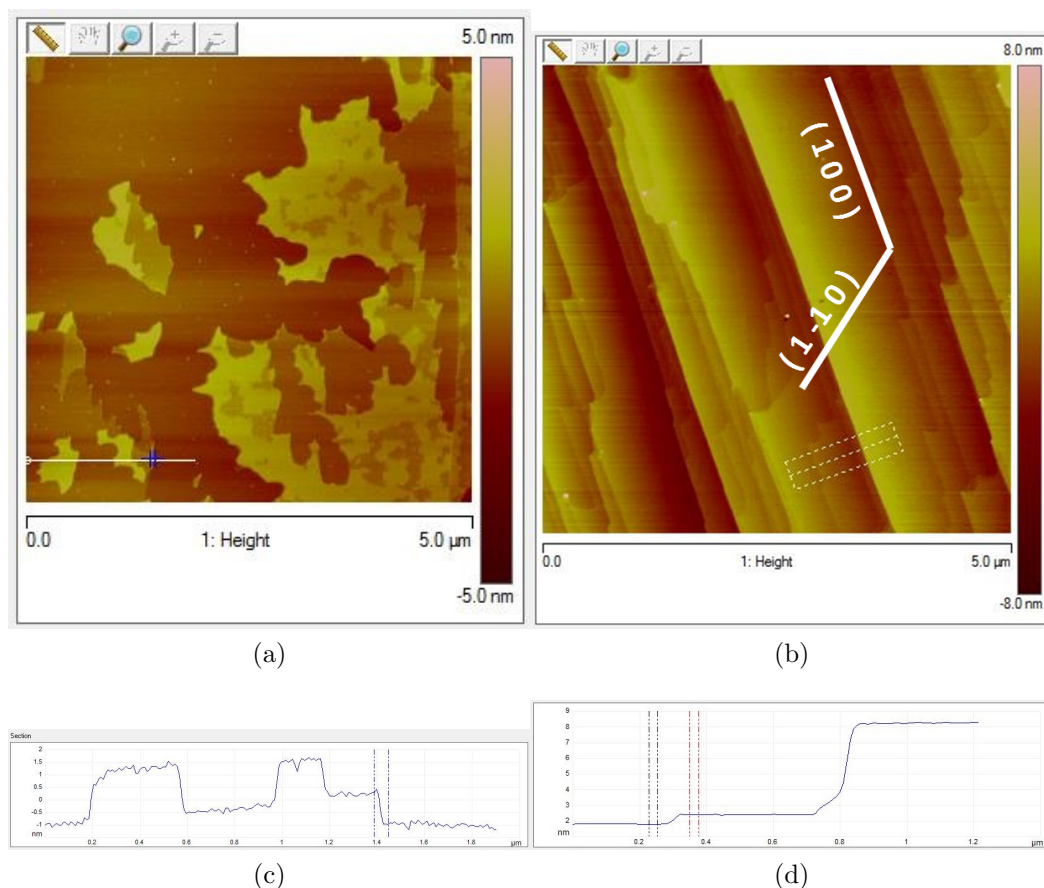


Figure 6.15: (a) and (b) Two representative AFM images of an ASA surface aged at 98% RH for two months ($5 \times 5 \mu\text{m}^2$). The orientation of (100) and (1-10) faces for both images are indicated by the thick white lines; (c) The cross sectional height of the white line in (a). The blue markers across a step feature measures the step height to be 12.6 \AA ; (d) The average cross section taken across the steps enclosed by the broken lines in (b), showing a small step and a macrostep of 6.3 and 58 \AA in height respectively.

6.4 Surface characterisation and bulk studies

X-ray photoelectron spectroscopy (XPS) was employed in attempt to chemically characterise the surfaces studied by AFM. It is noted that this study was a collaboration work, and Dr. Sven Koehler and Lauren Newton from the University of Manchester are acknowledged conducting these XPS experiments, where the experimental details are given in Chapter 4.

Only two spectra were successfully recorded, one from the surface aged in 0% RH, and the other at 98% RH and 40°C for one week. The reason for the much shorter storage period was due to the limited time available to prepare the samples for XPS studies. The storage temperature was raised from room temperature to 40° in order to accelerate the surface reaction rate within the shorter storage time. Although the conditions were different to the samples studied in the previous sections by AFM, tall features ranging from 100 to over

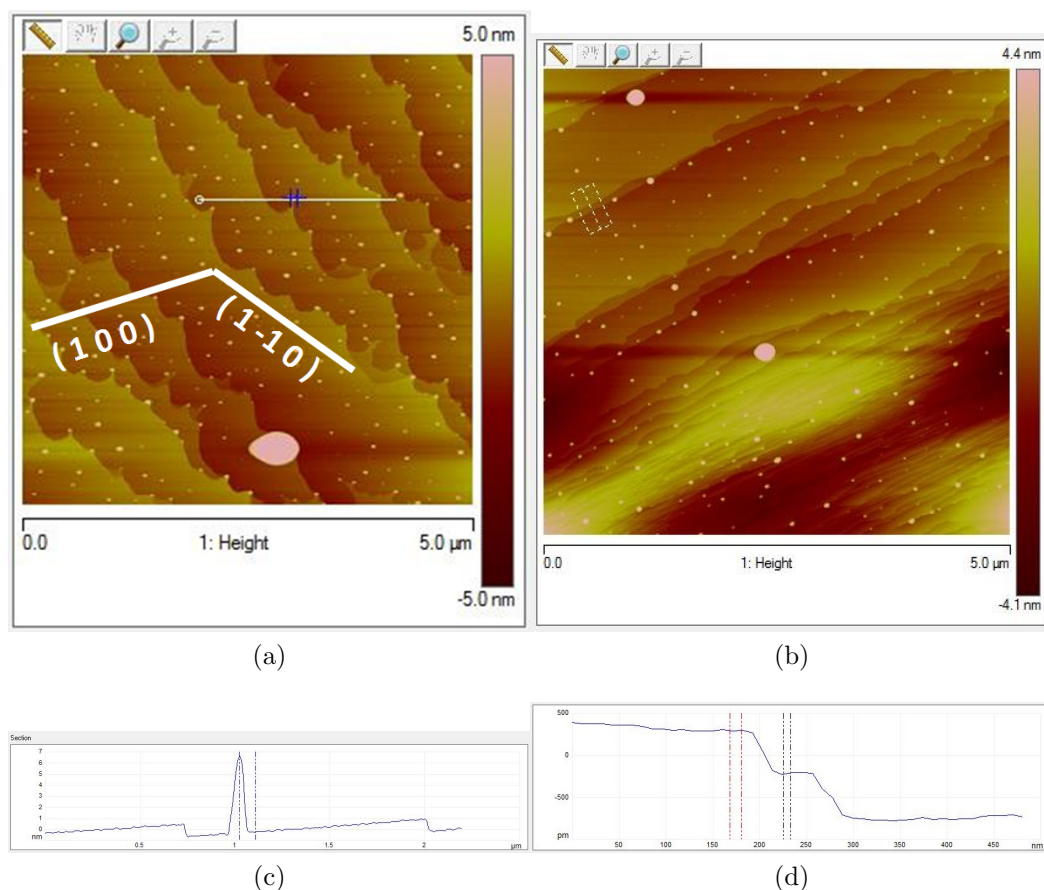


Figure 6.16: (a) and (b) Two representative AFM images of an ASA surface aged in toluene atmosphere for two months ($5 \times 5 \mu\text{m}^2$). The orientation of (100) and (1-10) faces for both images are indicated by the thick white lines; (c) The cross sectional height of the white line in (a). The height of a tall feature was measured to be 70 Å; (d) The average cross section taken across the steps enclosed by the broken lines in (b), showing steps of 5.3 Å in height, corresponding to the length of one ASA molecule along {001}.

400 Å in height were observed, which were similar to the features on the surface aged at room humidity for two months (Figure 6.17).

The carbon 1s XPS results are shown in Figure 6.18, together with the theoretical spectra of ASA and SA. For the theoretical ASA spectrum, there are two main bands at 285 eV (corresponding to the $\underline{\text{C}}=\text{C}/\underline{\text{C}}\text{-COOH}$ environments) and 289.5 eV ($\underline{\text{C}}\text{OOH}$) with a clear shoulder at around 286.5 eV ($\underline{\text{C}}\text{-O}$), while for theoretical SA spectrum both main bands are also present, with the intensity at 285 eV proportionally greater than that at 289.5 eV, and a greater contribution from the shoulder at 286.5 eV. The experimental XPS of the crystal aged in 0% RH (Figure 6.18(e)) matched the theoretical spectrum of ASA, as well as the (001) spectrum obtained from another study in the literature [169]. For the crystal aged in 98% RH and 40°C (Figure 6.18(f)), the spectrum did not match either of the theoretical ASA or SA spectra. Only one asymmetric broad peak was observed that spanned the range from 283 to 291 eV, where the

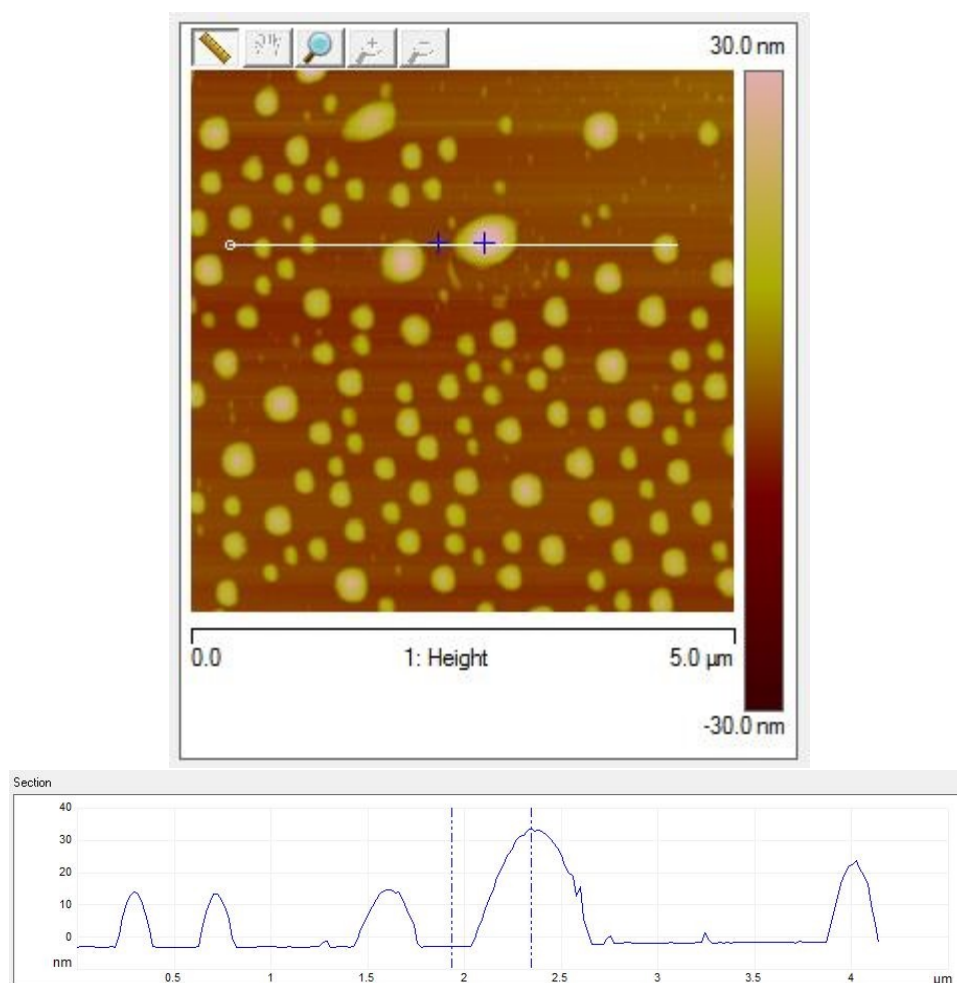


Figure 6.17: A representative AFM image of an ASA surface aged in 98% RH and 40°C for one week in preparation for XPS studies ($5 \times 5 \mu\text{m}^2$). The cross sectional height of the white line in the image is shown below, passing through several tall features that range from 100 to 400 Å in height.

maximum intensity was at 285 eV, together with a shoulder region at around 287 eV. Therefore, the spectrum could not be resolved to any specific carbon environments present. Nonetheless, compared to the spectrum obtained from the crystal aged in 0% RH, the intensity at 289.3 eV (COOH) was significantly lower for the spectrum obtained from aging in 98% RH and 40°C, suggesting a loss of COOH.

Although there was a significant difference between the XPS of the crystal aged in extreme humidity (and elevated temperature) and that aged in dry conditions, the XPS studies failed to indicate the exact chemical composition of the aged surfaces. It is possible that the resultant surface might be a mixture of substances including ASA, SA, as well as other components. Moreover, the spectrum of the crystal aged at elevated temperature and humidity might not reflect the same chemical composition of the crystals aged at room temperature

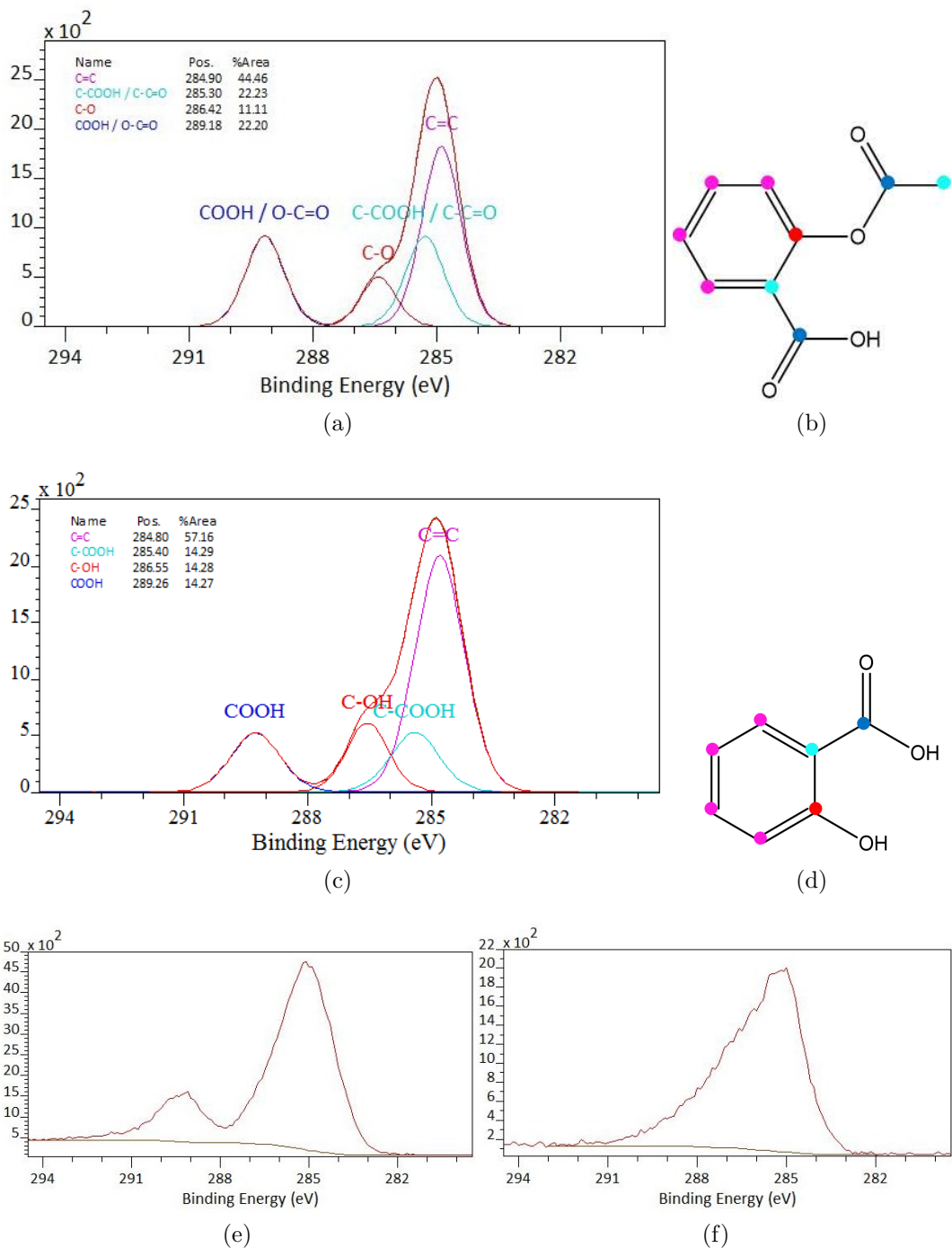


Figure 6.18: Theoretical carbon 1s XPS spectrum of ASA (a) and SA (c). The breakdown of the contribution from different carbon environments is shown together with the overall spectra. The molecular structure of ASA (b) and SA (d) is shown with atoms colours according to different carbon environments contributing to the XPS signal. The experimental carbon 1s XPS spectrum of {001} of ASA aged in 0% RH is shown in (e), while the spectra of the crystal aged in 98% RH (40°C) is shown in (f). The vertical axis of all the plots correspond to relative intensity detected at varying binding energies.

that were studied by AFM.

Attempts were made to repeat this XPS studies on more crystals aged in humidity. However, all the selected crystals were damaged either during transport or loading onto the instrument, and no further spectra were obtained. Nonetheless, this XPS study strongly indicated that there was a change in chemical composition of the surface stored at 98% RH and 40°.

Other analytical techniques were employed in attempt to characterise the bulk of the aged samples. Ground ASA samples were aged in 98% RH and 50% RH for over two months, and the PXRD patterns and ATR-FTIR spectra were recorded before and after aging (Figure 6.19 and 6.20), and neither indicated any changes after aging. This further confirms that the reaction mainly occurs on the crystal surface and not the bulk, which agrees with the more recent surface nucleation hydrolysis models in the literature [145].

6.5 Discussion

An overview of the surface study of ASA by AFM is presented in Figure 6.21, which shows a series of 3-D height profiles, corresponding to the height images in Figure 6.11 to 6.16. The following can be rationalised based on the results of the study so far:

1. Over a period of two months, there is no significant change in the bulk of ASA crystals aged in different conditions at room temperature.
2. In the absence of moisture, no tall features emerge and grow on the surface.
3. At moderate RH, several tall features are observed, indicating significant reaction.
4. The presence of macrosteps on some surfaces suggests that rearrangement of the surface molecules has occurred, possibly driven by the growth of tall features, as well as the natural sublimation of ASA as described in Chapter 5.

As no chemical characterisation was available for the surfaces aged in humidity (at room temperature), the reason for the absence of tall features on the surface stored in 98% RH is unclear. The increase in step height from an average of 5.4 Å to 6.0 Å suggests that a new chemical species might have formed on the terrace of the surface, which might be a result of the hydrolysis of ASA. This is not unlikely, as under such conditions, hydrolysis of ASA is expected to

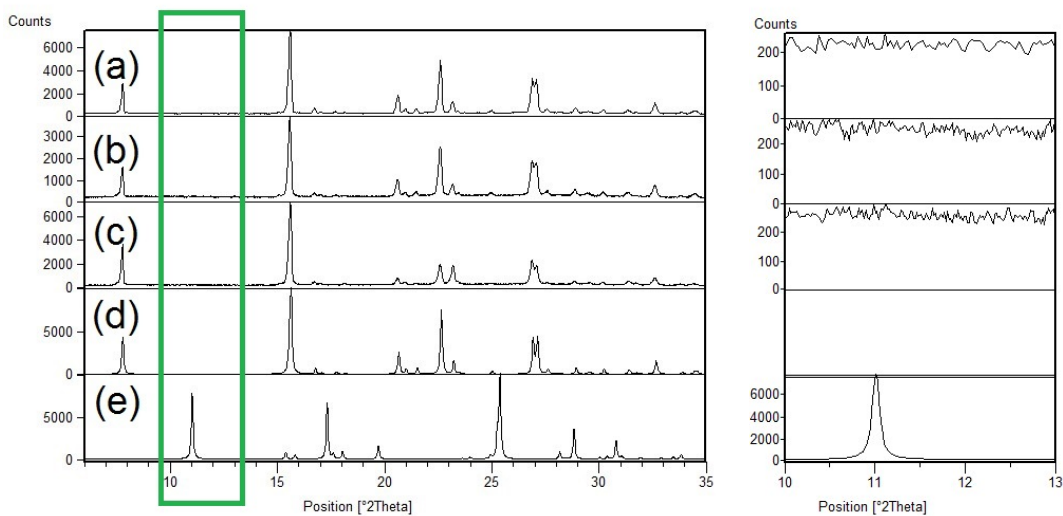


Figure 6.19: PXRD patterns of (a) ground ASA before aging; (b) ground ASA after aging for 2 months in 50% RH; (c) ground ASA after aging for 2 months in 98% RH; (d) simulated powder pattern of ASA form I; (e) simulated powder pattern of SA. A closeup of the region $10^\circ < 2\theta < 13^\circ$ (enclosed by the green rectangle) is shown on the right, indicating the absence of the SA reflection at $2\theta = 9^\circ$ for samples (a) to (c).

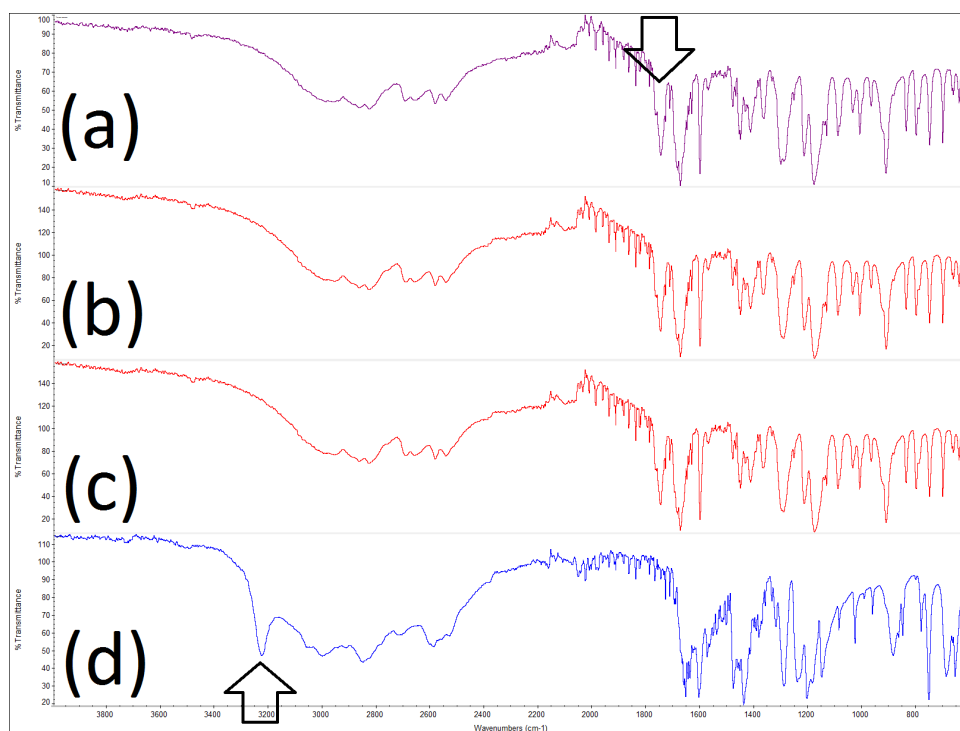


Figure 6.20: ATR-FTIR spectra of (a) ground ASA before aging; (b) ground ASA after exposure to 2 months of 50% RH; (c) ground ASA after exposure to 2 months of 98% RH; (d) SA (as purchased). The arrows indicate the distinct peaks of ASA and SA, and confirms that no SA peaks were observed in spectra (a) to (c).

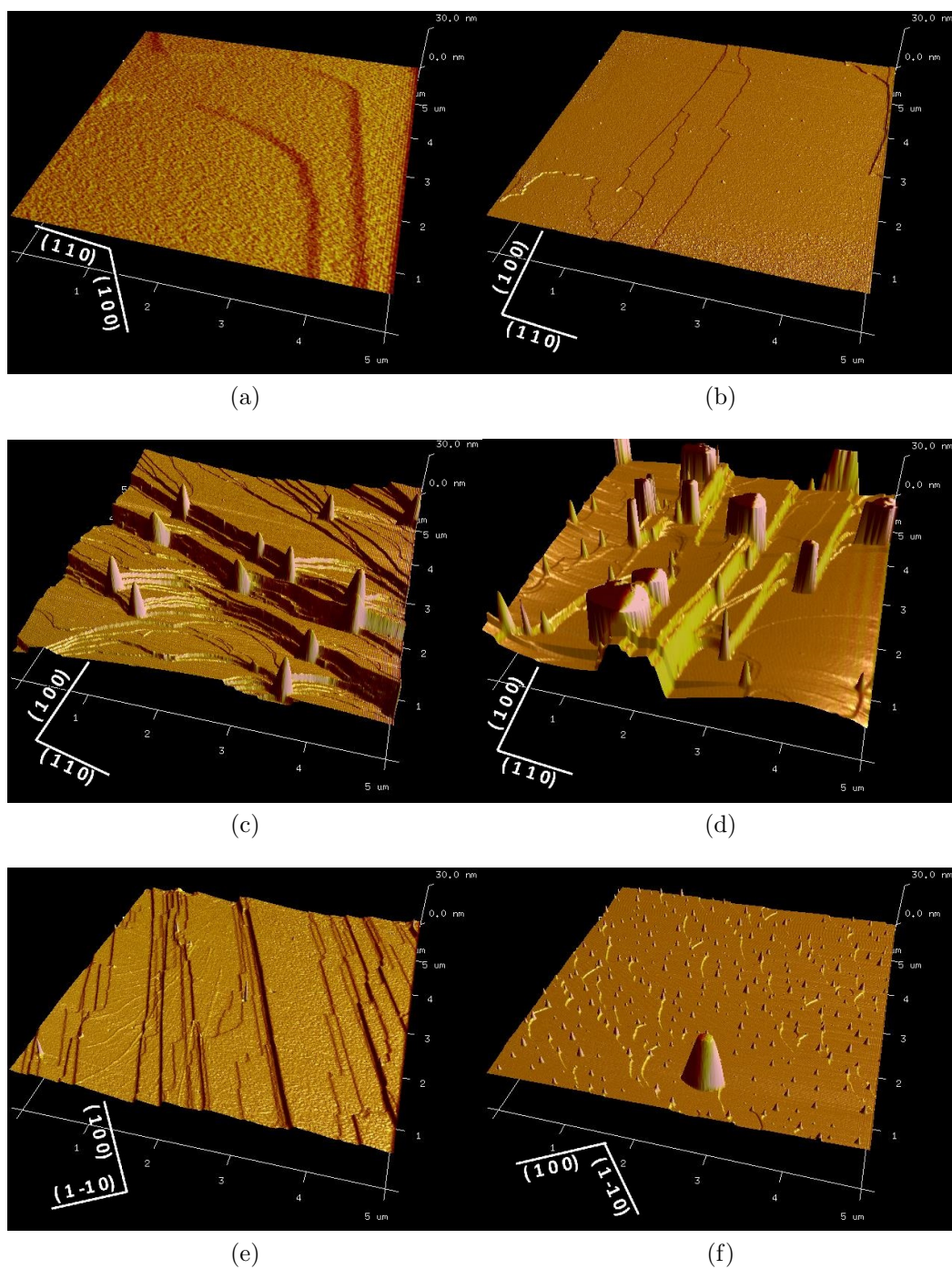


Figure 6.21: (a) A representative 3-D height profile (with an amplitude colour scale) of a fresh ASA {001} surface. (b - f) ASA {001} surface aged for two months in 0% RH (b), room humidity (30 to 60% RH)(c), 50% RH (d), 98% RH (e) and toluene atmosphere (f). The area and height range of all the images are fixed to be $5 \times 5 \mu\text{m}^2$ and 60 nm respectively for a better comparison of the images. The approximate orientation of the faces are indicated by the white lines at the bottom left of each image.

occur. Moreover, as the increase in RH allows more moisture to be adsorbed and condensed onto the surface, under such extreme RH it is possible that the amount of adsorbed moisture is large enough to dissolve both the tall features as well as the material on the terraces. As there are no longer specific sites of growth, the hydrolysis becomes a more homogeneous reaction occurring in the adsorbed layer of moisture, and recrystallising across the whole surface.

For the sample aged in toluene, tall features were also observed. This suggests that the growth of features is not exclusive to the presence of moisture. Any solvent vapour will likely provide a medium that mobilises surface molecules, and even dissolving them, in order to allow molecules to be transported from one region to another, which can promote the growth of tall features.

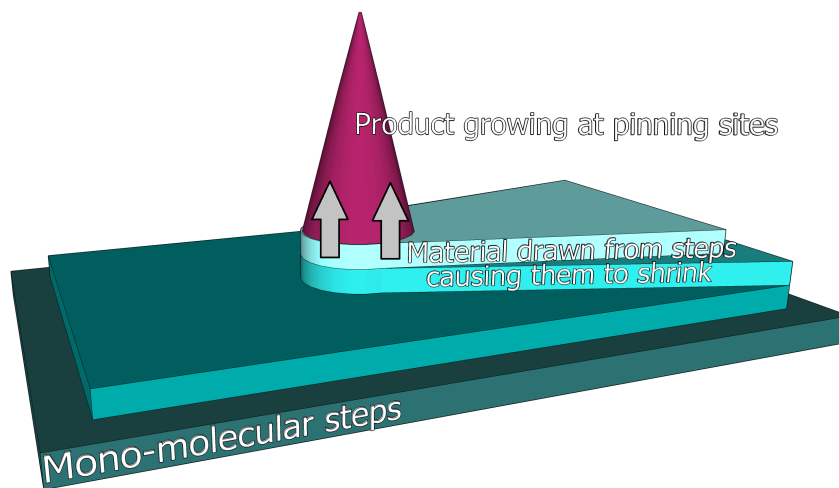
6.5.1 Proposed mechanism of surface product formation

Based on these observations, a mechanism of the formation and growth of the tall features on the surface is proposed in Figure 6.22(a):

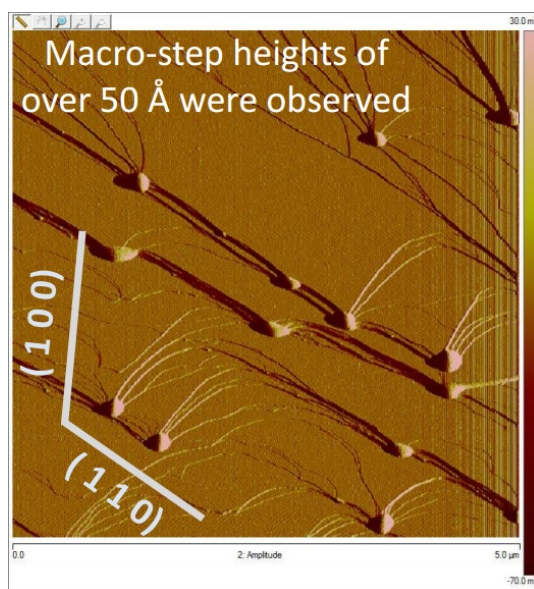
- In the presence of moisture or any solvent vapour, surface rearrangement is possible as the adsorbed solvent mobilises the top few molecular layers.
- Tall features are suggested to have formed at sites of defects or along the edge of steps, as these sites are relatively higher in energy than other flat terrace regions. Once formed, these tall features remain stationary relative to the rest of the surface, and continue to grow in time as steps continue to move along the surface.
- As these features grows, material is drawn from the top few layers on the flat terraces. These layers lose material gradually and shrink in size, causing the steps to migrate.
- While shrinking, these steps combine and align to create a slow growing face to reduce the number of steps and minimize the surface energy. An example is shown in Figure 6.22(b), where steps of over 50 Å were aligned to the slow growing face {110}.

6.5.2 Physical or chemical interaction?

Up to this point, the chemical composition of the tall features observed has still not been addressed. There are two possible routes of product formation, either via a chemical or a physical reaction. Based on previous bulk studies



(a)



(b)

Figure 6.22: (a) 3-D illustration of the mechanism of surface product formation; (b) Amplitude image of a sample $\{001\}$ surface aged in room RH with labelled crystal orientation ($5 \times 5 \mu\text{m}^2$).

on the hydrolysis of ASA (at extreme humidity and elevated temperatures) [135, 141, 142, 144], the tall features on the surface aged at 98% RH and 40°C are likely composed of SA, as the hydrolysis reaction is expected to occur under such condition.

However, at room temperature the hydrolysis is expected to be very slow. Given that there are no changes to the bulk over the two month ageing period for samples aged in humidity at room temperature, there is a possibility that any tall features observed on the corresponding surfaces are not due to the hydrolysis reaction, but simply due to the dissolution and recrystallisation of ASA molecules at the surface. This is not unlikely, as once the features have

emerged, they can template further molecules to deposit at the growing interface of these features which are kinetically more accessible than the regions of flat terraces. As a result, dissolved molecules may preferentially redeposit on tall features, contributing to their growth in size.

Solvent	Temperature (K)	"Solubility" of Aspirin (mol/dm³)	"Solubility" of Salicylic acid (mol/dm³)
Water	298	0.023	0.014
Water (0%RH)	298	0.000	0.000
Water (50%RH)	298	0.012	0.007
Water (98%RH)	298	0.023	0.014
Toluene	298	0.012	0.110
Acetone	298	1.028	2.122

Table 6.1: Solubility of ASA and SA in water and toluene at room temperature. From reference [187].

In an attempt to deduce the likely chemical composition of the surface products, the relative solubility of ASA and SA in water and toluene were considered (Table 6.1) [187]. In water, the solubility of ASA is greater than the solubility of SA. Therefore ASA is preferentially dissolved, compared to any SA that forms. As tall features are observed at moderate RH, these features are more likely to be SA than ASA.

In toluene, however, ASA is almost 10 times less soluble than SA, which would imply that any SA formed on the surface would most likely dissolve. Therefore, tall features composing of SA is less likely to emerge on the surface, and the observed tall features are a result of a physical dissolution and recrystallisation of ASA molecules on the surface.

6.6 Chapter conclusion

In this chapter, a study was conducted to investigate the surface response of ASA crystals in the presence of humidity and toluene vapour. The study focused on the response of {001} to different RHs as well as the toluene vapour environment, and the conclusions are as follow:

- A mechanism was proposed to describe the formation of tall features on the aged surface, which applies to both scenarios where such features form and grow via a physical or chemical reaction.
- Under dry conditions, no reaction on the surface is expected, due to the lack of medium to dissolve and mobilise surface molecules. Therefore, the

mechanism requires the presence of moisture or other solvent vapour in order for any surface reaction to occur.

- At a moderate RH level, the emergence of tall features is suggested to be composed of SA based on a solubility comparison analysis of SA and ASA in water.
- At extreme RH, the absence of any tall features is likely due to a large amount of water adsorbed onto the surface, dissolving any features that were originally present. A change in step height was detected, but the standard deviation of the measured step heights were large. It is suggested that there might be a change in composition of the surface due to the hydrolysis of ASA to SA, which is expected to occur under such conditions.
- The surfaces aged in a toluene atmosphere also contained tall features. Based on the solubility analysis, these features are not likely SA, but are a result of a physical process, where surface ASA molecules are dissolved and recrystallised at tall features (which are kinetically more accessible).

The results have highlighted the importance of studying the solid-state reactivity of organic solids at the surface level, which can allow a more fundamental understanding of the nature such reactions. Moreover, the surface rearrangement of ASA crystal surfaces due to exposure to toluene vapour was discovered. Future work should focus on identifying the chemical species of the surface products observed by AFM, in order to confirm the findings presented in this chapter. The effects of ageing ASA crystal surfaces in other solvents is also suggested, which may be a potential method to manipulate and control crystal surface features and reactivity.

Chapter 7

Following changes on crystal surfaces during photochemical reactions: A case study on anthracene (AN)

7.1 Introduction to solid-state photochemical reactions and the topochemical postulate

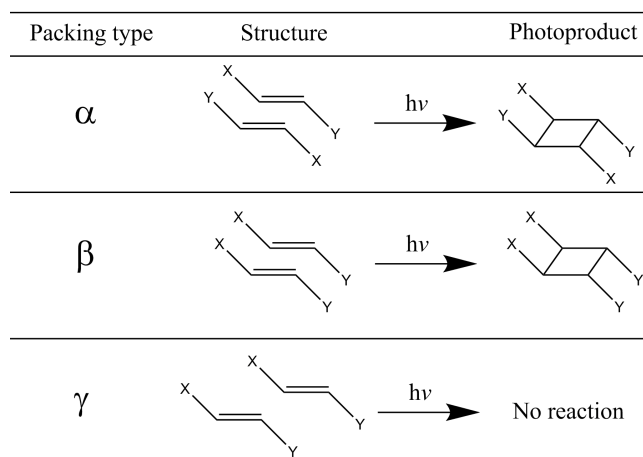


Figure 7.1: Three types of crystal structure classification based on the geometric relationship between neighbouring molecules.

Solid-state photochemical reactions have been known to exist for a long time, but only gained popularity and have been studied extensively since the 1960s. These reactions occur by exposing crystals to UV or visible light, and very often can proceed to 100% conversion of the starting material. One of the first reviews on photoreactions of organic solids was published by Cohen

in 1975 [188]. The best studied systems at that time were the (2+2) photocyclodimerisation of materials such as trans-cinnamic acid derivatives, dienes and stilbenes. These materials could be classified into three groups based on the geometric relationship between neighbouring molecules in the crystal structure (Figure 7.1), each group responding differently to UV light. As the family of trans-cinnamic acid derivatives spans across all three groups, this family of materials will be used to illustrate the photoreactivity of each group.

The topochemical postulate was initially proposed by Cohen and Schmidt [189] to explain photoreactivity. The postulate states that “*reaction in the solid state occurs with a minimum amount of atomic or molecular movement*”. For photodimerisation to occur, pairs of C=C double bonds have to be closer than a distance suggested to be 4.2 Å in order for the p(z) orbitals to overlap sufficiently. Therefore, as both the α and β polymorphs of cinnamic acid derivatives have separation of the pairs of C=C groups in between 3.6 to 4.1 Å, photodimerisation occurs, and β -cinnamic acid derivatives yield the tail-to-tail dimer, and α -cinnamic acid derivatives yield the head-to-tail dimer. The γ -cinnamic acid derivative polymorphs on the other hand have C=C separation distances of 4.7 to 5.1 Å, which is considered too far apart for dimerisation to occur within the perfect crystal (Figure 7.1) [190, 191].

7.1.1 Anomalies of the topochemical postulate, *e.g.* AN

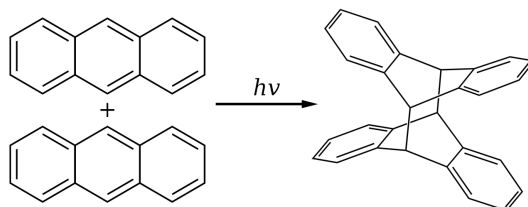


Figure 7.2: Photodimerisation scheme of AN.

There are exceptions where the photoreactivity and corresponding products of some crystalline materials do not conform to the topochemical postulate. One example is AN, which in the presence of UV light was shown to photodimerise (Figure 7.2) [192, 193].

The crystal structure of AN is shown in Figure 7.3 [180]. The BFDH morphology model predicts the (001) face to be the dominant growth face, which is hexagonal in shape. The unit cell parameters are as follow:

- $a = 8.441 \text{ \AA}$, $b = 5.996 \text{ \AA}$, $c = 11.112 \text{ \AA}$
- $\alpha = 90^\circ$, $\beta = 125.18^\circ$, $\gamma = 90^\circ$

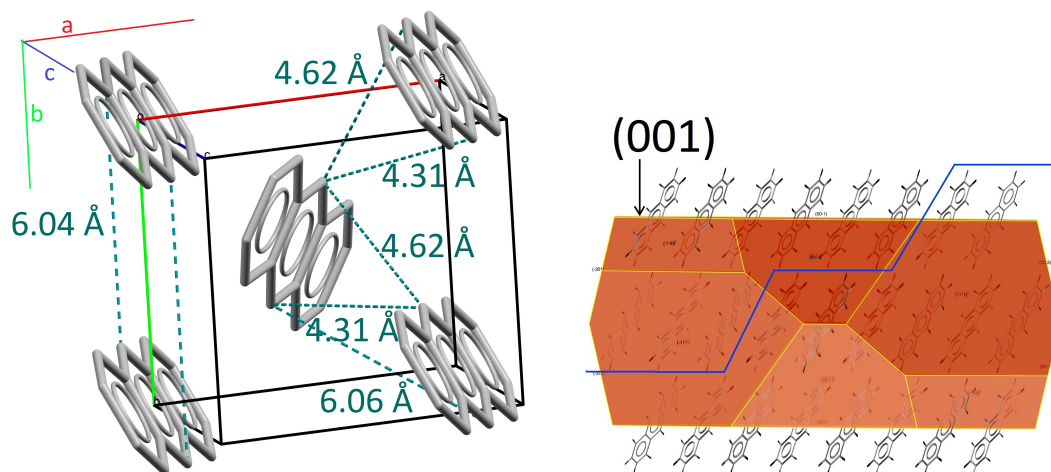


Figure 7.3: A unit cell in the crystal structure of AN (CSD reference: ANTCEN10) [180], showing the distance between the nearest neighbour molecules (left), and an overlay of the BFDH morphology prediction (right), where the top face is (001). The blue line indicates the monomolecular steps (of approximately 1 nm) that are expected to be observed on the (001) surface. Moreover, the AN molecules are not parallel to their neighbour molecules.

- Space group: $P 2_1/a$; Unit cell volume = 459.725 \AA^3

The closest distance between any pair of AN molecules is 4.31 \AA (Figure 7.3(a)), which is greater than 4.2 \AA . Moreover, as there are no parallel pairs of molecules in the structure the reactive centres are not aligned correctly for the reaction to occur. Therefore, the topochemical postulate predicts that AN is not photoreactive. However, Chandross and Ferguson reported that crystalline AN reacts photochemically to yield dianthracene (diAN) [193]. Kaupp further studied this reaction by AFM, and showed substantial material transport at the surface of AN crystals, contradicting the emphasis on minimum movement of molecules according to the topochemical postulate. It was also suggested that AN photoreactivity was enhanced at the surface compared to the bulk, as the high absorption of light by AN crystals will limit the penetration of light to the bulk of the crystal [192]. Furthermore, both Thomas *et al.* [194] and Craig *et al.* [195] suggested that such photoreactions are likely to occur at defects, where the molecules are displaced from regular lattice sites, which may reduce both the distance between molecules and activation energy required.

In this chapter, the surface reactivity of AN will be further investigated. In particular, the role of defects is assessed with the aid of AFM continuous imaging.

7.2 Experimental setup

7.2.1 Preparing AN crystals

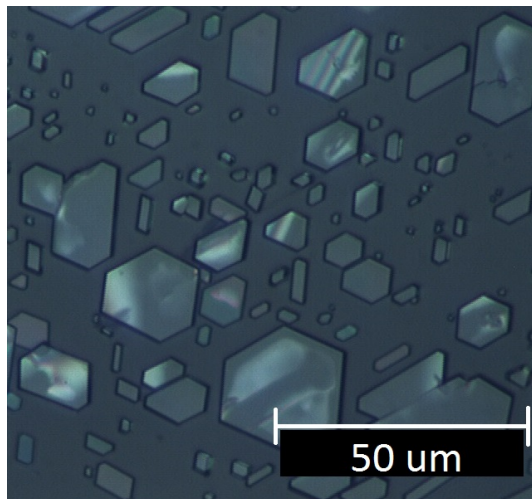


Figure 7.4: Polarised optical microscopy images of AN crystals obtained by recrystallisation from ethyl acetate, showing hexagon-shaped crystals ranging from 5 to 40 μm in length.

AN was sourced from Sigma Aldrich. For the bulk studies, including ATR-FTIR and PXRD, the sample was ground to minimize the preferred orientation in the PXRD patterns. Crystals for AFM imaging were prepared by applying a drop of ethyl acetate saturated with AN onto round glass coverslips. Upon evaporation of the solvent, crystals of hexagonal morphology formed (Figure 7.4), which matched the predicted morphology of AN with (001) being the dominant hexagonal face. The 1-D XRD pattern was identical to those obtained for the AN crystals prepared in Chapter 5, which revealed (001) as the dominant deflection (Figure 5.3). The coverslips were then mounted onto a magnetic steel disc to be imaged by AFM.

7.2.2 Studying the photoreaction of AN surfaces

An AM4113T-FVW Dino-Lite handheld digital microscope was used as a UV-A light source (mean emission wavelength of 400 nm). The microscope was placed near the AFM with the light shining on the sample (Figure 7.5).

All of the experiments were carried out under ambient room conditions (18 to 23°C, 30 to 60% RH) with the exception of that described in section 7.3.2, where a low RH was required. In this case, a humidity chamber was added onto the AFM (Figure 7.6), with the UV light source placed slightly further away from the sample, and incident through the perspex shield. As the amount of UV light absorbed by the shield was not determined, studies with and without

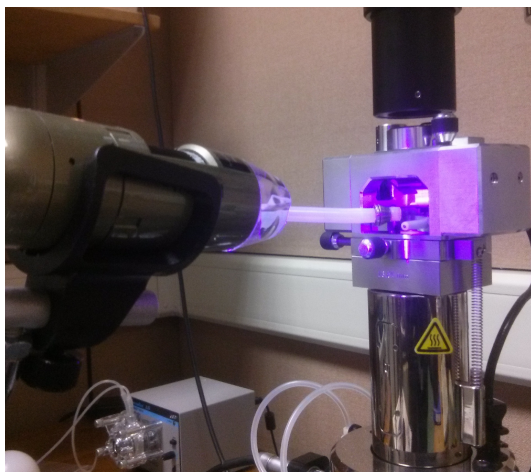


Figure 7.5: Set up of AFM imaging next to a UV-A light source.



Figure 7.6: Set up for AFM study under controlled humidity level.

the shield were considered separately in order to ensure the same amount of UV light exposure to the samples for a fair comparison.

7.3 Experiments and results

The following experiments were all conducted at ambient temperature:

1. Bulk analysis of AN crystals by ATR-FTIR and PXRD, before and after exposure to UV for one week under ambient condition.
2. Surface analysis of AN crystals by AFM:
 - (a) Non-continuous imaging of AN (001) before and after exposure to UV for 5 hours.

- (b) Continuous imaging of AN (001) during exposure to UV at a rate of approximately 9 minutes per image frame.
- (c) Non-continuous AFM imaging of AN (001) at different relative humidity (RH).

7.3.1 Bulk photoreactivity of AN crystals



Figure 7.7: Picture of AN crystals before (left) and after (right) exposure to UV light for 1 week.

AN crystals before and after exposure to UV for one week show a significant colour change (Figure 7.7). The yellow colour of the crystal after UV exposure matches the oxidation product anthraquinone (ANQ), which indicates that oxidation might have occurred.

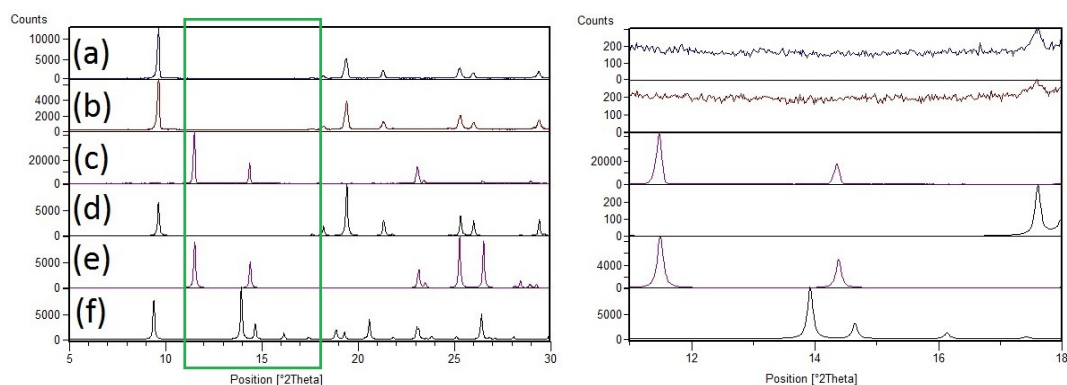


Figure 7.8: PXR D patterns (left) of (a) recrystallised AN; (b) sample (a) exposed to UV for one week; (c) commercial ANQ as purchased; (d) simulated pattern of AN [180]; (e) simulated pattern of ANQ; (f) simulated pattern of diAN [196]. The same patterns are shown on the right with 2θ ranged between 11° and 18° (range enclosed by the green rectangle on the left).

However, the PXR D patterns of AN crystals before and after UV exposure do not show evidence of any changes (Figure 7.8). This suggests that the component giving rise to the yellow colour is either amorphous, or the amount of it is insufficient to be detected by PXR D.

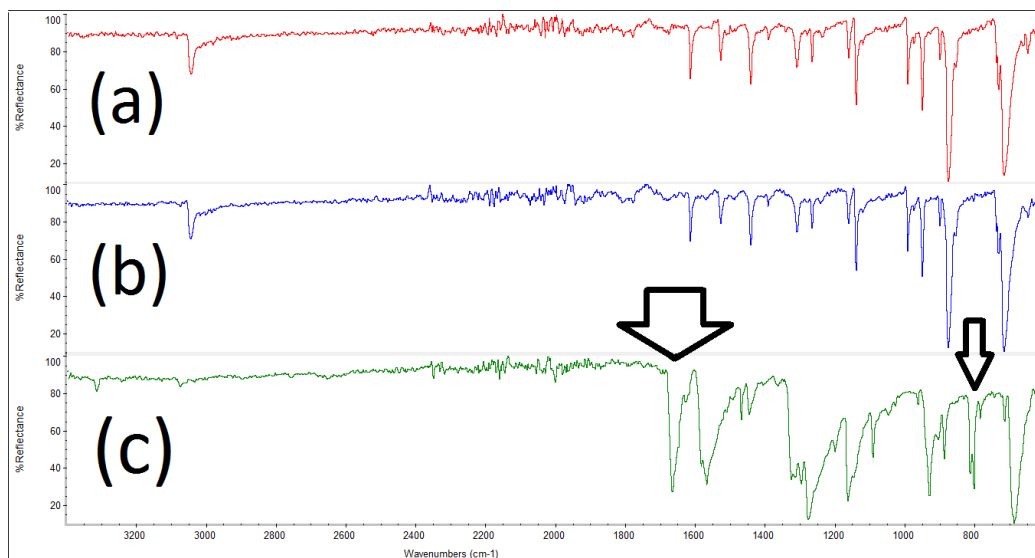


Figure 7.9: ATR-FTIR pattern of (a) recrystallised AN; (b) sample (a) after exposure to UV light for one week; (c) ANQ (as purchased). The arrows indicate the distinct absorption peaks only observed in ANQ, which were not detected in all other samples. The peak at around $1670 - 1680 \text{ cm}^{-1}$ corresponds to the C=O stretch of ANQ.

The ATR-FTIR spectra are shown in Figure 7.9. AN and ANQ can be readily distinguished by the presence of an absorption peak at $1670 - 1690 \text{ cm}^{-1}$, which is due to the carbonyl peak present in ANQ. The presence of ANQ is not seen in the AN sample before nor after UV exposure. This suggests that the reaction is occurring at the surface, which is not detected by ATR-FTIR, as the normal penetration depth of this ATR-FTIR technique is several hundred μms .

7.3.2 Surface photoreactivity of AN crystals

Non-continuous AFM imaging

As a control experiment, an AN surface was exposed to ambient conditions in the dark. This was to verify that there were no changes when the samples were not exposed to any UV or visible light. The sample was imaged by AFM before and after an ageing period of 4 hours (Figure 7.10), and the area showed no significant changes. Initially, the surface contained mainly step features of $10.7 \pm 0.4 \text{ \AA}$ in height, which corresponds to the thickness of one AN molecule along [001] (see Figure 7.3). After ageing, the only observation was the movement of steps, but this was likely due to the natural sublimation of AN, as discussed in Chapter 5. Therefore, based on these observations, no reaction is expected to occur in the dark apart from the slow sublimation of AN molecules from the surface.

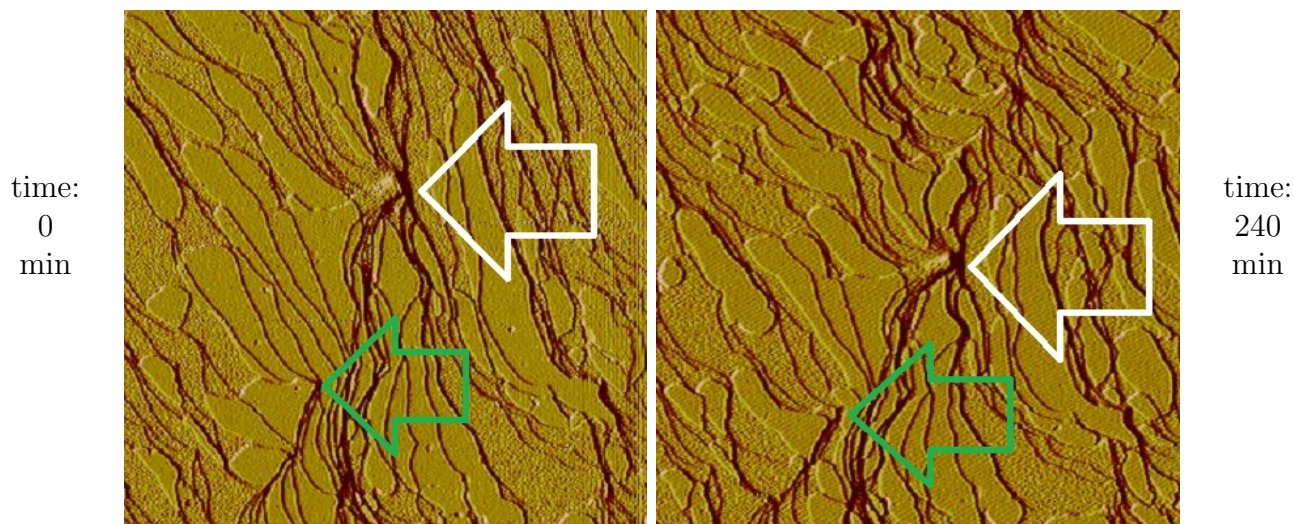


Figure 7.10: Amplitude AFM images of (a) a fresh AN (001) surface; (b) the same surface after storage in ambient conditions in the dark. The area of imaging is $3 \times 3 \mu\text{m}^2$. The typical step height measured was $10.7 \pm 0.4 \text{ \AA}$. The arrows indicate the same features found in both images.

The experiment was repeated on a fresh crystal, this time in the presence of UV light. After 4 hours of UV exposure in ambient conditions, the surface of AN showed significant changes (Figure 7.11). The overall roughness of the surface increased, and Rq before and after exposure to UV were $0.5 \pm 0.3 \text{ nm}$ and $3.5 \pm 0.3 \text{ nm}$ respectively, where these values were measured on the terraces on the surface, which did not contain any steps and tall features. However, photoreactivity was observed to be more enhanced at step edges. As highlighted in blue in Figure 7.11, this region originally contained pits of 1 – 3 nm in height, reacted to yield surface products of over 40 nm in height. The white arrows indicate a large step feature of 3 nm originally, which showed significant product formation of 20 nm. Although new protruding features were also observed throughout the surface, the height of these features are significantly greater at regions of pits and steps, suggesting that photoreactivity is more pronounced at these sites of surface defects.

Continuous AFM imaging

In order to gain a better understanding towards how the photoproducts emerge, a fresh (001) AN surface was monitored continuously by AFM imaging (10 min/image), and under continuous UV irradiation. A set of 6 representative 3-D height profiles of this study is given in Figure 7.12 to provide an overview of the reaction. A more detailed analysis will be given below in reference to the corresponding height profile images given in Figure 7.13. For reference, the table below shows the relationship of the subfigures in Figure 7.12 and 7.13:

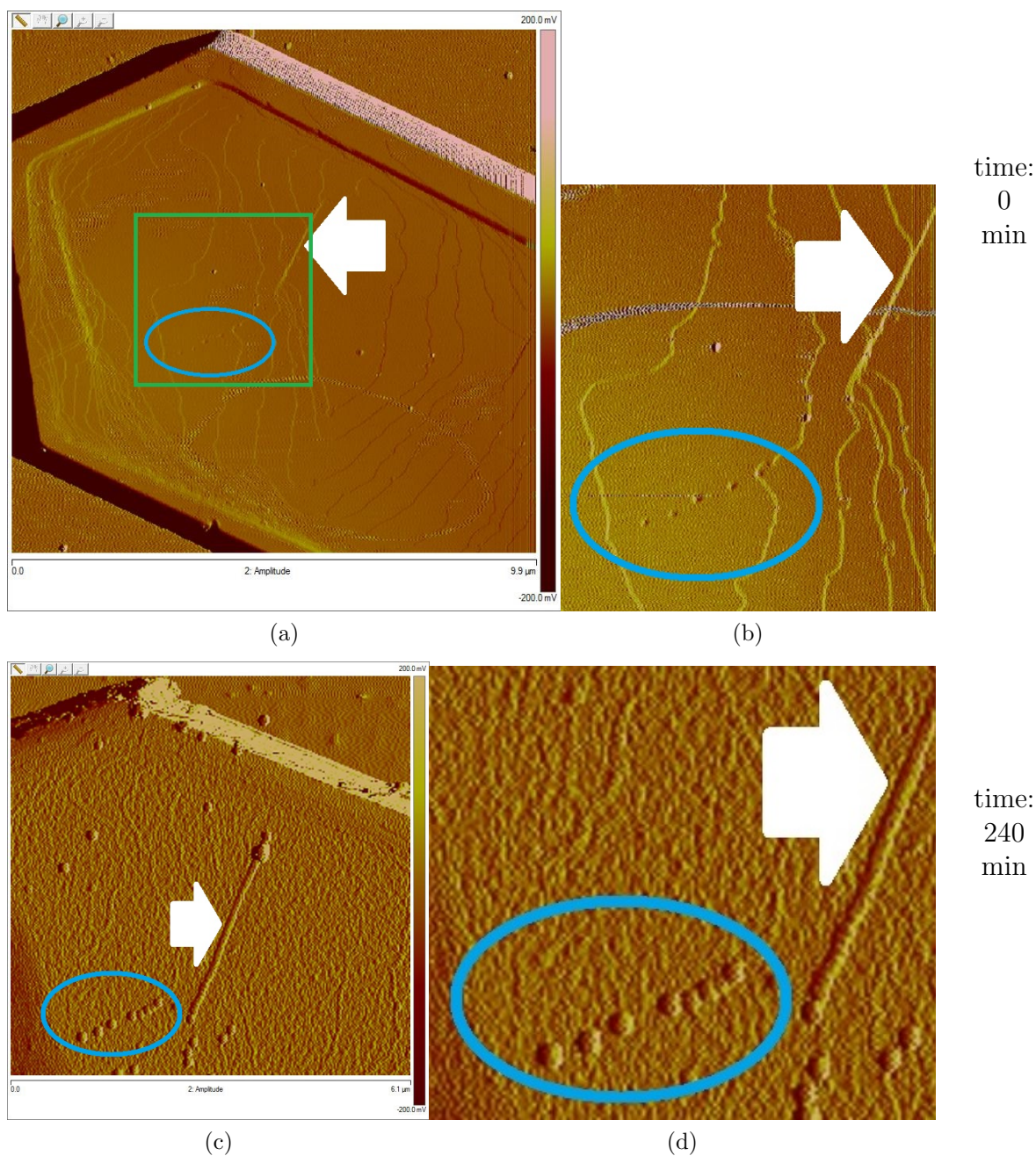


Figure 7.11: Amplitude images of AN crystal surface (a) before exposure to UV light ($9.9 \times 9.9 \mu\text{m}^2$); (b) a close up image of the area enclosed by the green rectangle in (a); (c) after exposure to UV light ($6.1 \times 6.1 \mu\text{m}^2$); (d) a close up image of (c). The white arrows indicate the same step feature of 3 nm height, while highlighted in blue is originally an array of pits ranging from 1 – 3 nm in depth. After exposure to UV light, new protruding features of 20 – 50 nm in height were observed at both of these features, indicating significant reactivity. The surface roughness (Rq) measured before and after exposure to UV were 0.5 ± 0.3 nm and 3.5 ± 0.3 nm respectively. Note: The images shown in this figure were selected for better representation purposes. These images were recorded prior to those shown in Figure 7.10, and the step edges appeared to be much straighter than those shown in Figure 7.10. It is suspected that over time there could have been a gradual degradation of AN and build up of impurity in the solvent, which could affect crystallisation and give rise to the difference in these step edge features. However, it was observed that such difference did not affect reactivity of the crystal surfaces, as crystals prepared at a later date (where the step features were less straight) changed in the same way as shown in the images shown in this figure (upon exposure to UV light).

Time (min)	3D height image in 7.12	Corresponding 2-D height profiles in 7.13
0	(a)	(a), (b), (c)
80	(b)	(d), (e), (f)
480	(c)	(g), (h), (i)
560	(d)	(j), (k), (l)
800	(e)	(m), (n), (o)
1160	(f)	(p), (q), (r)

Initially the surface contained a few tall features believed to be the result of photodimerisation occurring during sample preparation in an illuminated room. The rest of the surface was relatively flat, containing an emerging screw dislocation and many step features of 1 molecule thick. There were also some pit sites which were 1 to 4 nm deep (examples are given in Figure 7.13 (b) and (c)). After 80 minutes of exposure to UV light, new features ranging from 3 to 6 nm in height emerged (Figure 7.13 (d)). The original pits and step edges appeared to be sites of product formation, as shown in Figure 7.13 (e) and (f).

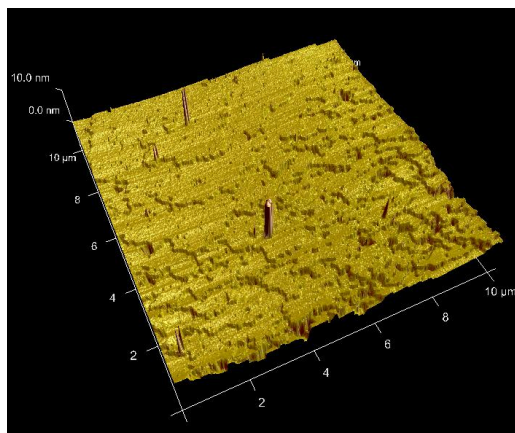
Over time, the features continued to grow in size, with several growing to 10 nm in height after 560 minutes (Figure 7.13 (g)). At this time, regions of step rearrangement were observed, as highlighted by the arrows in Figure 7.13 (h) and (i). Although natural sublimation of AN on the surface can give rise to such step movement, it is believed that this is not the only reason contributing to step rearrangement. As the growth of surface features draws material from the flat terrace regions, it is likely that this will also cause step movement as the terraces shrink in size.

As the steps continue to migrate, new sites of feature growth emerge (Figure 7.13 (k), (l), (n), (o)). Eventually product growth spreads throughout the whole surface, as shown in Figure 7.13 (f) and 7.13 (p), where the height of the observed features ranged from 5 to 30 nm. The features formed earlier continue to grow as new growth sites emerge, giving these earlier formed features more time for product formation. Therefore, the earliest formed features appear to have grown larger than those surrounding them (Figure 7.13 (q) and (r)).

To verify whether the surface was influenced by the AFM imaging tip, as discussed in Chapter 5, a larger area was recorded at the same position after the continuous imaging sequence (Figure 7.14). As there was no difference between the area that was repeatedly imaged and its surroundings, this indicated that the tip induction effect was not significant.

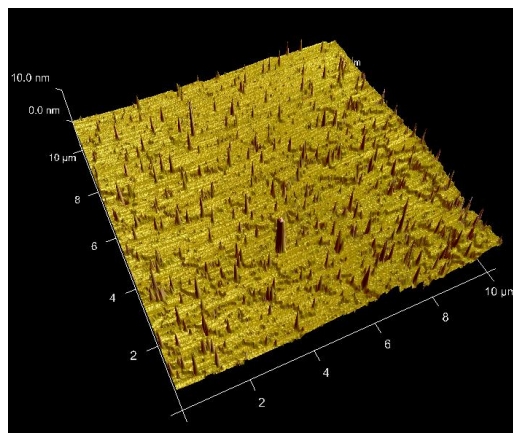
At this point it is worth commenting on the prepared AN surface in the

time:
0
min



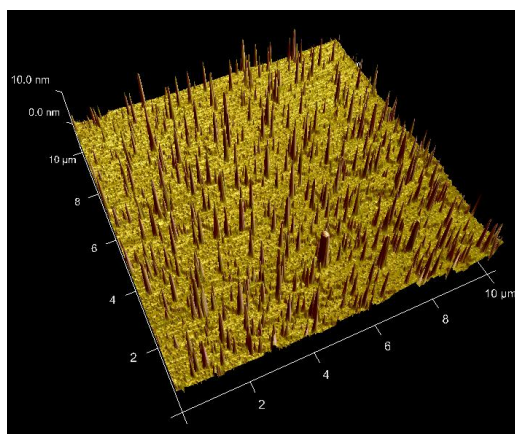
(a)

time:
80
min



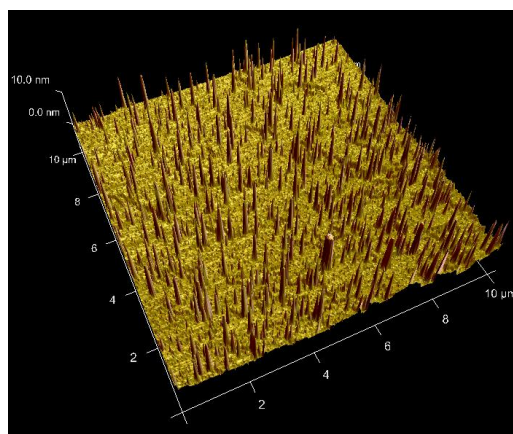
(b)

time:
480
min



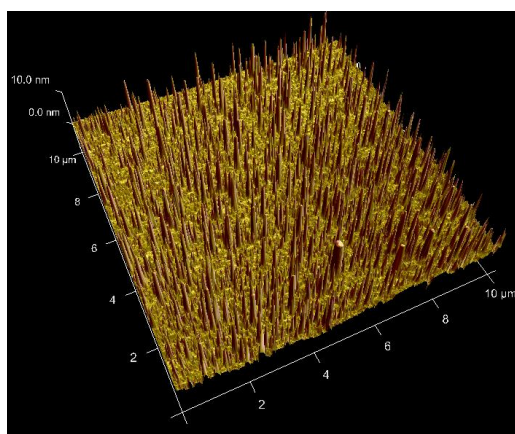
(c)

time:
560
min



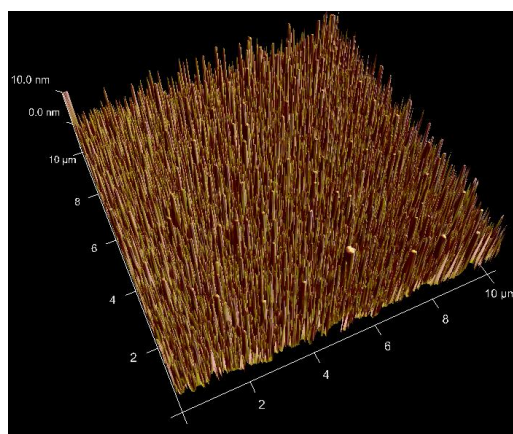
(d)

time:
800
min



(e)

time:
1160
min



(f)

Figure 7.12: 3-D Height profile of continuous AFM imaging on AN (001) surface exposed to UV for (a) 0 min; (b) 80 min; (c) 480 min; (d) 560 min; (e) 800 min; (f) 1160 min. The images are falsely coloured according to an amplitude scale for better representation. The imaging area is $10 \times 10 \mu\text{m}^2$ for all images.

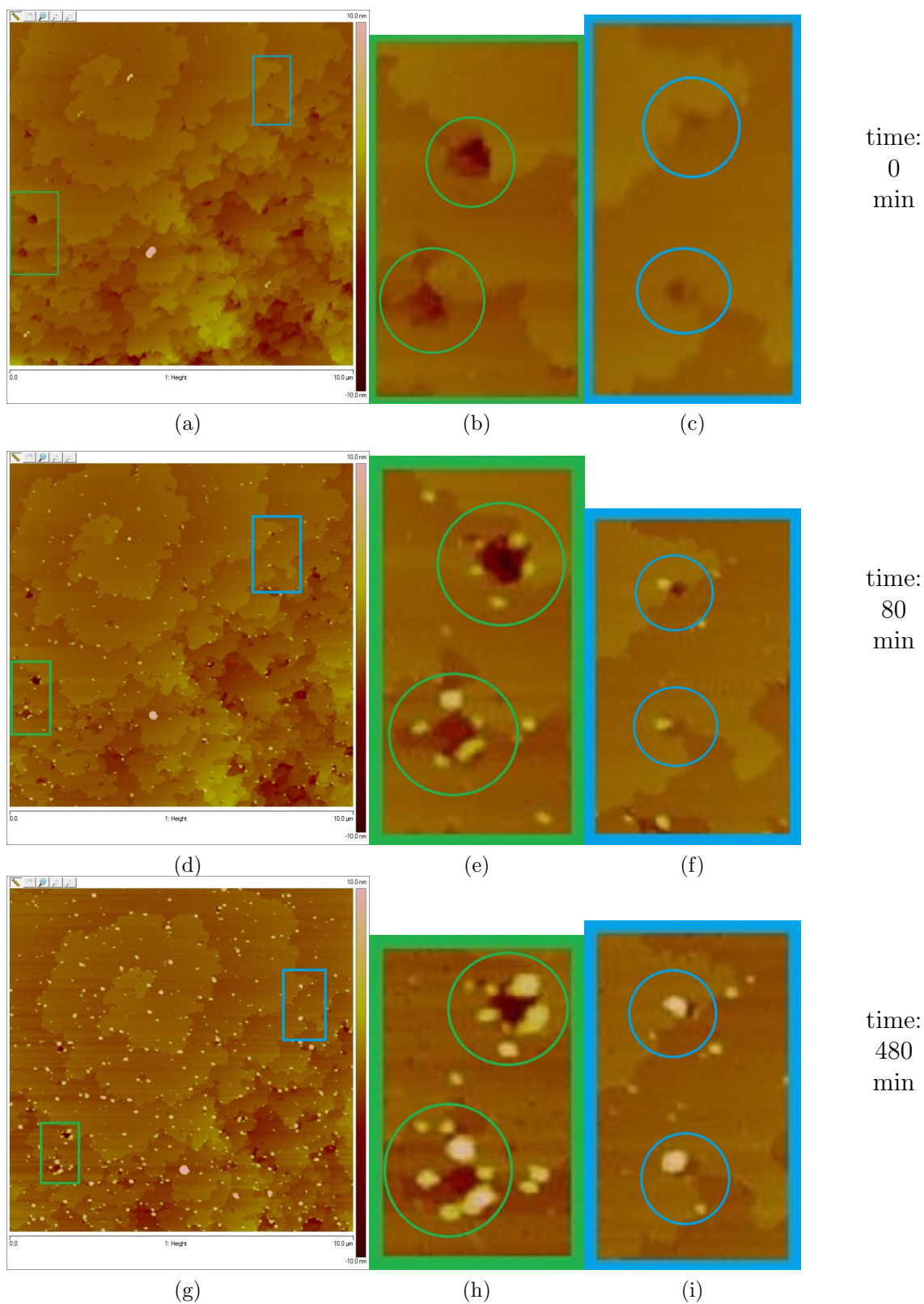


Figure 7.13: Height profile of continuous AFM imaging on AN (001) surface exposed to continuous UV for 0 min (a, b, c), 80 min (d, e, f), 480 min (g, h, i). The area of imaging was $10 \times 10 \mu\text{m}^2$ in (a, d, g), while (b, e, h) and (c, f, i) are close up images of the area enclosed by the green and blue rectangles respectively in (a, d, g). The circles indicate the position of the pits and steps originally present in (b) and (c) which later appear to be sites of high reactivity.

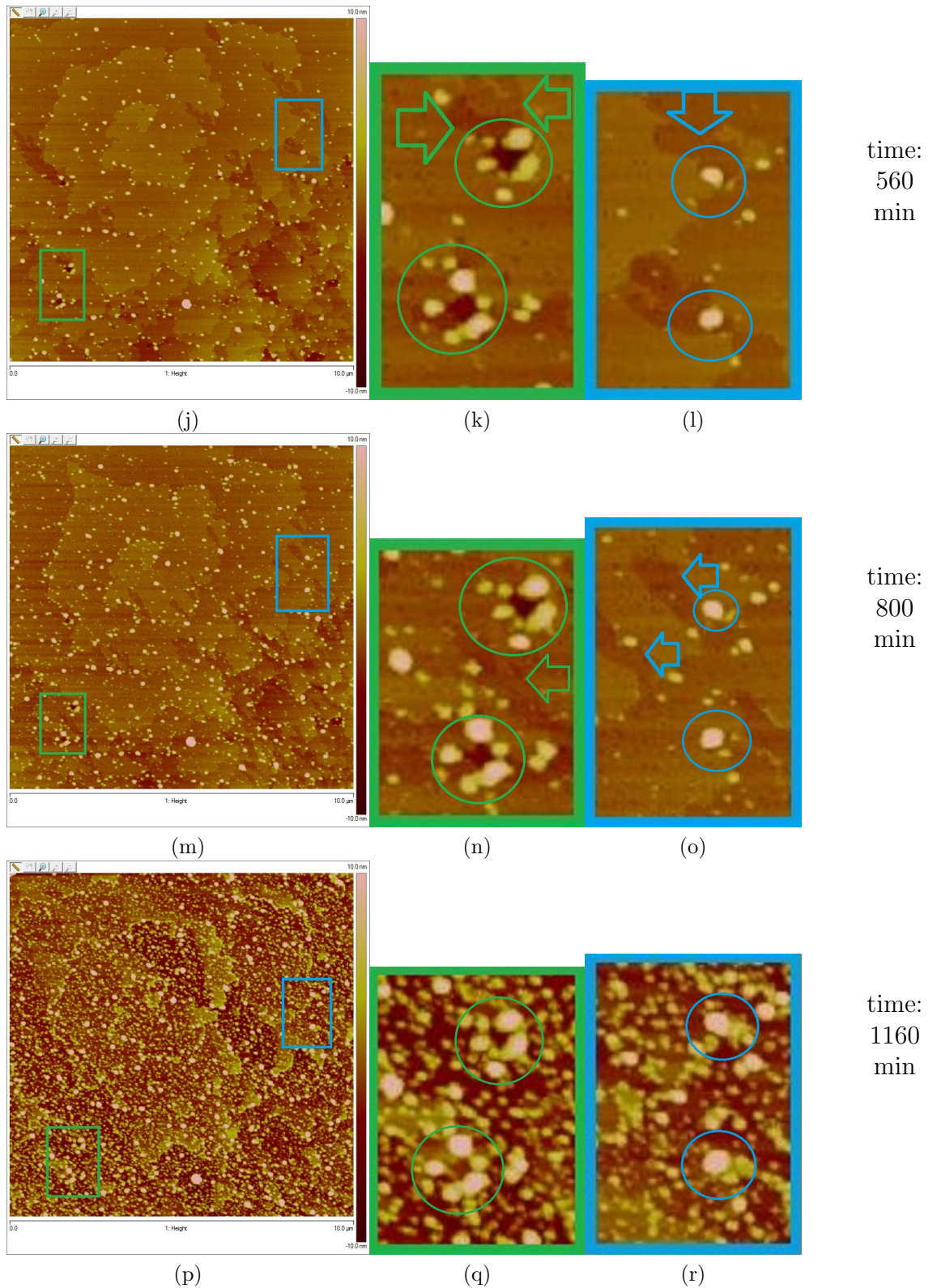


Figure 7.13 (cont.): Height profile of continuous AFM imaging on AN (001) surface exposed to continuous UV for 560 min (j, k, l), 800 min (m, n, o), 1160 min (p, q, r). The area of imaging was $10 \times 10 \mu\text{m}^2$ in (j, m, p), while (k, n, q) and (l, o, r) are close up images of the area enclosed by the green and blue rectangles respectively in (j, m, p). The arrows indicate regions of step movement, while the circles mark the original position of the pits and steps present in (b) and (c).

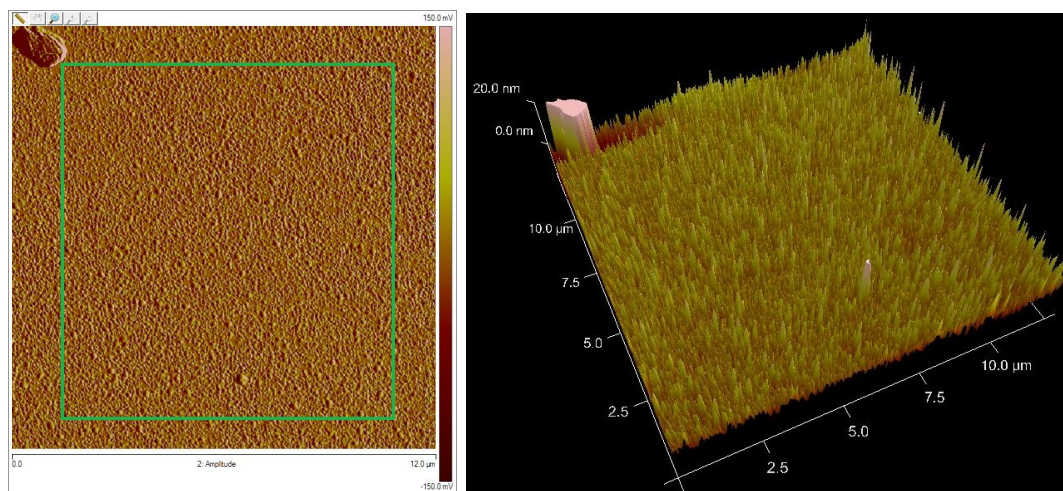


Figure 7.14: (a) Amplitude image, and (b) 3-D height profile of a larger area ($12 \times 12 \mu\text{m}^2$) at the same position that was repeatedly imaged previously in Figure 7.12 and 7.13. The green rectangle encloses the area that was repeatedly imaged, which indicates no significant difference to the surrounding areas.

previous section (Figure 7.11) compared to that here (Figure 7.13 (a)). Steps of one monolayer thick were observed on both surfaces. The step edges on the former surface appeared to be much straighter than those on the latter surface. As the same AN source and solvent were used to prepare new solutions each time to form these crystals, the reason for this difference was unclear, but was not further investigated. It is suspected that over time there might have been a build up of impurity in the solvent, or possible degradation of AN, which could affect the crystallisation process at the interface between the mother liquor and the growing crystal surface.

The following mechanism, similar to that in Chapter 6, is proposed to explain the observations from the above continuous imaging study of AN surfaces:

1. Product formation initially occurs at sites of defects, including step edges and pits.
2. Product growth continues over time, drawing material from the surrounding flat terrace.
3. This depletes the material from the flat terrace regions, eventually causing steps to move and the associated terraces to shrink in size.
4. As the steps rearrange, new defect sites are created, initiating further reaction.
5. Steps 2 to 4 continue to occur, eventually spreading product growth across the surface

Investigating the effect of moisture on photoactivity of AN

In contrast to the topochemical postulate, the mechanism of AN photoreaction proposed above requires surface material to be mobile. The presence of moisture is suspected to be an important factor in affecting the surface mobility of AN surfaces, which in turn controls the photoreactivity occurring at defect sites. However, it is worth noting that humidity could also lead to the formation of ANQ, which will be further discussed in section 7.4.

To investigate the effect of humidity on the photoreaction, AN crystals were exposed to UV under two test conditions: one in dry conditions that was near to 0% RH, and another at ambient conditions. During the study, the measured room humidity ranged from 40 to 50% RH, which was a narrower range than the normal fluctuation of room humidity between 30 to 60% RH.

A continuous nitrogen gas flow was supplied to the chamber (Figure 7.6), and as the chamber was not sealed completely, the nitrogen gas gradually replaced the original volume of gas in the chamber, removing moisture. It is worth pointing out that the gas flow is expected to promote the sublimation of surface molecules both kinetically and thermodynamically. The air turbulence disturbs surface molecules which will more likely leave the surface. The continuous removal of sublimed molecules in the chamber shifts the thermodynamic equilibrium of the sublimation reaction towards the gas phase. Therefore, in order to minimize such effect, the nitrogen flow was kept to a minimum, just enough to maintain the RH of the chamber at less than 1%.

As it was expected that the transparent chamber wall could shield the sample from the UV light source, the sample was left in the set up for 24 hours to ensure enough time for the photoreaction to occur. The chamber was also used without nitrogen flow for the experiments conducted in ambient conditions to ensure equal UV exposure.

The samples were imaged by AFM before and after the 24-hour UV treatment (approximately 1440 min), which in between this period the imaging tip was withdrawn vertically from the surface, and sample remained in the set up. This allowed returning the tip to image the same area afterwards. A slight offset of the imaged area was expected due to creeping and bowing of the piezo unit before and after 24 hours. However, the position should not have deviated significantly, and certain features on the surface were used as reference points to map out the overlap area of imaging when available.

For the sample studied under dry conditions, the images before and after aging could be related by comparing the relative positions of the features observed on each image (Figure 7.15 (a) and (d)). Closeup images are shown in

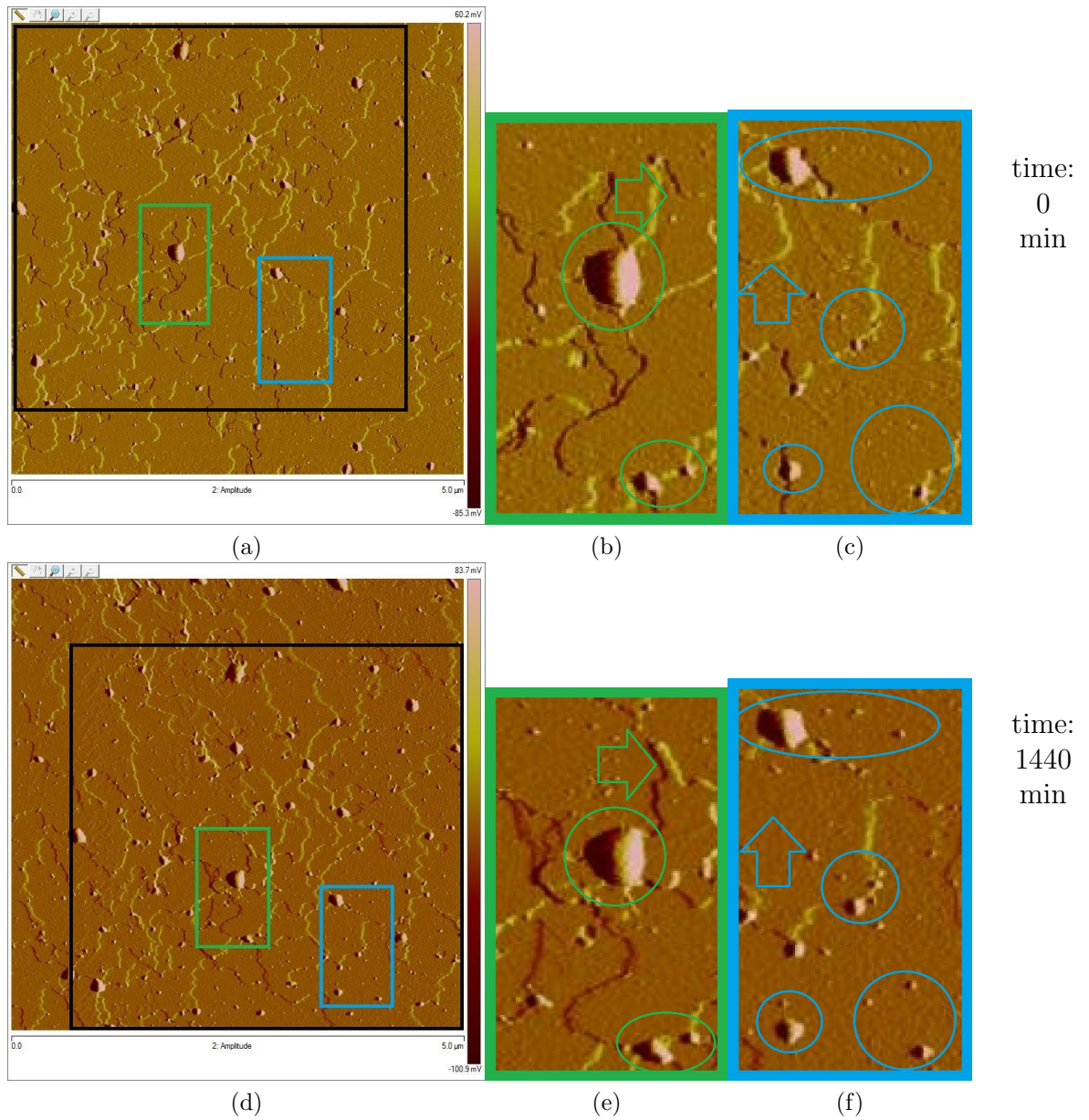


Figure 7.15: Amplitude profile of an AN (001) surface exposed to UV under dry conditions before (a – c) and after (d – f) 24 hours. The area of imaging was $5 \times 5 \mu\text{m}^2$ in (a, d), where the black rectangles enclose the same area that was imaged. (b, c) and (e, f) are close up images of the area enclosed by the green and blue rectangles respectively in (a, d). The circles indicate the features seen before and after 24 hours, while the arrows indicate the position where step rearrangement has occurred.

Figure 7.15 (b, c, e, f), where there was evidence of step rearrangement due to sublimation of AN molecules, and this reaction was further promoted under the continuous nitrogen gas flow. Some features were originally present before the aging period, and some features showed growth in size. However, the change in height for all the features was no more than 5 nm, which suggested that the surface reactivity was not significant.

For the sample studied under ambient conditions, approximately the same area of the crystal was imaged before and after 24 hours of exposure to UV (Figure 7.16 (a) and (d)). The images showed that the original features expanded laterally by a significant amount (Figure 7.16 (b, c, e, f)). Cross section analysis showed that these features had grown in height by over 15 nm according to a cross section analysis. Several new features emerged after the aging period, and step rearrangement was observed (Figure 7.16 (c) and (f)), which is possibly due to both the sublimation and the growth of features drawing away material from the steps.

Overall the growth in both the number and size of features after aging in ambient humidity was much more significant than for the sample studied in dry conditions. Therefore, this set of experiments suggest that humidity is required for any features to grow on the surface. It is also postulated that the vapour of other organic solvents will have the same effect on the surface photoreaction as moisture.

7.4 Dianthracene or anthraquinone?

Up to this point, no comment has been made on the chemical composition of the features being formed at defect sites on the surface. As these features seem to have initially grown at specific sites, the reaction involved is not homogeneous throughout the surface. This supports the idea that such surface features correspond to the photodimerisation product, as the reaction is only expected to occur when pairs of molecules are distorted from their original positions in the crystal structure. While surface relaxation on the terrace can displace the outermost molecules (Figure 7.17 (a)), the degree of such displacement is likely to be even greater at steps (Figure 7.17 (b)). As the terrace did not show any product growth, it is possible that surface relaxation on the terrace was not sufficient to displace the position of AN molecules enough and create the correct orientation for dimerisation, while the greater extent of relaxation at the step edges was enough for photodimerisation to be possible.

However, as it was observed that moisture is required for the formation of

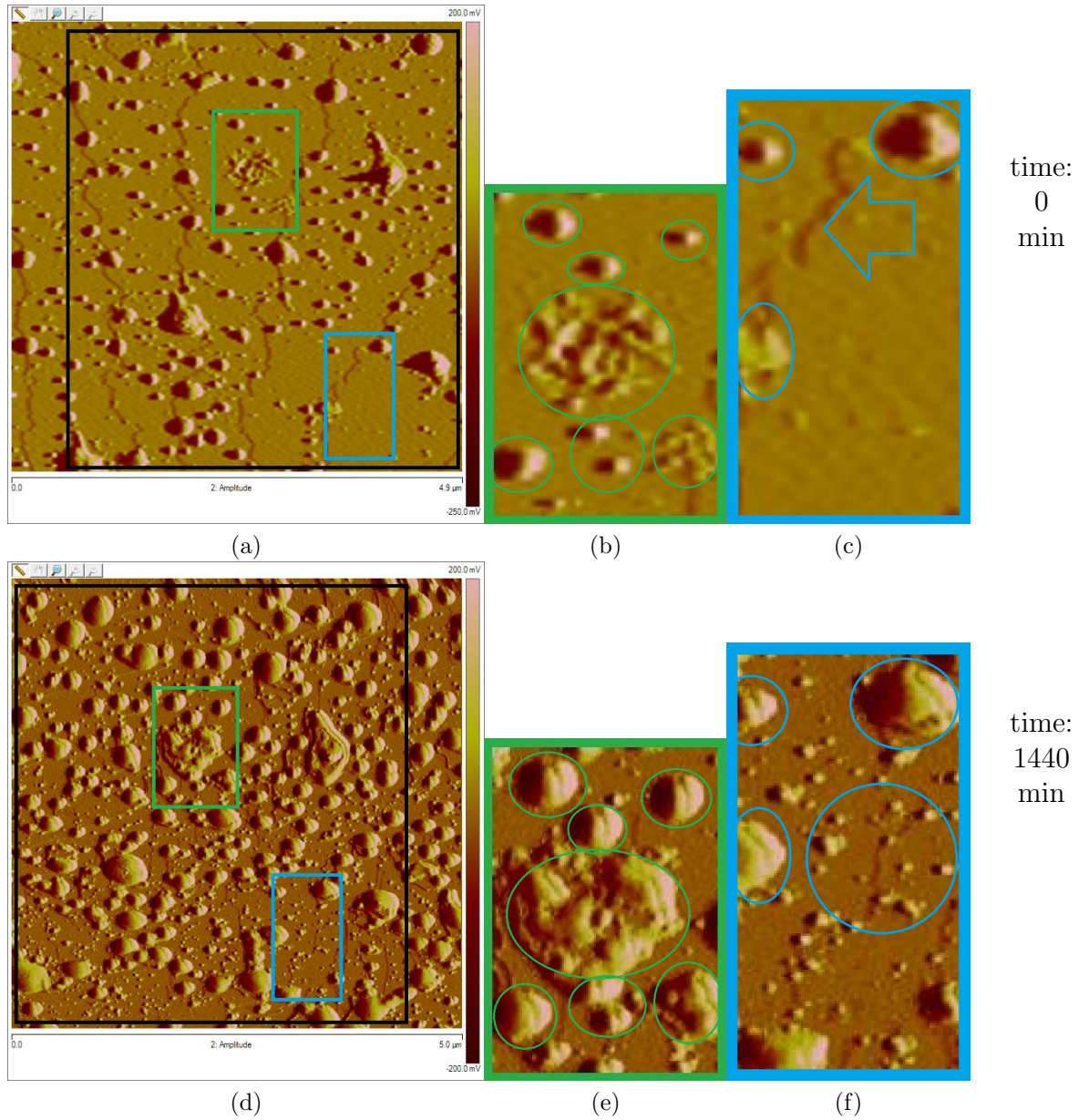


Figure 7.16: Amplitude profile of an AN (001) surface exposed to UV under ambient humidity before (a – c) and after (d – f) 24 hours. The area of imaging was $5 \times 5 \mu\text{m}^2$ in (a, d), where the black rectangles enclose the same area that was imaged. (b, c) and (e, f) are close up images of the area enclosed by the green and blue rectangles respectively in (a, d). The circles indicate the features seen before and after 24 hours, showing significant growth during this period, while the arrow indicates the initial position of a step that had migrated.

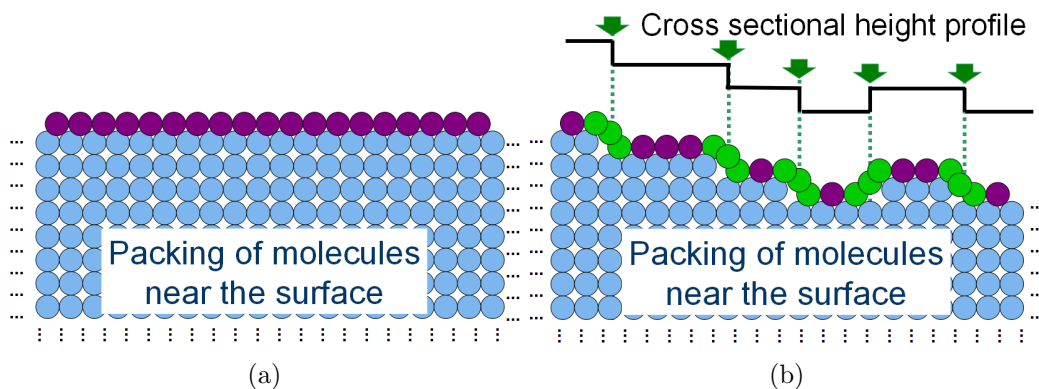
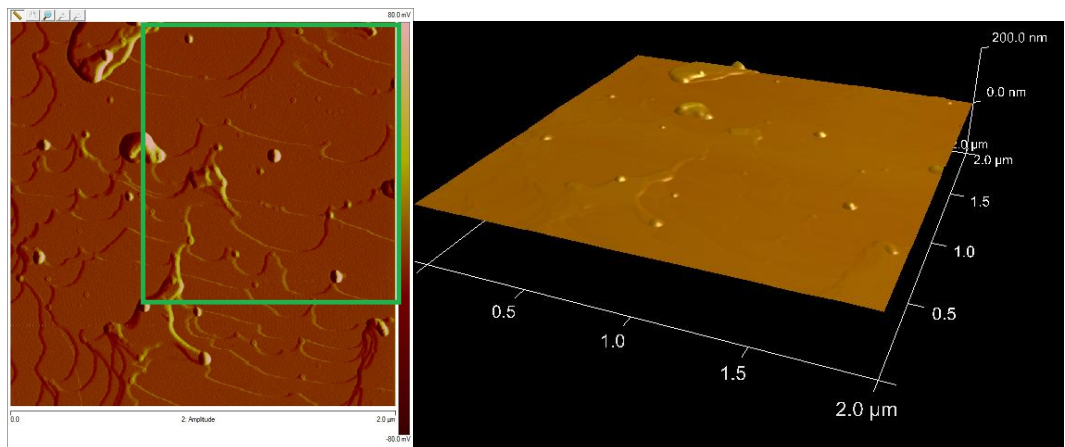


Figure 7.17: Schematic 2-D illustration of the surface relaxation (a) on a flat crystal surface; (b) at step or pit features. The circles represent AN molecules, where the molecules in the bulk crystal are coloured in blue, while the relaxed surface molecules on the (001) face of AN are coloured in purple. The green circles represent the molecules near the edge of the step, which are distorted to the greatest extent from their original position in the perfect lattice, therefore making these sites the most reactive sites, as indicated by the arrows.

products, there is a possibility that the surface AN molecules oxidised to yield ANQ instead of the dimer [197, 198]. As the photo-oxidation of AN to ANQ only requires AN molecules to be exposed to oxygen and humidity, it is not a topochemical reaction, *i.e.* AN molecules do not have to be in close proximity with one another to undergo photoreaction. Therefore, it is likely that the formation of ANQ is not limited to sites of defects, but occurs across the entire surface, as the outermost molecules are in contact with oxygen and moisture.

Another continuous imaging study of the photoreaction of a different AN crystal under similar conditions (room humidity and temperature) is shown in Figure 7.18. While new features were growing at localised sites (Figure 7.18 (c), (d)), which agreed with the proposed photodimerisation mechanism, a secondary product emerged after approximately 5 hours of irradiation, which was not limited to any particular sites (Figure 7.18 (e) to (l)). This secondary growth covered the entire surface, converting both the regions of flat terraces as well as the localised growing features. Later AFM images did not show any further change on the surface, up to a period of 10 hours. An image of a larger area was recorded afterwards, which showed no significant difference between the continuously imaged area and the surrounding areas, indicating insignificant tip influence on the surface (Figure 7.19).

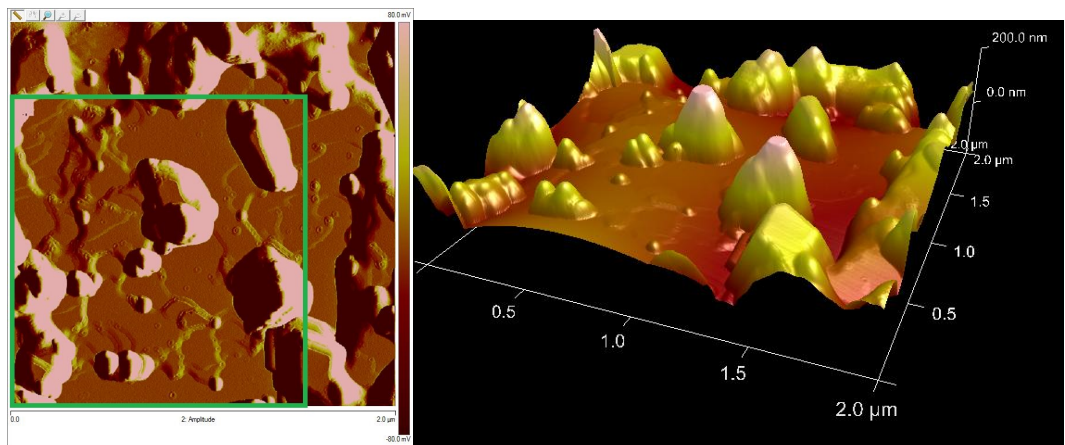
Bulk techniques such as PXRD and ATR-FTIR were not able to show any changes at the surface, and there were no other techniques to chemically characterise the surface. Therefore, it can only be postulated that while the features growing at localised sites correspond to the photodimerisation of AN due to its topochemical nature, the secondary surface change corresponds to



time:
0
min

(a)

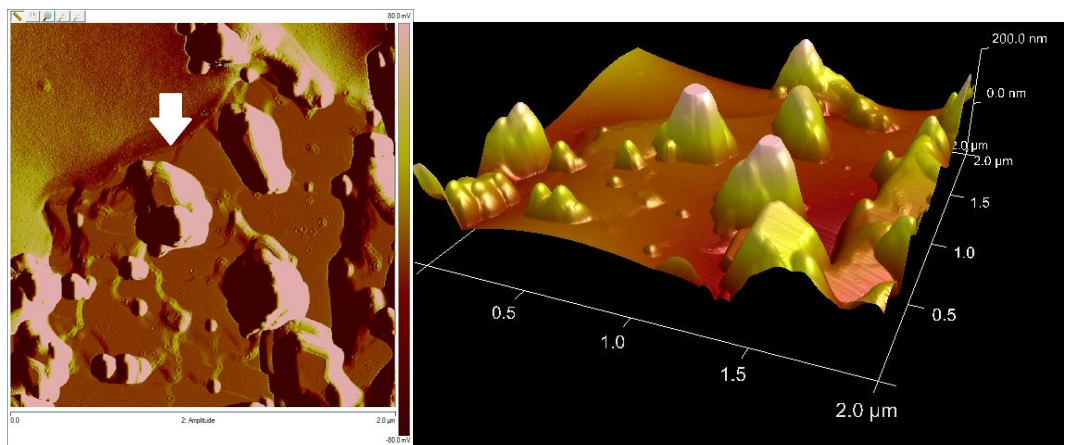
(b)



time:
270
min

(c)

(d)



time:
280
min

(e)

(f)

Figure 7.18: Amplitude profile ((a), (c), (e)) and 3-D height profile ((b), (d), (f)) of an AN (001) surface exposed to UV for 0 min ((a), (b)), 270 min ((c), (d)), and 280 min ((e), (f)). The imaging area is $2 \times 2 \mu\text{m}^2$ for all images.

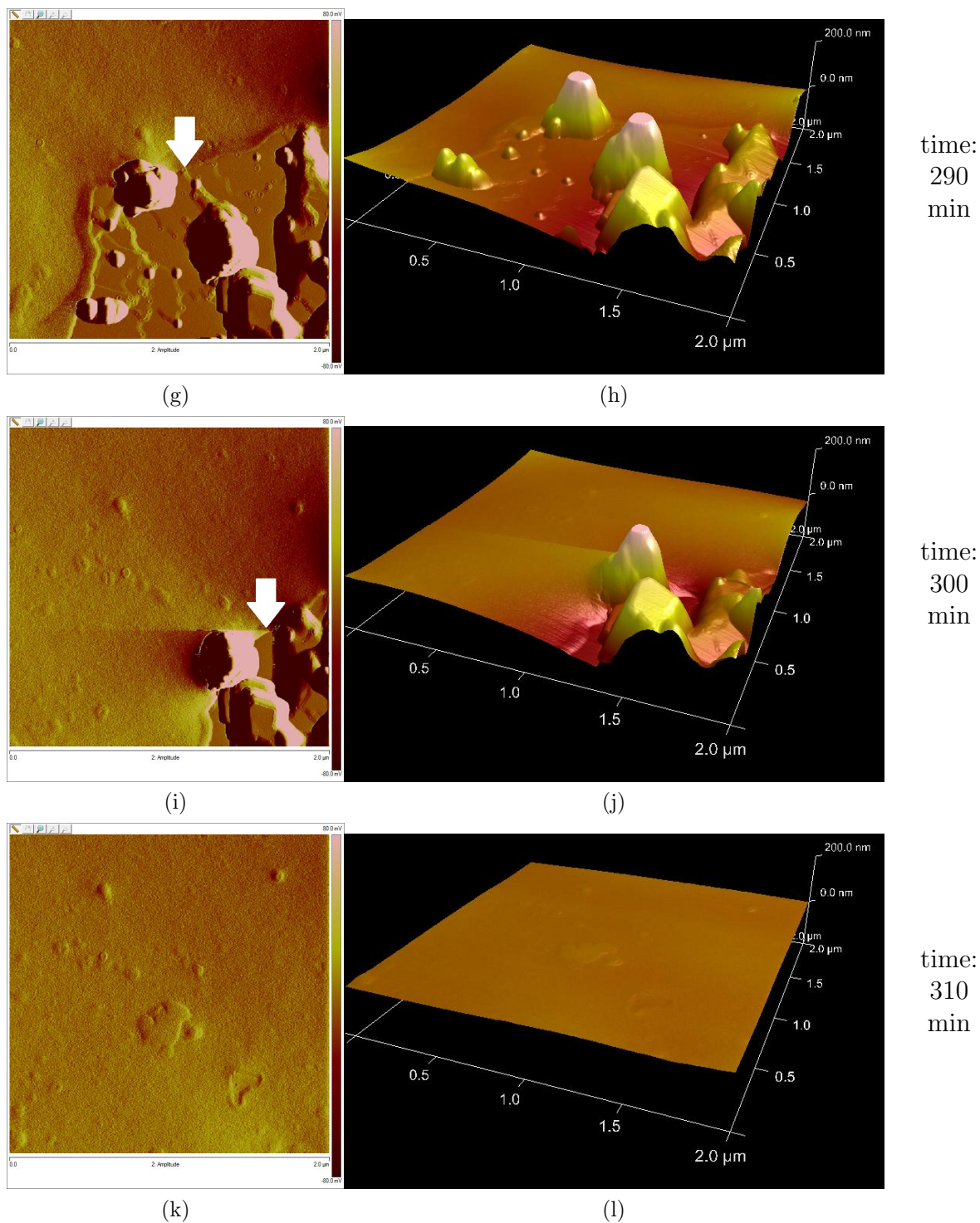


Figure 7.18 (cont.): Amplitude profile ((g), (i), (k)) and 3D height profile ((h), (j), (l)) of an AN (001) surface exposed to UV for 290 min ((g), (h)), 300 min ((i), (j)), and 310 min ((k), (l)). The white arrow indicates the secondary product growth propagating across the whole surface. The imaging area is $2 \times 2 \mu\text{m}^2$ for all images.

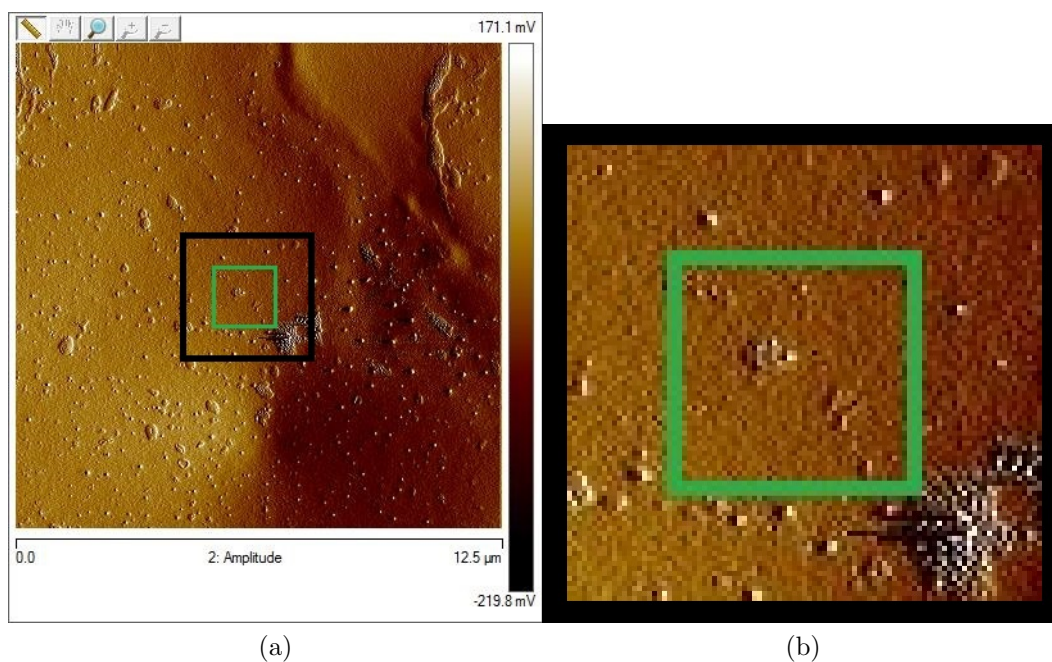


Figure 7.19: (a) Amplitude profile of a larger area ($12.5 \times 12.5 \mu\text{m}^2$) after the continuous imaging period; (b) a closeup image of the area of the black rectangle in (a). The green rectangles denote the area that was continuously imaged ($2 \times 2 \mu\text{m}^2$), which showed no significant difference to the rest of the surface, indicating insignificant tip effect.

the photo-oxidation of AN to ANQ, or the formation of an amorphous phase, as both reactions are not topochemical.

7.5 Inconsistent rate of reaction at sites of defects

There was no accurate method in determining the amount of product formed, as the features grew both laterally and vertically on the surface. Moreover, the growth about the lateral plane was often not uniform. Attempts to quantify the rate of product formation at defect sites on AN crystals were made using the growth in height of the features as indicator. For each of the UV studies of AN (001) at ambient humidity so far in this chapter (Figure 7.11, 7.16, 7.13, 7.18), five features that showed the most significant growth in height were identified.

One of these studies showed a much slower growth compared to the others (Figure 7.16 (c)). This was because the study involved a humidity chamber which was expected to partially shield the sample from the UV source, hence lowering its reactivity. For the other three studies, the height growth of features varied from 4 nm/hour to over 20 nm/hour (Figure 7.13 (p) and 7.18 (l)), which was still a very wide range. Although these were rough quantitative estimations, a qualitative inspection of the images recorded on these samples further

supports the scattered growth rate of the features on AN crystal surfaces.

The reason for the difference in growth rates is yet to be determined. It is believed that the UV photon flux was constant as the UV light source was kept at a fixed distance to the sample. Fluctuations in temperature and room humidity is one of the suspected factors that can affect the rate of product formation. Room temperature and RH ranged between 18°C to 23°C, and 30% to 60% respectively. The rate of sublimation of surface AN molecules is expected to be higher at elevated temperatures, which would enhance step rearrangement on the crystal surface, creating more initial product growth sites. Variation in RH can affect AN surfaces in two ways: firstly, by mobilising surface molecules which allow surface rearrangement for product growth at localised defect sites, and secondly, by providing moisture for the photo-oxidation reaction, promoting the formation of ANQ or amorphous content.

7.6 Chapter Conclusion

In this chapter, the surface photoreactivity of AN was investigated by AFM. The findings are as follows:

- Photoreaction on AN crystal surfaces is more likely to occur at defect sites such as steps and pits than the rest of the surface.
- This localised product formation is suggested to be the photodimerisation product, diAN, as this reaction requires AN molecules to be distorted from their original position in a perfect crystal.
- A mechanism of the solid-state photodimerisation was proposed, which involves the rearrangement of surface molecules.
- Surface rearrangement was shown to be possible only in the presence of moisture, suggesting that the presence of solvent vapour is required to mobilise surface molecules for product growth to occur.
- A non-topochemical secondary product growth was observed to propagate across the entire surface and was not limited to any defect sites. This was postulated to be the formation of either an amorphous phase or a ANQ (produced from the photo-oxidation reaction producing AN).

Although the topochemical postulate does not predict AN to photodimerise, the results in this chapter have suggested that the “minimum movement of molecules” of the postulate does not apply to surface molecules, as they can

be more mobile than the molecules in the bulk crystal. Thus, the proposed surface mechanism based on molecular movement allows the explanation of why this reaction occurs. Future work should focus on chemical analysis of the observed surface products, using analytical techniques such as XPS, or AFM combined with Raman spectroscopy. It should also consider how AFM or other techniques might be used to study the migration of the reactive front into the crystal as the reaction proceeds.

Chapter 8

Conclusions

In this thesis, three main topics were covered. The first one was evaluating AFM as a technique to study organic crystals. Two aspects were identified that influenced the surface of these crystals, namely the natural sublimation of surface molecules at room temperature, and the interaction between the AFM tip and the sample surface. While a correlation was found between the likelihood of natural sublimation and the sublimation enthalpy of each material, the influence on the surface by the AFM tip was found to be unpredictable. It was suggested that an image of an enlarged area should be recorded after any continuous imaging studies in order to determine whether the surface was influenced by the tip.

The second topic was on the degradation of pharmaceutical solids, where the solid-state hydrolysis of aspirin (ASA) crystals in the presence of humidity was the model system that was studied by AFM. The surface behaviour of ASA (001) varied under different RH levels. In the absence of humidity, no changes were observed on the ASA surface, indicating that the surface is stable under dry conditions. For the surface exposed to moderate RH, formation of tall features were observed, which is likely related to the hydrolysis of ASA molecules to salicylic acid (SA). In this case the reaction on the surface is not homogeneous, as the features emerged at specific locations, which are believed to be original sites of defects. A mechanism was proposed based on transportation of surface molecules to these reactive sites that propagate the extent of the solid-state reaction, where moisture acts as both a chemical reagent for the hydrolysis reaction, and a medium to mobilise surface molecules.

For ASA stored under high RH, no new growing features were observed at the surface. There was a noticeable change in step height, which suggests that the whole surface material might be a different composition to the original. It is possible that hydrolysis has occurred, with a new layer of SA forming

across the entire surface, suggesting a more homogeneous reaction than the surface stored at moderate RH. The difference in observations between the two humidity levels might be due to the amount of water adsorbed onto the surfaces at different RHs, which in turn affects the amount of surface molecules dissolved, as well as the dissolution of such tall features.

Another interesting observation was the exposure of ASA (001) to toluene vapour, as similar growth of tall features were observed. Based on a solubility comparison between SA and ASA in toluene and water, it is suggested that such tall features are a result of dissolution and recrystallisation of ASA surface molecules. Molecules are believed to preferentially deposit at growing features emerging from sites of defects, which are kinetically more accessible than other parts of the surface. This phenomenon is yet to be reported, and may have potential applications in controlling the surface roughness of samples by exposure to organic vapour, which in turn may allow better control over solid-state reactivity.

In the last topic of the thesis, the photoreactivity of anthracene (AN) was investigated. As the photodimerisation of crystalline AN is not predicted to occur according to the well known topochemical postulate, this challenges one of the fundamental concepts of crystal engineering. After exposure to UV, no changes in the bulk were detected by PXRD and ATR-FTIR, confirming that the photoreaction was a surface phenomenon. Continuous AFM imaging indicated significant changes on AN (001) originating at defect sites such as steps and pits. This is believed to be a result of the photodimerisation, as the reaction can only proceed with AN molecules displaced from their original position in a perfect crystal. A mechanism similar to that describing the hydrolysis of ASA at moderate RH was applied to this study, involving the rearrangement of surface molecule which was possible in the presence of moisture. A non-topochemical secondary product growth was also observed to propagate through the entire surface which was not limited to defect sites. This was suggested to be either the formation of an amorphous phase or anthraquinone (a photo-oxidation product of AN). These results suggested that the “minimum movement of molecules” of the postulate does not apply to surface molecules, as they can be more mobile than the molecules in the bulk crystal.

To the best of our knowledge, this is the first report that has investigated the role of humidity and surface defects on the solid-state reactivity of organic crystals. Evidence has suggested that the reactivity of a crystal surface can depend on the amount of defects (steps and pits) present initially, as these are often kinetic sites of higher energy than other parts of the surface. Moisture, or

other solvent vapours also play an important role that enables surface molecules to be transported to these reactive sites, allowing further propagation of the reaction. A few future research ideas are suggested below:

1. Study the surface response of ASA (100). A comparison of this to the response of ASA (001) will provide more insight towards the degree of anisotropy between the two faces.
2. As two different surface responses were observed when storing ASA (001) at 50% and 98% RH, studies of ASA (001) stored at RH levels in between these two conditions will be useful in determining the transition of the hydrolysis mechanism from one to another as the RH is changed.
3. Surface studies of organic crystals that follow the topochemical postulate to undergo photoreaction, *e.g.* cinnamic acid. It will be interesting to see how the surface changes upon exposure to UV light for such crystal surfaces, whether the reaction will be homogeneous, or exhibit heterogeneous surface photoreaction which is similar to that found on AN crystal surfaces.
4. As solid-state reactivity is likely affected by the number of defects present on the surface, further investigation in the origin of defects on the surface are suggested. With a better understanding of defects, this may allow a more accurate estimation, and eventually better control over the amount of defects present on a crystal surface. This would be extremely useful in various industries, such as maintaining homogeneity of products, or fine-tuning the reactivity of solids by changing the number of defects present.

Based on the results in this report, AFM was demonstrated to be a powerful tool in studying organic crystal surfaces. The main limitation of this technique is the lack of chemical characterisation of the surfaces that are studied, and other common techniques are often not sensitive enough to detect the changes observed by AFM. Future work involving better chemical analysis techniques is recommended, especially the combination of AFM with Raman spectroscopy.

Chapter 9

Bibliography

- [1] Schmidt, G. M. J. Photodimerization in the solid state. *Pure App. Chem.* **27**, 647–678 (1971).
- [2] Vishweshwar, P., McMahon, J. A., Bis, J. A. & Zaworotko, M. J. Pharmaceutical Co-Crystals. *J. Pharm. Sci.* **95**, 499–516 (2006).
- [3] Desiraju, G. R. Supramolecular Synthons in Crystal Engineering - A New Organic Synthesis. *Angew. Chem. Int. Ed.* **34**, 2311–2327 (1995).
- [4] Tsuzuki, S., Honda, K. & Azumi, R. Model chemistry calculations of thiophene dimer interactions: origin of pi-stacking. *J. Am. Chem. Soc.* **124**, 12200–9 (2002).
- [5] Almarsson, O. & Zaworotko, M. J. Crystal engineering of the composition of pharmaceutical phases. Do pharmaceutical co-crystals represent a new path to improved medicines? *Chem. Commun.* 1889–96 (2004).
- [6] Desiraju, G. R. Crystal engineering: a holistic view. *Angew. Chem. Int. Ed.* **46**, 8342–56 (2007).
- [7] Braga, D. Crystal engineering, where from? Where to? *Chem. Commun.* 2751–4 (2003).
- [8] Nehm, S. J., Rodríguez-Spong, B. & Rodríguez-Hornedo, N. Phase Solubility Diagrams of Cocrystals Are Explained by Solubility Product and Solution Complexation. *Cryst. Growth Des.* **6**, 592–600 (2006).
- [9] Bethune, S. J., Huang, N., Jayasankar, A. & Rodriguez-Hornedo, N. Understanding and Predicting the Effect of Cocrystal Components and pH on Cocrystal Solubility. *Cryst. Growth Des.* **9**, 3976–3988 (2009).

- [10] Trask, A. V., Haynes, D. A., Motherwell, W. D. S. & Jones, W. Screening for crystalline salts via mechanochemistry. *Chem. Commun.* 51–3 (2006).
- [11] Bernstein, J., Davey, R. J. & Henck, J.-O. Concomitant Polymorphs. *Angew. Chem. Int. Ed.* **38**, 3440–3461 (1999).
- [12] Schultheiss, N. & Newman, A. W. Pharmaceutical Cocrystals and Their Physicochemical Properties. *Cryst. Growth Des.* **9**, 2950–2967 (2009).
- [13] Good, D. J. & Rodríguez-Hornedo, N. Solubility Advantage of Pharmaceutical Cocrystals. *Cryst. Growth Des.* **9**, 2252–2264 (2009).
- [14] Karki, S., Friscic, T. & Jones, W. Control and Interconversion of Cocrystal Stoichiometry in Grinding: Stepwise Mechanism for the Formation of a Hydrogen-Bonded Cocrystal. *CrystEngComm* **11**, 470–481 (2009).
- [15] Kobayashi, Y., Ito, S., Itai, S. & Yamamoto, K. Physicochemical properties and bioavailability of carbamazepine polymorphs and dihydrate. *Int. J. Pharm.* **193**, 137–46 (2000).
- [16] Miyazaki, T., Sivaprakasam, K., Tantry, J. & Suryanarayanan, R. Physical Characterization of Dibasic Calcium Phosphate Dihydrate and Anhydrate. *J. Pharm. Sci.* **98**, 905 (2009).
- [17] Hancock, B. C. & Parks, M. What is the true solubility advantage for amorphous pharmaceuticals? *Pharm. Res.* **17**, 397–404 (2000).
- [18] Lucas, P., Anderson, K. & Staniforth, J. N. Protein Deposition from Dry Powder Inhalers: Fine Particle Multiplets as Performance Modifiers. *Pharm. Res.* **15**, 562–569 (1998).
- [19] Hickey, A. J. Lung Deposition and Clearance of Pharmaceutical Aerosols: What Can Be Learned from Inhalation Toxicology and Industrial Hygiene? *Aerosol Sci. Tech.* **18**, 290–304 (1993).
- [20] Bauer, J. *et al.* Ritonavir: an extraordinary example of conformational polymorphism. *Pharm. Res.* **18**, 859–66 (2001).
- [21] Kaialy, W. *et al.* Characterisation and deposition studies of recrystallised lactose from binary mixtures of ethanol/butanol for improved drug delivery from dry powder inhalers. *AAPS J.* **13**, 30–43 (2011).
- [22] Begat, P., Young, P. M., Edge, S., Kaerger, J. S. & Price, R. The effect of mechanical processing on surface stability of pharmaceutical powders:

- visualization by atomic force microscopy. *J. Pharm. Sci.* **92**, 611–20 (2003).
- [23] Descamps, M., Willart, J. F., Dudognon, E. & Caron, V. Transformation of Pharmaceutical Compounds upon Milling and Comilling : The Role of Tg. *J. Pharm. Sci.* **96**, 1398–1407 (2007).
- [24] Pirttimaki, J., Laine, E., Ketolainen, J. & Paronen, P. Effects of grinding and compression on crystal structure of anhydrous caffeine. *Int. J. Pharm.* **95**, 93–99 (1993).
- [25] Binnig, G., Quate, C. F. & Gerber, C. Atomic Force Microscope. *Phys. Rev. Lett.* **56**, 930–934 (1986).
- [26] Chow, E. H. H., Bučar, D.-K. & Jones, W. New opportunities in crystal engineering—the role of atomic force microscopy in studies of molecular crystals. *Chem. Commun.* **48**, 9210–26 (2012).
- [27] Meyer, G. & Amer, N. M. Novel optical approach to atomic force microscopy. *Appl. Phys. Lett.* **53**, 1045 (1988).
- [28] Lal, R., Ramachandran, S. & Arnsdorf, M. F. Multidimensional atomic force microscopy: a versatile novel technology for nanopharmacology research. *AAPS J.* **12**, 716–28 (2010).
- [29] Johnson, K. L., Kendall, K. & Roberts, A. D. Surface Energy and the Contact of Elastic Solids. *Proc. R. Soc. Lond. A Mat.* **324**, 301–313 (1971).
- [30] Derjaguin, B. V., Muller, V. M. & Toporov, Y. P. Effect of contact deformations on the adhesion of particles. *J. Colloid Interface Sci.* **53**, 314–326 (1975).
- [31] Martin, Y., Williams, C. C. & Wickramasinghe, H. K. Atomic force microscope force mapping and profiling on a sub 100-Å scale. *J. Appl. Phys.* **61**, 4723 (1987).
- [32] Cleveland, J. P., Anczykowski, B., Schmid, A. E. & Elings, V. B. Energy dissipation in tapping-mode atomic force microscopy. *Appl. Phys. Lett.* **72**, 2613 (1998).
- [33] Zhao, Y., Cheng, Q., Qian, M. & Cantrell, J. H. Phase image contrast mechanism in intermittent contact atomic force microscopy. *J. Appl. Phys.* **108**, 094311 (2010).

- [34] Ye, Z. & Zhao, X. Phase imaging atomic force microscopy in the characterization of biomaterials. *J. Microsc.* **238**, 27–35 (2010).
- [35] Zhong, Q., Inniss, D., Kjoller, K. & Elings, V. B. Fractured polymer/silica fiber surface studied by tapping mode atomic force microscopy. *Surf. Sci. Lett.* **290**, L688–L692 (1993).
- [36] Gross, L., Mohn, F., Moll, N., Liljeroth, P. & Meyer, G. The chemical structure of a molecule resolved by atomic force microscopy. *Science (New York, N.Y.)* **325**, 1110–4 (2009).
- [37] Giessibl, F. J. Advances in atomic force microscopy. *Rev. Mod. Phys.* **75**, 949–983 (2003).
- [38] Ward, M. D. Bulk Crystals to Surfaces : Combining X-ray Diffraction and Atomic Force Microscopy to Probe the Structure and Formation of Crystal Interfaces to Bulk Crystal Structures. *Chem. Rev.* **101**, 1697–1726 (2001).
- [39] Edwardson, J. M. & Henderson, R. M. Atomic force microscopy and drug discovery. *Drug discovery today* **9**, 64–71 (2004).
- [40] Bunker, M., Davies, M. & Roberts, C. Towards screening of inhalation formulations: measuring interactions with AFM. *Expert Opin. Drug Delivery* **2**, 613–624 (2005).
- [41] Hinterdorfer, P. & Dufrêne, Y. F. Detection and localization of single molecular recognition events using atomic force microscopy. *Nat. Methods* **3**, 347 (2006).
- [42] Turner, Y. T. A., Roberts, C. J. & Davies, M. C. Scanning probe microscopy in the field of drug delivery. *Adv. Drug Delivery Rev.* **59**, 1453–73 (2007).
- [43] Oliver, R. A. Advances in AFM for the electrical characterization of semiconductors. *Rep. Prog. Phys.* **71**, 076501 (2008).
- [44] Rosa, L. G. & Liang, J. Atomic force microscope nanolithography: dippen, nanoshaving, nanografting, tapping mode, electrochemical and thermal nanolithography. *J. Phys.: Condens. Matter* **21**, 483001 (2009).
- [45] Moreno Flores, S. & Toca-Herrera, J. L. The new future of scanning probe microscopy: Combining atomic force microscopy with other

- surface-sensitive techniques, optical microscopy and fluorescence techniques. *Nanoscale* **1**, 40–9 (2009).
- [46] Lauritsen, J. V. & Reichling, M. Atomic resolution non-contact atomic force microscopy of clean metal oxide surfaces. *J. Phys.: Condens. Matter* **22**, 263001 (2010).
- [47] Rice, J. H. Nanoscale optical imaging by atomic force infrared microscopy. *Nanoscale* **2**, 660–7 (2010).
- [48] Barth, C., Foster, A. S., Henry, C. R. & Shluger, A. L. Recent Trends in Surface Characterization and Chemistry with High-Resolution Scanning Force Methods. *Adv. Mater.* **23**, 477–501 (2011).
- [49] Varughese, S., Kiran, M. S. R. N., Ramamurty, U. & Desiraju, G. R. Nanoindentation in Crystal Engineering: Quantifying Mechanical Properties of Molecular Crystals. *Angew. Chem. Int. Ed.* **52**, 2701–2712 (2013).
- [50] Ward, M. D. Materials science. Snapshots of crystal growth. *Science* **308**, 1566–7 (2005).
- [51] Ristic, R. I., Sherwood, J. & Shripathi, T. The influence of tensile strain on the growth of crystals of potash alum and sodium nitrate. *J. Cryst. Growth* **179**, 194–204 (1997).
- [52] Weisenhorn, A. L., Hansma, P. K., Albrecht, T. R. & Quate, C. F. Forces in atomic force microscopy in air and water. *Appl. Phys. Lett.* **54**, 2651 (1989).
- [53] Musumeci, D. & Ward, M. D. Elucidation of the crystal growth mechanism of melamine-cyanuric acid by using real time in situ atomic force microscopy. *CrystEngComm* **13**, 1067–1069 (2011).
- [54] Lam, C.-W. *et al.* Diagnosis and spectrum of melamine-related renal disease: plausible mechanism of stone formation in humans. *Clin. Chim. Acta* **402**, 150–5 (2009).
- [55] Brown, C. A. *et al.* Outbreaks of Renal Failure Associated with Melamine and Cyanuric Acid in Dogs and Cats in 2004 and 2007. *J. Vet. Diagn. Invest.* **19**, 525–531 (2007).

- [56] Cuppen, H. M., Graswinckel, W. S. & Meekes, H. Screw Dislocations on Polycenes : A Requirement for Crystallization. *Cryst. Growth Des.* **4**, 1351–1357 (2004).
- [57] Choubey, A., Kwon, O.-p., Jazbinsek, M. & Gunter, P. High-Quality Organic Single Crystalline Thin Films for Nonlinear Optical Applications by Vapor Growth. *Cryst. Growth Des.* **7**, 402–405 (2007).
- [58] Fritz, S. E. *et al.* Thin Film Transistors Based on Alkylphenyl Quaterthiophenes: Structure and Electrical Transport Properties. *Chem. Mater.* **19**, 1355–1361 (2007).
- [59] Price, R. & Young, P. M. Visualization of the crystallization of lactose from the amorphous state. *J. Pharm. Sci.* **93**, 155–64 (2004).
- [60] Chen, D., Haugstad, G., Li, Z. J. & Suryanarayanan, R. Water Sorption Induced Transformations in Crystalline Solid Surfaces : Characterization by Atomic Force Microscopy. *J. Pharm. Sci.* **99**, 4032–4041 (2010).
- [61] Vekilov, P. G. What Determines the Rate of Growth of Crystals from Solution? *Cryst. Growth Des.* **7**, 2796–2810 (2007).
- [62] Sleutel, M. *et al.* The Role of Surface Diffusion in the Growth Mechanism of Triosephosphate Isomerase Crystals. *Cryst. Growth Des.* **8**, 1173–1180 (2008).
- [63] Hondoh, H. & Nakada, T. Effect of Protein Molecular Anisotropy on Crystal Growth. *Cryst. Growth Des.* **8**, 4262–4267 (2008).
- [64] Kaupp, G. Solid-state photochemistry: new approaches based on new mechanistic insights. *Int. J. Photoenergy* **3**, 55–62 (2001).
- [65] Kaupp, G. Solid-state molecular syntheses: complete reactions without auxiliaries based on the new solid-state mechanism. *CrystEngComm* **5**, 117 (2003).
- [66] Kaupp, G. Waste-free synthesis and production all across chemistry with the benefit of self-assembled crystal packings. *J. Phys. Org. Chem.* **21**, 630–643 (2008).
- [67] Yu, L. Polymorphism in molecular solids: an extraordinary system of red, orange, and yellow crystals. *Acc. Chem. Res.* **43**, 1257–66 (2010).

- [68] Hillier, A. C. & Ward, M. D. Atomic Force Microscopy of the Electrochemical Nucleation and Growth of Molecular Crystals. *Science* (1994).
- [69] Mitchell, C. A., Yu, L. & Ward, M. D. Selective nucleation and discovery of organic polymorphs through epitaxy with single crystal substrates. *J. Am. Chem. Soc.* **123**, 10830–9 (2001).
- [70] Leunissen, M. E., Graswinckel, W. S., van Enkevort, W. J. P. & Vlieg, E. Epitaxial Nucleation and Growth of n-Alkane Crystals on Graphite (0001). *Cryst. Growth Des.* (2004).
- [71] Greene, J. E. *Handbook of Crystal Growth* (Elsevier, Amsterdam, 1993).
- [72] Kishi, Y. & Matsuoka, M. Phenomena and Kinetics of Solid-State Polymorphic Transition of Caffeine. *Cryst. Growth Des.* **10**, 2916–2920 (2010).
- [73] Matsuo, K. & Matsuoka, M. Kinetics of Solid State Polymorphic Transition of Caffeine. *J. Chem. Eng. Jpn.* **40**, 468–472 (2007).
- [74] Jones, M. D., Beezer, A. E. & Buckton, G. Determination of Outer Layer and Bulk Dehydration Kinetics of Trehalose Dihydrate Using Atomic Force Microscopy, Gravimetric Vapour Sorption and Near Infrared Spectroscopy. *J. Pharm. Sci.* **97**, 4404–4415 (2008).
- [75] Sharp, J. H., Brindley, G. W. & Narahari Achar, B. N. Numerical Data for Some Commonly Used Solid State Reaction Equations. *J. Am. Ceram. Soc.* **49**, 379–82 (1966).
- [76] Rimer, J. D. *et al.* Crystal growth inhibitors for the prevention of L-cystine kidney stones through molecular design. *Science* **330**, 337–41 (2010).
- [77] Mahlin, D., Berggren, J., Alderborn, G. & Engström, S. Moisture-induced surface crystallization of spray-dried amorphous lactose particles studied by atomic force microscopy. *J. Pharm. Sci.* **93**, 29–37 (2004).
- [78] Mahlin, D., Berggren, J., Gelius, U., Engström, S. & Alderborn, G. The influence of PVP incorporation on moisture-induced surface crystallization of amorphous spray-dried lactose particles. *Int. J. Pharm.* **321**, 78–85 (2006).
- [79] Weuts, I. *et al.* Physicochemical Properties of the Amorphous Drug, Cast Films, and Spray Dried Powders to Predict Formulation Probability of

- Success for Solid Dispersions : Etravirine. *J. Pharm. Sci.* **100**, 260–274 (2011).
- [80] Thompson, C., Davies, M. C., Roberts, C. J., Tendler, S. J. B. & Wilkinson, M. J. The effects of additives on the growth and morphology of paracetamol (acetaminophen) crystals. *Int. J. Pharm.* **280**, 137–50 (2004).
- [81] Keel, T. R., Thompson, C., Davies, M. C., Tendler, S. J. B. & Roberts, C. J. AFM studies of the crystallization and habit modification of an excipient material, adipic acid. *Int. J. Pharm.* **280**, 185–98 (2004).
- [82] Cassidy, A. M. C., Gardner, C. E. & Jones, W. Following the surface response of caffeine cocrystals to controlled humidity storage by atomic force microscopy. *Int. J. Pharm.* **379**, 59–66 (2009).
- [83] Trask, A. V., Motherwell, W. D. S. & Jones, W. Pharmaceutical Cocrystallization: Engineering a Remedy for Caffeine Hydration. *Cryst. Growth Des.* **5**, 1013–1021 (2005).
- [84] Kiang, Y.-H. *et al.* Crystal structure and surface properties of an investigational drug—a case study. *Int. J. Pharm.* **280**, 17–26 (2004).
- [85] Sonwai, S. & Rousseau, D. Fat Crystal Growth and Microstructural Evolution in Industrial Milk Chocolate. *Cryst. Growth Des.* **9**, 3165–3174 (2008).
- [86] Chew, C. M., Ristic, R. I., Dennehy, R. D. & De Yoreo, J. J. Crystallization of Paracetamol under Oscillatory Flow Mixing Conditions. *Cryst. Growth Des.* **4**, 1045–1052 (2004).
- [87] Chernov, A. A. Formation of crystals in solutions. *Contemp. Phys.* **30**, 251–276 (1989).
- [88] Kim, K., Centrone, A., Hatton, T. A. & Myerson, A. S. Polymorphism control of nanosized glycine crystals on engineered surfaces. *CrystEngComm* **13**, 1127 (2011).
- [89] Kim, K., Lee, I. S., Centrone, A., Hatton, T. A. & Myerson, A. S. Formation of nanosized organic molecular crystals on engineered surfaces. *J. Am. Chem. Soc.* **131**, 18212–3 (2009).
- [90] Liu, S., Wang, W. M., Briseno, A. L., Mannsfeld, S. C. B. & Bao, Z. Controlled Deposition of Crystalline Organic Semiconductors for Field-Effect-Transistor Applications. *Adv. Mater.* **21**, 1217–1232 (2009).

- [91] Ito, A., Yamanobe-Hada, M. & Shindo, H. In situ AFM observation of polymorphic transformation at crystal surface of glycine. *J. Cryst. Growth* **275**, e1691–e1695 (2005).
- [92] Danesh, A. *et al.* The discrimination of drug polymorphic forms from single crystals using atomic force microscopy. *Pharm. Res.* **17**, 887–90 (2000).
- [93] Anantachaisilp, S. *et al.* Chemical and structural investigation of lipid nanoparticles: drug-lipid interaction and molecular distribution. *Nanotechnology* **21**, 125102 (2010).
- [94] Wen, H., Li, T., Morris, K. R. & Park, K. Dissolution Study on Aspirin and α -Glycine Crystals. *J. Phys. Chem. B* **108**, 11219–11227 (2004).
- [95] Hartman, P. & Perdok, W. G. On the relations between structure and morphology of crystals. I. *Acta Cryst.* **8**, 49–52 (1955).
- [96] Danesh, A. *et al.* An in situ dissolution study of aspirin crystal planes (100) and (001) by atomic force microscopy. *Pharm. Res.* **18**, 299–303 (2001).
- [97] Abendan, R. S. & Swift, J. A. Dissolution on Cholesterol Monohydrate Single-Crystal Surfaces Monitored by in Situ Atomic Force Microscopy. *Cryst. Growth Des.* **5**, 2146–2153 (2005).
- [98] Gvozdev, N. V., Petrova, E. V., Chernevich, T. G., Shustin, O. A. & Rashkovich, L. N. Atomic force microscopy of growth and dissolution of calcium oxalate monohydrate (COM) crystals. *J. Cryst. Growth* **261**, 539–548 (2004).
- [99] Petrova, E. V., Gvozdev, N. V. & Rashkovich, L. N. Growth and Dissolution of Calcium Oxalate Monohydrate (COM) Crystals. *J. Optoelectron. Adv. Mater.* **6**, 261–268 (2004).
- [100] Davies, M. *et al.* Characterization of drug particle surface energetics and young’s modulus by atomic force microscopy and inverse gas chromatography. *Pharm. Res.* **22**, 1158–66 (2005).
- [101] Cao, X., Sun, C. & Thamann, T. J. A study of sulfamerazine single crystals using atomic force microscopy, transmission light microscopy, and Raman spectroscopy. *J. Pharm. Sci.* **94**, 1881–92 (2005).

- [102] Zhang, J. *et al.* Determination of the surface free energy of crystalline and amorphous lactose by atomic force microscopy adhesion measurement. *Pharm. Res.* **23**, 401–7 (2006).
- [103] Wang, J. J., Li, T., Bateman, S. D., Erck, R. & Morris, K. R. Modeling of adhesion in tablet compression—I. Atomic force microscopy and molecular simulation. *J. Pharm. Sci.* **92**, 798–814 (2003).
- [104] Bérard, V. *et al.* Affinity scale between a carrier and a drug in DPI studied by atomic force microscopy. *Int. J. Pharm.* **247**, 127–37 (2002).
- [105] James, J. *et al.* The surface characterisation and comparison of two potential sub-micron, sugar bulking excipients for use in low-dose, suspension formulations in metered dose inhalers. *Int. J. Pharm.* **361**, 209–21 (2008).
- [106] James, J., Davies, M., Toon, R., Jinks, P. & Roberts, C. J. Particulate drug interactions with polymeric and elastomeric valve components in suspension formulations for metered dose inhalers. *Int. J. Pharm.* **366**, 124–32 (2009).
- [107] Young, P. M., Price, R., Tobyn, M. J., Buttrum, M. & Dey, F. Investigation into the effect of humidity on drug-drug interactions using the atomic force microscope. *J. Pharm. Sci.* **92**, 815–822 (2003).
- [108] Begat, P., Morton, D. A. V., Staniforth, J. N. & Price, R. The cohesive-adhesive balances in dry powder inhaler formulations I: Direct quantification by atomic force microscopy. *Pharm. Res.* **21**, 1591–7 (2004).
- [109] Traini, D., Young, P. M., Rogueda, P. & Price, R. The Use of AFM and Surface Energy Measurements to Investigate Drug-Canister Material Interactions in a Model Pressurized Metered Dose Inhaler Formulation. *Aerosol Sci. Tech.* **40**, 227–236 (2006).
- [110] Perkins, M. C. *et al.* Towards the understanding and prediction of material changes during micronisation using atomic force microscopy. *Eur. J. Pharm. Sci.* **38**, 1–8 (2009).
- [111] Ward, S. *et al.* Identifying and mapping surface amorphous domains. *Pharm. Res.* **22**, 1195–202 (2005).
- [112] Wu, M. *et al.* Nanoscale mechanical measurement determination of the glass transition temperature of poly(lactic acid)/everolimus coated stents in air and dissolution media. *Eur. J. Pharm. Sci.* **36**, 493–501 (2009).

- [113] Masterson, V. M. & Cao, X. Evaluating particle hardness of pharmaceutical solids using AFM nanoindentation. *Int. J. Pharm.* **362**, 163–71 (2008).
- [114] Cao, X., Morganti, M., Hancock, B. C. & Masterson, V. M. Correlating Particle Hardness With Powder Compaction Performance. *J. Pharm. Sci.* **99**, 4307–4316 (2010).
- [115] Reddy, C. M. *et al.* Structural basis for bending of organic crystals. *Chem. Commun.* **1**, 3945–7 (2005).
- [116] Kiran, M. S. R. N., Varughese, S., Reddy, C. M., Ramamurty, U. & Desiraju, G. R. Mechanical Anisotropy in Crystalline Saccharin: Nanoindentation Studies. *Cryst. Growth Des.* **10**, 4650–4655 (2010).
- [117] Karunatilaka, C. *et al.* Softening and hardening of macro- and nano-sized organic cocrystals in a single-crystal transformation. *Angew. Chem. Int. Ed.* **50**, 8642–6 (2011).
- [118] Jing, Y., Zhang, Y., Blendell, J., Koslowski, M. & Carvajal, M. T. Nanoindentation Method To Study Slip Planes in Molecular Crystals in a Systematic Manner. *Cryst. Growth Des.* **11**, 5260–5267 (2011).
- [119] Kaupp, G., Schmeyers, J. & Hangen, U. D. Anisotropic molecular movements in organic crystals by mechanical stress. *J. Phys. Org. Chem.* **15**, 307–313 (2002).
- [120] Kaupp, G. & Naimi-Jamal, M. R. Mechanically induced molecular migrations in molecular crystals. *CrystEngComm* **7**, 402 (2005).
- [121] Six, K. *et al.* Identification of phase separation in solid dispersions of itraconazole and Eudragit E100 using microthermal analysis. *Pharm. Res.* **20**, 135–8 (2003).
- [122] Royall, P. G., Craig, D. Q. M., Price, D. M., Reading, M. & Lever, T. J. An investigation into the use of micro-thermal analysis for the solid state characterisation of an HPMC tablet formulation. *Int. J. Pharm.* **192**, 97–103 (1999).
- [123] Royall, P. G., Kett, V. L., Andrews, C. S. & Craig, D. Q. M. Identification of Crystalline and Amorphous Regions in Low Molecular Weight Materials Using Microthermal Analysis. *J. Phys. Chem. B* **105**, 7021–7026 (2001).

- [124] Dai, X., Reading, M. & Craig, D. Q. M. Mapping Amorphous Material on a Partially Crystalline Surface : Nanothermal Analysis for Simultaneous Characterisation and Imaging of Lactose Compacts. *J. Pharm. Sci.* **98**, 1499–1510 (2009).
- [125] Harding, L., Wood, J., Reading, M. & Craig, D. Q. M. Two- and three-dimensional imaging of multicomponent systems using scanning thermal microscopy and localized thermomechanical analysis. *Anal. Chem.* **79**, 129–39 (2007).
- [126] Kraya, R. A. & Bonnell, D. A. Determining the Electronic Properties of Individual Nanointerfaces by Combining Intermittent AFM Imaging and Contact Spectroscopy. *IEEE Trans. Nanotechnol.* **9**, 741–744 (2010).
- [127] Hendriksen, B. L. M. *et al.* Electrical transport properties of oligothiophene-based molecular films studied by current sensing atomic force microscopy. *Nano letters* **11**, 4107–12 (2011).
- [128] Park, J. Y. & Qi, Y. Probing nanotribological and electrical properties of organic molecular films with atomic force microscopy. *Scanning* **32**, 257–64 (2010).
- [129] Kelley, T. W., Granstrom, E. L. & Frisbie, C. D. Conducting Probe Atomic Force Microscopy : A Characterization Tool for Molecular Electronics. *Adv. Mater.* **55455**, 261–264 (1999).
- [130] Kapadia, P. P. *et al.* Semiconducting Organic Assemblies Prepared from Tetraphenylethylene Tetracarboxylic Acid and Bis(pyridine)s via Charge-Assisted Hydrogen Bonding. *J. Am. Chem. Soc.* **133**, 8490–8493 (2011).
- [131] Tsunemi, E., Kobayashi, K., Matsushige, K. & Yamada, H. Visualization of anisotropic conductance in polydiacetylene crystal by dual-probe frequency-modulation atomic force microscopy/Kelvin-probe force microscopy. *J. Vac. Sci. Technol. B* **28**, C4D24 (2010).
- [132] Nonnenmacher, M., OBoyle, M. P. & Wickramasinghe, H. K. Kelvin probe force microscopy. *Appl. Phys. Lett.* **58**, 2921 (1991).
- [133] Araujo, P. T. *et al.* In situ atomic force microscopy tip-induced deformations and Raman spectroscopy characterization of single-wall carbon nanotubes. *Nano letters* **12**, 4110–6 (2012).

- [134] Gerhardt, C. Researches on the constitution of organic acids. *Q. J. Chem. Soc.* **5**, 127 (1853).
- [135] Gore, A. Y. *et al.* Significance of salicylic acid sublimation in stability testing of aspirin-containing solids. *J. Pharm. Sci.* **57**, 1850–1854 (1968).
- [136] Alibrandi, G., Micali, N., Trusso, S. & Villari, A. Hydrolysis of aspirin studied by spectrophotometric and fluorometric variable-temperature kinetics. *J. Pharm. Sci.* **85**, 1105–8 (1996).
- [137] Edwards, L. J. The Hydrolysis of Aspirin - A Determination of the Thermodynamic Dissociation Constant and a Study of the Reaction Kinetics by Ultra-Violet Spectrophotometry. *Trans. Faraday. Soc.* **46**, 723–735 (1950).
- [138] Edwards, L. J. The Hydrolysis of Aspirin. *Trans. Faraday Soc.* **48**, 696–699 (1952).
- [139] Garrett, E. R. The Kinetics of Solvolysis of Acyl Esters of Salicylic Acid. *J. Am. Chem. Soc.* **79**, 3401–3408 (1957).
- [140] Watanabe, K. Kinetic Studies on Hydrolysis of Acetylsalicylic Acid in Binary Systems of Water and Organic Solvents. *Yakugaku Zasshi* **90**, 1570–1573 (1970).
- [141] Leeson, L. J. & Mattocks, A. M. Decomposition of Aspirin in the Solid State. *J. Am. Pharm. Assoc.* **47**, 329–333 (1958).
- [142] Carstensen, J. T., Attarchi, F. & Hou, X.-P. Decomposition of Aspirin in the Solid State in the Presence of Limited Amounts of Moisture. *J. Pharm. Sci.* **74**, 741–745 (1985).
- [143] Yang, W.-H. & Brooke, D. Rate equation for solid state decomposition of aspirin in the presence of moisture. *Int. J. Pharm.* **11**, 271–276 (1982).
- [144] Ball, M. C. Solid-state Hydrolysis of Aspirin. *J. Chem. Soc. Faraday Trans.* **90**, 997–1001 (1994).
- [145] Hasegawa, J., Hanano, M. & Awazu, S. Decomposition of Acetylsalicylic Acid and Its Derivatives in Solid State. *Chem. Pharm. Bull.* **23**, 86–97 (1975).
- [146] Carstensen, J. T. & Attarchi, F. Decomposition of Aspirin in the Solid State in the presence of Limited Amounts of Moisture III: Effect of Temperature and a Possible Mechanism. *J. Pharm. Sci.* **77**, 318–321 (1988).

- [147] Vishweshwar, P., McMahon, J. A., Oliveira, M., Peterson, M. L. & Zaworotko, M. J. The predictably elusive form II of aspirin. *J. Am. Chem. Soc.* **127**, 16802–3 (2005).
- [148] Bond, A. D., Boese, R. & Desiraju, G. R. On the polymorphism of aspirin: crystalline aspirin as intergrowths of two "polymorphic" domains. *Angew. Chem. Int. Ed.* **46**, 618–22 (2007).
- [149] Bond, A. D., Boese, R. & Desiraju, G. R. On the polymorphism of aspirin. *Angew. Chem. Int. Ed.* **46**, 615–7 (2007).
- [150] Wheatley, P. J. The Crystal and Molecular Structure of Aspirin. *J. Chem. Soc.* 6036–6048 (1964).
- [151] Bond, A. D., Solanko, K. A., Parsons, S., Redder, S. & Boese, R. Single crystals of aspirin form II: crystallisation and stability. *CrystEngComm* **13**, 399 (2011).
- [152] Arora, K. K., Tayade, N. G. & Suryanarayanan, R. Unintended water mediated cocrystal formation in carbamazepine and aspirin tablets. *Mol. Pharm.* **8**, 982–9 (2011).
- [153] Bica, K., Rijkssen, C., Nieuwenhuyzen, M. & Rogers, R. D. In search of pure liquid salt forms of aspirin: ionic liquid approaches with acetylsalicylic acid and salicylic acid. *Phys. Chem. Chem. Phys.* **12**, 2011 (2010).
- [154] Lee, S., Dekay, H. G. & Banker, G. S. Effect of Water Vapor Pressure on Moisture Sorption and the Stability of Aspirin and Ascorbic Acid in Tablet Matrices. *J. Pharm. Sci.* **54**, 1153–1158 (1965).
- [155] Gucluyildiz, H., Banker, G. S. & Peck, G. E. Determination of Porosity and Pore-Size Distribution of Aspirin Tablets Relevant to Drug Stability. *J. Pharm. Sci.* **66**, 407–414 (1977).
- [156] Gore, A. Y. & Banker, G. S. Surface Chemistry of Colloidal Silica and a Possible Application to Stabilize Aspirin in Solid Matrixes. *J. Pharm. Sci.* **68**, 197–202 (1979).
- [157] Ager, D. J. *et al.* Stability of Aspirin in Solid Mixtures. *J. Pharm. Sci.* **75**, 97–101 (1986).
- [158] Yuasa, H., Kanaya, Y. & Asahina, K. Studies on Whisker Growth on the Tablet Surface. III. Mechanism of Whisker Growth on Aspirin Tablet

- and Its Effect on the Mechanical Strength of the Tablet. *Chem. Pharm. Bull.* **34**, 850–857 (1986).
- [159] Yuasa, H., Yamashita, J. & Kanaya, Y. Studies on Whisker Growth in Solid Preparations. VI. Whisker Growth in Mixtures Composed of Aspirin and Porous Glass Powder. *Chem. Pharm. Bull.* **41**, 731–736 (1993).
- [160] Landin, M. *et al.* Chemical stability of acetylsalicylic acid in tablets prepared with different particle size fractions of a commercial brand of dicalcium phosphate dihydrate. *Int. J. Pharm.* **123**, 143–144 (1995).
- [161] Du, J. & Hoag, S. W. The influence of excipients on the stability of the moisture sensitive drugs aspirin and niacinamide: comparison of tablets containing lactose monohydrate with tablets containing anhydrous lactose. *Pharm. Dev. Technol.* **6**, 159–66 (2001).
- [162] Landin, M., Fontao, M. J. & Martínez-Pacheco, R. A Comparison of Trehalose Dihydrate and Mannitol as Stabilizing Agents for Dicalcium Phosphate Dihydrate Based Tablets. *Drug Dev. Ind. Pharm.* **31**, 249–256 (2005).
- [163] Mihranyan, A., Stromme, M. & Ek, R. Influence of cellulose powder structure on moisture-induced degradation of acetylsalicylic acid. *Eur. J. Pharm. Sci.* **27**, 220–5 (2006).
- [164] Heidarian, M., Mihranyan, A., Stromme, M. & Ek, R. Influence of water-cellulose binding energy on stability of acetylsalicylic acid. *Int. J. Pharm.* **323**, 139–45 (2006).
- [165] Builders, P. F., Bonaventure, A. M., Tiwalade, A., Okpako, L. C. & At-tama, A. a. Novel multifunctional pharmaceutical excipients derived from microcrystalline cellulose-starch microparticulate composites prepared by compatibilized reactive polymer blending. *Int. J. Pharm.* **388**, 159–67 (2010).
- [166] Glombitza, B. W. & Schmidt, P. C. Comparison of Three New Spectrophotometric Methods for Simultaneous Determination of Aspirin and Salicylic Acid in Tablets without Separation of Pharmaceutical Excipients. *J. Pharm. Sci.* **83**, 751–757 (1994).
- [167] Tawashi, R. Dissolution Rates of Two Polymorphic Forms. *Science* **160**, 76 (1968).

- [168] Kim, Y., Machida, K., Taga, T. & Osaki, K. Structure Redetermination and Packing Analysis of Aspirin Crystal. *Chem. Pharm. Bull.* **33**, 2641–2647 (1985).
- [169] Heng, J. Y. Y., Bismarck, A., Lee, A. F., Wilson, K. & Williams, D. R. Anisotropic Surface Chemistry of Aspirin Crystals. *J. Pharm. Sci.* **96**, 2134–2144 (2007).
- [170] Aubrey-Medendorp, C., Parkin, S. & Li, T. The Confusion of Indexing Aspirin Crystals. *J. Pharm. Sci.* **97**, 1361–1367 (2008).
- [171] Varughese, S. *et al.* Interaction anisotropy and shear instability of aspirin polymorphs established by nanoindentation. *Chem. Sci.* **2**, 2236–2242 (2011).
- [172] Cassidy, A. M. C., Gardner, C. E., Auffret, T., Aldous, B. & Jones, W. Decoupling the Effects of Surface Chemistry and Humidity on Solid-State Hydrolysis of Aspirin In the Presence of Dicalcium Phosphate Dihydrate. *J. Pharm. Sci.* **101**, 1496–1507 (2012).
- [173] Donnay, J. D. H. & Harker, D. A New Law of Crystal Morphology Extending the Law of Bravais. *Am. Mineral.* **22**, 446 (1937).
- [174] Tang, A.-M. & Cui, Y.-J. Controlling suction by the vapour equilibrium technique at different temperatures and its application in determining the water retention properties of MX80 clay. *Can. Geotech. J.* **42**, 287–296 (2005).
- [175] Stevens, J. S., Byard, S. J., Zlotnikov, E. & Schroeder, S. L. M. Detection of free base surface enrichment of a pharmaceutical salt by X-ray photoelectron spectroscopy (XPS). *J. Pharm. Sci.* **100**, 942–8 (2011).
- [176] Matlis, S. & Edgar, R. Experimental Evaluation of Probe Sample Force in Tapping Mode Scanning Force Microscopy. *Surf. Interface Anal.* **27**, 374–378 (1999).
- [177] Fujita, M. *et al.* Real-Time Observations of Oriented Crystallization of Poly(-caprolactone) Thin Film, Induced by an AFM Tip. *Macromol. Chem. Phys.* **208**, 1862–1870 (2007).
- [178] Cochran, W. The crystal and molecular structure of salicylic acid. *Acta Cryst.* **6**, 260–268 (1953).

- [179] Ebisuzaki, Y., Boyle, P. D. & Smith, J. a. Methylxanthines. I. Anhydrous Theophylline. *Acta Cryst.* **C53**, 777–779 (1997).
- [180] Brock, C. P. & Dunitz, J. D. Temperature dependence of thermal motion in crystalline anthracene. *Acta Cryst.* **B46**, 795–806 (1990).
- [181] Arshadi, M. R. Determination of heats of sublimation of organic compounds by a mass spectrometric-knudsen effusion method. *J. Chem. Soc. Faraday Trans. 1* **70**, 1569–1571 (1974).
- [182] Perlovich, G. L., Kurkov, S. V., Kinchin, A. N. & Bauer-Brandl, A. Solvation and hydration characteristics of ibuprofen and acetylsalicylic acid. *AAPS J.* **6**, 22–30 (2004).
- [183] Chickos, J. S. & Acree Jr., W. E. Enthalpies of Sublimation of Organic and Organometallic Compounds. 19102001. *J. Phys. Chem. Ref. Data* **31**, 537–698 (2002).
- [184] Vatvani, D. R. M. *Thesis to be submitted*. Ph.D. thesis, University of Cambridge (2014).
- [185] Gavezzotti, A. & Filippini, G. Geometry of the Intermolecular X-H.cntdot..cntdot..cntdot.Y (X, Y = N, O) Hydrogen Bond and the Calibration of Empirical Hydrogen-Bond Potentials. *J. Phys. Chem.* **98**, 4831–4837 (1994).
- [186] Filippini, G. & Gavezzotti, A. Empirical intermolecular potentials for organic crystals: the ‘6-exp’ approximation revisited. *Acta Crystallogr., Sect. B: Struct. Sci.* **49**, 868–880 (1993).
- [187] Perlovich, G. L. & Bauer-Brandl, A. Thermodynamics of solutions I: benzoic acid and acetylsalicylic acid as models for drug substances and the prediction of solubility. *Pharm. Res.* **20**, 471–478 (2003).
- [188] Cohen, M. D. The Photochemistry of Organic Solids. *Angew. Chem. Int. Ed.* **14**, 386 (1975).
- [189] Cohen, M. D. & Schmidt, G. M. J. Topochemistry . Part I . A Survey. *J. Chem. Soc.* 1996 (1964).
- [190] Schmidt, G. M. J. Topochemistry. Part III. The Crystal Chemistry of some trans-Cinnamic Acids. *J. Chem. Soc.* 2014–2021 (1964).

- [191] Cohen, M. D., Schmidt, G. M. J. & Sonntag, F. I. Topochemistry. Part II. The Photochemistry of trans-Cinnamic Acids. *J. Chem. Soc.* 2000 (1964).
- [192] Kaupp, G. Photodimerization of Anthracenes in the Solid State: New Results from Atomic Force Microscopy. *Angew. Chem. Int. Ed.* **31**, 595–598 (1992).
- [193] Chandross, E. A. & Ferguson, J. Photodimerization of Crystalline Anthracene. The Photolytic Dissociation of Crystalline Dianthracene. *J. Chem. Phys.* **45**, 3564–3567 (1966).
- [194] Thomas, J. M. & Williams, J. O. Lattice Imperfections in Organic Solids Part 2. *Trans. Faraday Soc.* **63**, 1922–1928 (1967).
- [195] Craig, D. P. & Sarti-Fantoni, P. Photochemical Dimerisation in Crystalline Anthracenes. *Chem. Commun.* 742–743 (1966).
- [196] Choi, C. S. & Marinkas, P. L. Refinement of Di-para-anthracene. *Acta Cryst.* **B36**, 2491–2493 (1980).
- [197] Cordeiro, D. S. & Corio, P. Electrochemical and Photocatalytic Reactions of Polycyclic Aromatic Hydrocarbons Investigated by Raman Spectroscopy. *J. Braz. Chem. Soc.* **20**, 80–87 (2009).
- [198] Lonsdale, D. K., Nave, E. & Stephens, J. F. X-Ray Studies of a Single Crystal Chemical Reaction: Photo-Oxide of Anthracene to (Anthraquinone, Anthrone). *Phil. Trans. R. Soc. A* **261**, 1–31 (1966).